Quantum-orbit analysis of laser-matter interactions in intense orthogonally polarised fields

by

Toni Das

Under the supervision of Doctor Carla Figueira de Morisson Faria
and the subsidiary supervision of Doctor Dan Browne

A thesis submitted in partial fulfilment for the
degree of Doctor of Philosophy

University College London
Department of Physics and Astronomy

Examination committee:

Doctor Stephen Hogan

Doctor Adam Kirrander

March 16, 2017

Declaration of authorship

I, Toni Das, declare that this thesis titled 'Quantum- orbit analysis of laser-matter interactions in intense orthogonally polarised fields' and the work presented in it is my own. I confirm that:

- This work was done wholly or mainly while in candidature for a research degree at this University.
- Where any part of this thesis has previously been submitted for a degree or any other qualification at this University or any other institution, this has been clearly stated.
- Where I have consulted the published work of others, this is always clearly attributed.
- Where I have quoted from the work of others, the source is always given. With the exception of such quotations, this thesis is entirely my own work.
- I have acknowledged all main sources of help.
- Where the thesis is based on work done by myself jointly with others, I have made clear exactly what was done by others and what I have contributed myself.

Signed:

Date:

"We're all born naked, the rest is drag" - Rupaul

Abstract

A quantum-orbit analysis of laser-matter interactions allows us to understand, in terms of electron trajectories, the influence of intense orthogonally polarised fields on strong field phenomena. In doing so it allows us to understand the electron dynamics in the continuum and disentangle the influence of the field from the imprints left by the target molecule in the photoelectron and high-order harmonic spectra of strong field phenomena. This is the main topic of this thesis which focuses on temporal and spatial quantum interference in high harmonic generation (HHG) from molecules and above-threshold ionisation (ATI) from atoms. These are investigated semi-analytically at the single-molecule response and single-active orbital level, using the strong field approximation and the steepest descent method. In the case of HHG, a further investigation is performed at the macroscopic harmonic response level to model experimental HHG spectra by using Maxwell's wave equations. HHG from molecules in orthogonally polarised fields is the most extensive topic of this work.

At the single-molecule response level, we first investigate the influence of employing an orthogonally polarised field on the structural interference minima in high-order harmonic spectra from aligned diatomic molecules such as H_2 and Ar_2 in bichromatic orthogonally polarised fields and elliptical fields. We derive a generalised two-centre interference condition, which accounts for s-p mixing and the orbital symmetry, within the strong field and the single-active electron approximation. We show that the orthogonally polarised fields introduce an effective dynamic shift in the angle for which the two-centre interference maxima and minima occur, with regard to the existing condition for linearly polarised fields. This shift depends on the ratio between the field-dressed momentum components of the returning electron parallel and perpendicular to the major polarisation axis along each possible orbit, and therefore incorporates the electron's angle of return. Because of this dependence, we find that there will be a blurring in the two-centre interference minima, and that increasing ellipticity leads to splitting in such patterns. We modelled the macroscopic harmonic response level, to investigate whether the features were washed out or survive high harmonic propagation to the far-field. We propose the optimal conditions for observing these shifted minima, using phase matching

and polarisation gating, so they can be measured experimentally, with the possibility of extracting the electrons angle of return.

In our analysis of the imprint of nodal planes in high-order harmonic spectra from aligned diatomic molecules in orthogonal polarised fields, we show that the typical suppression in the spectra associated to nodal planes is distorted. This distortion can also be employed to map the electron's angle of return to its parent ion. We show that the velocity form of the dipole operator is superior to the length form in providing information about this distortion. However, both forms introduce artefacts that are absent in the actual momentum-space wavefunction. Furthermore, elliptically polarised fields lead to larger distortions in comparison to two-colour orthogonally polarised fields. These features are investigated in detail for O_2, whose highest occupied molecular orbital provides two orthogonal nodal planes.

Lastly we investigate temporal interference in direct ATI momentum distribution maps, employing linear and orthogonally polarised fields. We identify a type of intra-cycle interference that is often overlooked in other studies and using an orthogonally polarised field we show that the momentum distributions for individual trajectories separate. This reduces the overlap between the two distributions leading to the reduction of intra-cycle interference.

Acknowledgements

I wish to express my greatest thanks and appreciation to Dr. Carla Figueira de Morisson Faria for her expertise, guidance, patience and support, without which this thesis would not have been possible. Thanks also to the UK Engineering and Physical Sources Research Council (EPRSC) and the UCL impact studentship for funding my PhD. I am grateful to Professor Jon Morangos and his group at Imperial College London for the use of their HHG propagation code and thank you to Dr Luke Chipperfield for his help with the modifications. A special thanks for Dr Bradley Bernhard Augstein for his invaluable help and discussions throughout my Masters and PhD. Finally, I am extremely grateful to my family and friends, especially to my parents Eileen Williams and Robin K. Das, my partner Anna Goldstone, my sister Robin V. Das and my aunt Ruth Gopaul-Jacobs, for their love, encouragement and emotional support throughout my PhD. Thank you to my nan Lillian Jacobs for calling me up almost every day with encouragement and thank you Cissie Williams for everything, we miss you.

Frame of this research

The work presented in this thesis has been carried out in the Physics and Astronomy department of University College London, between September 2012 until March 2016, under the supervision of Dr. Carla Figueira de Morisson Faria and subsidiary supervision of Dr. Dan Browne. Some of the work includes collaborations with Prof. Jon P. Marangos, Dr. Luke E. Chipperfield and Dr. David J. Hoffmann of the Quantum Optics and Laser Science Group of the Department of Physics at Imperial College London. Parts of this thesis maybe be found in the following papers:

Paper 1: T. Das, B. B. Augstein, and C. Figueira de Morisson Faria, "High-order-harmonic generation from diatomic molecules in driving fields with non-vanishing ellipticity: A generalized interference condition", Phys. Rev. A, vol. 88, p. 023404, (2013) (reference [1]).

Paper 2: T. Das, B. B. Augstein, C. Figueira de Morisson Faria, L. E. Chipperfield, D. J. Hoffmann, and J. P. Marangos, "Extracting an electron's angle of return from shifted interference patterns in macroscopic high-order-harmonic spectra of diatomic molecules", Phys. Rev. A, vol. 92, p. 023406 (2015) (reference [2])

Paper 3: T. Das and C. Figueira de Morisson Faria, "Shifting nodal-plane suppressions in high-order harmonic spectra from diatomic molecules in orthogonally polarized driving fields", arXiv:1602.04030v1 (2016)

In this thesis the contents of paper 1,2,3 and 4 appear in Chapters 4, 5, 7 and 9, respectively. I am the lead author of all papers except paper 4, where I contributed the section analysing intra- and inter-cycle interference in above threshold ionisation and affects of employing and elliptically polarised field.

Contents

List of Figures

Part I

General overview

Chapter 1

Introduction

1.1 Orthogonally polarised fields

The common topic of the work represented in this thesis is the interaction of matter with fields composed of two orthogonally polarised wave propagating in the same direction, but oscillate at a perpendicular angle to each other. The importance of fields composed in this way is that they introduce control over another degree of freedom to processes such as molecular alignment and electron motion. For instance, it was shown theoretically and experimentally that elliptically polarised fields could be used to achieve three dimensional alignment of 3,4-dibromothiophene molecules and restrict its movement along all three axes [4]. Previous to this work linearly polarised fields were used, which could align molecule along one axis, but could not restrict the rotation of the aligned molecule. Even at a biological level studies have suggested that elliptically polarised light can be tuned between linear and circular polarisation to be used as a non-invasive probe to image tissues such as an exposed cerebral cortex or skin specific depths. In this way they could serve as diagnostic tool for early disease detection, such as cancerous growths [5, 6, 7, 8].

Since the mid 1990s, orthogonally polarised fields have been proposed as a resource for controlling strong-field phenomena, such as high-order harmonic generation (HHG), above threshold ionisation (ATI) and non-sequential double ionisation (NSDI). These phenomena were measured for the first time when strong driving fields of intensity I $> 10^{13}$ W/cm^2 were employed [9, 10, 11, 12]. At the time their existence could not be explained by perturbation theory. This is because at these intensities the driving field can no longer be treated as a perturbation, as it was now comparable to the Coulomb field of the target atom or molecule for the outer-shell electrons.

Nowadays, the three step mechanism [13] is commonly used to explain how the strong-field phenomena are produced [see Fig. 1.1]. The first step of this mechanism is ionisation

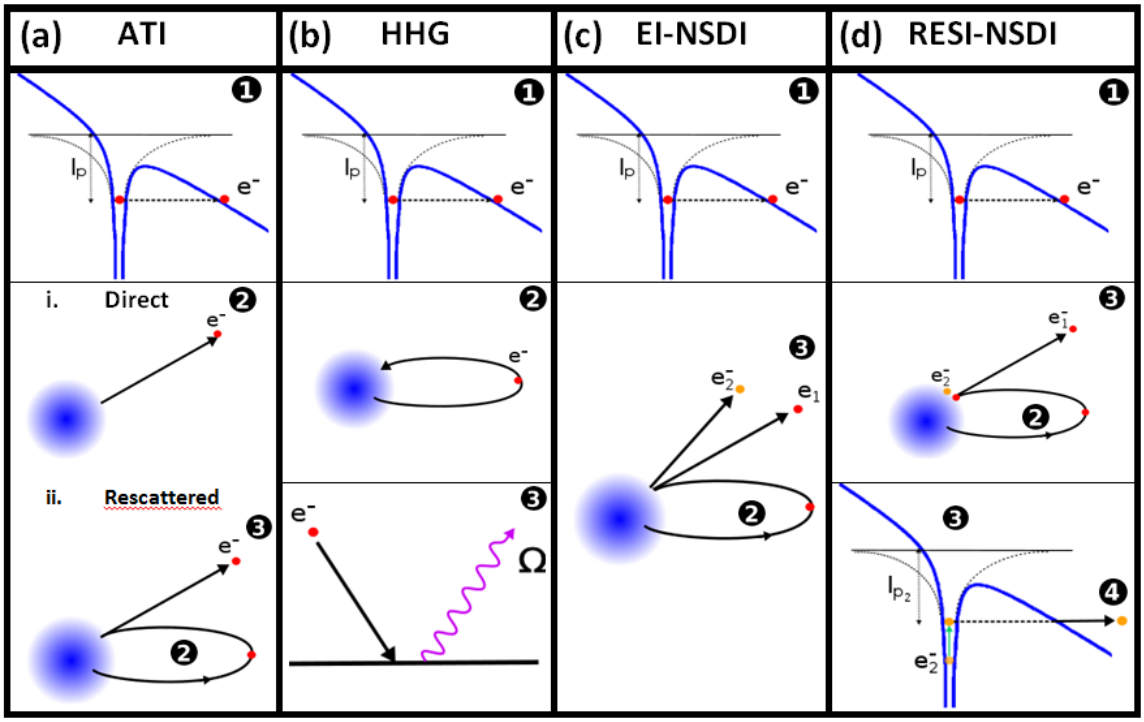

Figure 1.1: Schematic representation of the three step mechanism (TSM) for (a) direct ATI (i) and rescattered ATI (ii), (b) HHG, (c) electron impact (EI) NDSI and (d) recollision excitation with sub-sequential tunnelling ionization (RESI) NSDI. The numbers in black circles indicate the steps in the TSM.

of an electron via multiphoton or tunnel ionisation [Fig. 1.1(1)]. In the second step this freed electron propagates in the continuum accumulating kinetic energy from the laser field [Fig. 1.1(2)]. Some electrons may leave the vicinity of their parent ion reaching the detector without further interaction (direct ATI) [Fig. 1.1(a)i] and some may return. If an electron returns, in the third step it can either: recombine with its parent ion, releasing its energy in the form of emitted high-harmonic radiation (HHG) [Fig. 1.1(b)]; elastically re-scatter with it (rescattered ATI) [Fig. 1.1(a)ii] or collide inelastically to free a second electron from the atom or molecule (electron impact NSDI) [Fig. 1.1(c)] or excited the second electron which tunnel ionises some time later and reaches the detector (recollision excitation with sub-sequential tunnelling ionization NSDI) [Fig. 1.1(d)].

Introducing a second field that is orthogonally polarised to the first, enables one to steer the motion of the active electron in the continuum and control how it returns to the core. This introduces a momentum component perpendicular to the momentum an electron usually acquires from a linearly polarised laser. This is the key idea behind polarisation-gating techniques, where this new degree of freedom may be controlled by modifying the field ellipticity. For instance, lasers with changing ellipticity over time were suggested in [14, 15, 16, 17] as a way to produce isolated attosecond pulses. This

was experimentally realised in [18, 19], where the dependence of HHG on the ellipticity of the driving pulses was used to create a temporal window of linear polarisation, for which the generation of extreme ultra violet (XUV) harmonics is possible. This technique allows the generation of a broadband of XUV pulses with the possibility of single-cycle pulses. This is an improvement on the attopulses produced through linearly polarised pulses, for which only the spectral portion around the cut off can be used [20, 21, 22]. Furthermore, polarisation-gating techniques allow a substantial increase in the intensity of the attosecond pulses produced [23]. Another important application of polarisation-gated pulses is the attosecond imaging of matter, in particular the reconstruction of molecular orbitals [24].

This potential for imaging was first realised with aligned molecules using linearly polarised fields [25] and was later achieved for molecules such as CO2 [26] and CO [27, 28]. However, pairs of orthogonally polarised fields exhibit a series of advantages. They allow a greater degree of control of the angle with which an electron leaves and returns to its parent ion [29, 24]. Hence, in principle, there is no necessity of aligning or rotating the molecule to be imaged, this provides access to degenerate orbitals, or molecules that are difficult to align. They also allow molecular-orbital reconstruction from a single-shot measurement [24]. This may be useful for probing dynamic processes in which space, energy and time coherence are important.

Orthogonal two colour fields have a particular advantage over elliptically polarised fields as they have less impact on HHG efficiency as the strength of the perpendicular field is increased. In fact it was shown in [30, 31] that adding a weaker second harmonic field at a well chosen phase difference enhanced the signal of the harmonics generated. This has also been shown to suppress or enhance the contributions of individual orbits along which the re-colliding electron may return [32]. Trajectory selection was also reported in Ref. [33], where it was shown that the correlated electron dynamics in the electron impact mechanism of NSDI was strongly influenced by the phase difference in the orthogonal two colour field, producing strong anti correlated patterns in momentum distribution maps. The origin of this influence was due to the fact that the window of time with which the first ionised electron could return to the parent ion was significantly reduced. This meant that only a select group of trajectories could rescatter and ionised the second electron.

For ATI most studies with orthogonally polarised fields have focused mainly on the angular dependence on the ionisation rate [34, 35, 36, 37]. In one study it was shown that elliptically polarised fields could be used to suppress the contribution of electrons that re-scatter. This revealed temporal interference between electron trajectories that are associated with direct ATI, where recollision does not occur [38]. For rescattered ATI, it has been shown that increasing the ellipticity of the field, increases the contributions of quantum orbits that spend much longer in the continuum, with contributions from shorter

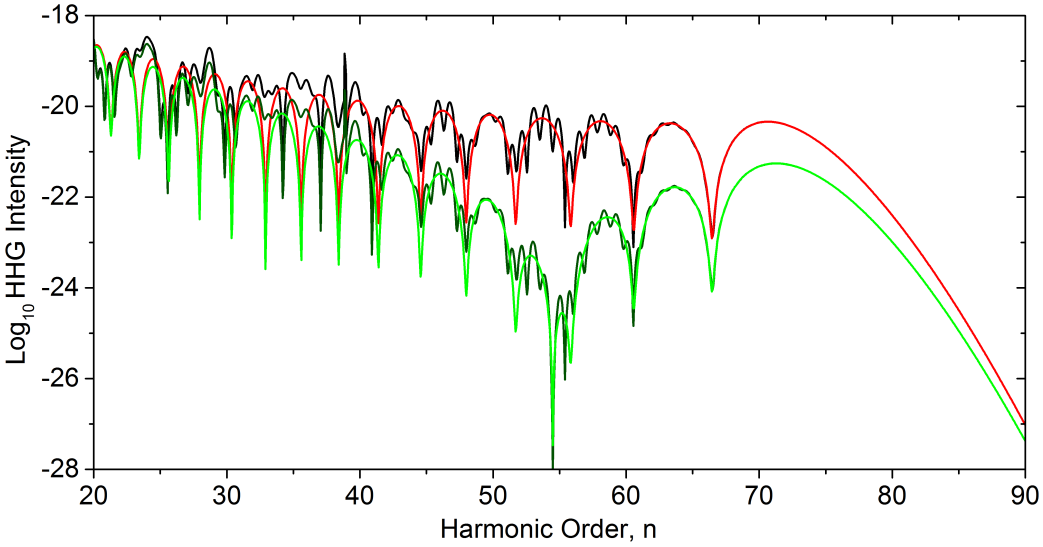

Figure 1.2: High-order harmonic spectrum calculated using the strong field approximation model, from a hydrogen atom, H (black and red solid curves) and a hydrogen molecule, H_2 (dark and light green curves) subjected to a continuous monochromatic linearly polarised field of intensity $I = 5 \times 10^{14}$ W/cm^2 and frequency $\omega = 0.057$ a.u. The ionisation potential of H and H_2 are $I_p = 0.5$ a.u. and $I_p = 0.59$ a.u., respectively. The H_2 molecule has an internuclear distance of $R = 1.4$ a.u. and is aligned parallel to the polarisation of driving laser field. The red and light green [black and dark green] curves give the HHG spectrum contributions from the two [six] shortest trajectories ionising from the same peak in the electric field.

orbits decreasing rapidly [39]. This kind of work shows the importance of including these longer orbits when modelling these phenomena, which are often ignored.

1.2 Quantum interference

1.2.1 Temporal interference

The three step mechanism of ionisation, propagation and possible recombination, tells us that in the propagation step the electron follows a trajectory that is influenced by the force exerted on it by the laser field. For strong field phenomena that involve a rescattering or recombination mechanism such as rescattered ATI, NSDI and HHG, this trajectory returns to the site of ionisation after it has propagated in the continuum. In HHG for example, the quantum mechanical picture tells us that an emitted high harmonic is the result of a sum over many quantum trajectory contributions that the electron can take and return with a particular kinetic energy that it has gained in the continuum [40, 41]. These trajectories acquire a phase while propagating in the continuum which will depend on the excursion time and the pondermotive energy of the laser driving field,

$U_p = E_0^2/4\omega^2$, where E_0 and ω are the electric field amplitude and the angular frequency of the driving laser field. The difference in phase between these trajectories will give rise to constructive and destructive interference, which will lead to an interference pattern across the high harmonic spectrum. In Fig. 1.2 we can see the temporal interference between the two shortest trajectories, giving rise to the bumps and troughs in the higher harmonic spectrum given by the red curve. We can also see that as we go to the high harmonic orders the interference pattern gets thicker, indicating that phase difference due to the difference in excursion time is getting smaller. In fact, at the cut-off, indicated by the sudden drop in HHG signal, the trajectories have actually coalesced into one trajectory. For rescattered ATI, where the electron reaches the detector in the final step, the individual contributions from different pairs of trajectories were observed, when the single plateau normally observed with a linearly polarised field was transformed into a staircase of plateaus with the use of elliptically polarised fields [42, 43]. Each plateau could be associated to contributions from a particular pair of trajectories. For HHG, observing temporal interference of trajectories is less straight forward as spatial and temporal averaging blurs the fringes at the macroscopic harmonic response level. In Ref. [44] they showed that this can be avoided by varying the intensity of the driving laser field, thereby changing the relative phase of the contributing trajectories and carefully selecting macroscopic conditions. This allowed them to observe interference between the two shortest pairs of trajectories.

For direct ATI, these trajectories take the electron to the detector without rescattering. In a linearly polarised field their final momentum is determined by the time at which they are ionised, which is most probably around the peak of the electric field. Constructive or destructive interference will occur when trajectories that start at different parts of the electric field reach the detector with the same final momentum. Within one cycle of the electric field the electron can reach the detector with a range of final momentums via two possible trajectories that start from adjacent peaks of the electric field. This creates an intra-cycle interference pattern that arises from the temporal double slit created by the time difference between these trajectory start times [45]. If more than one cycle of the field is considered, trajectories starting from consecutive peaks separated by one cycle will constructively and destructively interfere. This leads to inter-cycle interference pattern that can be thought of as arising from a temporal diffraction grating consisting of N slits, where N is the number of cycles of the field [45]. This inter-cycle interference is the well known ATI peaks which appears as a pattern of rings in the momentum distribution maps [46, 47].

1.2.2 Spatial interference from molecules

For linearly polarised driving fields, molecular imprints in HHG spectra have been widely studied, at least within the single-active electron and single-active orbital approximation. For instance, it is by now common knowledge that nodal planes cause a strong suppression in HHG spectra if they are aligned parallel to the laser-field polarisation [48]. This suppression arises from the fact that nodal planes are areas of vanishing probability density in the wavefunction of the target molecule. This suppresses ionisation in the first step of the HHG mechanism. Additionally a vanishingly small overlap of the returning electronic wavefunction and the core wave function of the molecule suppresses recombination in the third step of the HHG mechanism. This suppression was confirmed in experiment and theoretical calculations that compared HHG from aligned CO_2, which possesses two nodal planes in its highest occupied molecular orbital (HOMO), and N_2, which possesses none.

High harmonic spectra from aligned molecules also exhibit a multi-slit like interference pattern, with pronounced maxima and minima, which are dependent on the internuclear distance and the orientation of the molecule with respect to the polarisation of the laser field. This is a structural effect that results from the electron wave packet recombining to spatially different centres. For the simplest scenario, i.e., a diatomic molecule, these interference patterns have been experimentally observed for molecules such as H_2^+ and CO_2 (which can be considered to be an elongated O_2 molecule) [49, 50, 51]. They have also been observed in other strong field phenomena such as rescattered ATI from O_2 [52]. In Ref. [53], theoretical predictions for two centre interference in HHG showed the pronounced minima within the plateau of the HHG spectrum from H_2 and H_2^+, were expected to occur for

$$R\cos\theta_L = (2n+1)\lambda/2, \tag{1.1}$$

where R is the internuclear distance of the diatomic molecule, θ_L was the orientation of the molecule with regards to the polarisation of the field and $\lambda = 2\pi/p$ is the De Broglie wavelength of the returning electron wavepacket. Using the fact that the harmonic order of a radiated photon in HHG is given by the sum of ionisation energy (I_p) of the molecule and the kinetic energy ($E_{K.E}$) of the returning electron, $\Omega = I_p + E_{K.E}$, the predicted harmonic that the minima would occur is given by

$$\Omega = I_p + \frac{(2n+1)^2\pi^2}{2R^2\cos^2\theta_L}. \tag{1.2}$$

In Fig. 1.2, we compare the calculated harmonic spectrum from a Hydrogen atom (red and black curves) and a Hydrogen molecule (green and dark green curve). We can clearly see a structural interference minimum in the plateau of the H_2 HHG spectrum, the posi-

tion of which is predicted by Eq. (1.2) at the 54th harmonic. However, this interference condition was found to incorrectly predict the position of the minimum of experimentally measured HHG from CO_2 [54] and N_2 [55] because the valence orbitals of these molecules are made up of both s-type and p-type orbitals, unlike H_2, which is made up of purely s-type orbitals, Furthurmore, some studies have suggested that multi-electron effects may be important [56]. In 2009 a generalised two-centre interference condition for HHG from homonuclear diatomic molecules subjected to a linearly polarised laser field that accounts for the orbital geometry and also $s-p$ mixing was introduced [57]. This condition was shown to correctly predict the position of the minima in calculated HHG spectra from H_2, O_2 and N_2 whose HOMOs are composed by s-type, p-type and s-p mixed orbitals, respectively. Two centre interference has also been studied in heteronuclear diatomic molecules, where it was found in one particular theoretical study that the asymmetry of the heteronuclear molecular orbitals leads to some blurring in the interference patterns [58].

The model used to calculate the harmonic spectrum from H_2 in Fig 1.2 employs the Born-Oppenheimer approximation, which means that the electronic and nuclear degrees of freedom are disentangled. This allow us to neglect nuclear motion as it happens on a much larger time scale compared to electronic motion. Therefore the position of the nuclei of the molecular target in this model are assumed to be fixed. For large molecules such as N_2 and O_2 this is a good approximation as the vibration of the heavy nuclei is very small [59]. This is not the case for molecules such as H_2 and D_2 for which the internuclear distance can change within the time the electron ionises and recombines. This effect has been shown to lead to a lower minimum in the harmonic spectrum than previously predicted [50], as well as terminating HHG from these molecules after a few periods of the field, causing a shortening of the attosecond pulse trains and in general leading to a lower HHG efficiency [60, 61]. Nevertheless, in order to isolate the effects of orthogonally polarised fields of quantum structural interference, the Born-Oppenheimer approximation has been employed throughout the work presented in this thesis.

Studies of the above-mentioned two-centre interference for elliptically polarised fields are comparatively few. Most of the studies are focused on the harmonic yield, as a function of the driving-field polarisation [62], or on the ellipticity of the high-order harmonics as a way to probe the anisotropy of a molecular medium [63, 64, 65]. In particular, recent investigations have shown that the minimum related to two-centre interference becomes increasingly blurred and appears to split if the ellipticity of the driving field is increased [66]. Therein, an interference condition for the perpendicular molecular orientation was presented, which was different along the major and the minor polarisation axis of the driving field. The focus of such papers, however, was on the vector character of the HHG transition probabilities [66], and on the ellipticity of the high-order harmonics [65]. So far

the above-mentioned blurring and splitting has not been addressed. Two centre interference patterns in ATI spectra are also possible, with some studies proposing interference conditions for rescattered ATI from diatomic molecules in linearly polarised fields, which can take into account $s - p$ mixing [67]. In Ref. [68], structural two-centre interference in direct ATI spectra from diatomic molecules was analysed as well as temporal interference. In this study they found that increasing field ellipticity blurred the temporal interference, but the spatial interference patterns were unaffected.

Two centre interference can tell us a lot about our target molecule, such as the internuclear separation, alignment of a molecule [53]and the movement of the atomic centres between ionisation time and recombination time which occurs on a femtosecond time scale [50]. The revelation that the minimum could contain information about structure and properties of the target molecule led to orbital tomography, in which the orbital the electron ionises from is reconstructed from the HHG spectra of the target molecule. Two centre interference has also been shown to reveal the information about the strength of *s-p* mixing of molecular orbital to which the electron returns [57, 69] and whether different ionisation and recombination channels play an important role in the final HHG spectra [69, 48]. In fact this is the idea behind HHG spectroscopy, where the modulation of the two centre interference pattern caused by changes in relative amplitude of the different ionisation channels as a function of the molecular alignment are used to track the multi-electron rearrangement on an attosecond timescale [70, 71].

But in order to be able to image molecules with orthogonally polarised fields, one must disentangle the imprints left by the field on the molecular target from the features caused by the field itself. In this thesis, we perform a detailed study of the influence of an orthogonally polarised driving field on the structural interference in HHG, in order to explain the effects found in [66]. We find that the blurring and splitting of interference minima are the result of sub-cycle modifications of the electrons trajectories mentioned in Sec. 1.2.1, caused by the orthogonally polarised field. The field imparts a perpendicular momentum on to the electron trajectories which will depend on their ionisation and recombination time, therefore inducing the electron to return at varying angles with respect to the field. This range of return angles will cause the position the minimum in the spectra to shift differently for each trajectory, leading to blurring.

We then show that we are able to predict the position of the shifted minima for the individual trajectories with a modified two-centre interference condition for diatomic molecules in orthogonally polarised driving fields. This condition holds for arbitrary shapes, relative phase and frequencies of these two fields and in the limit of vanishing perpendicular field, the interference condition in Ref. [57] is recovered. If observable in experiments, it would therefore be possible to extract the electrons angle of return from the modified positions of two centre interference minima, which, as we can see in Fig. 1.2

is a dominant feature in HHG spectra of diatomic molecules. Observing shifted two centre interference in HHG spectra from aligned diatomic molecules has not been accomplished to date. This is mostly likely due to blurring caused by this variation in the return angle for the electron trajectories. In Ref. [54], this blurring was observed experimentally. They found that increasing the ellipticity of the driving field had little effect on the HHG intensity for harmonic orders influenced by destructive two centre interferences compared to those that were not. Here, the expected loss in HHG intensity is compensated by an increase in intensity due to the blurring minimum. This experiment highlights our main motivation of work in this thesis, which is to reduce the blurring observed in [54] and aid in the observation of shifted two centre interference experimentally. With our detailed study of the physics behind this phenomena, we have a better understanding of the conditions that need to be met at the single atom response level, such as field type and phase difference, and the macroscopic phase matching conditions (discussed later in Sec. 1.4), such as gas jet position and pulse duration, in order to achieve observation of the shifted minimum experimentally.

Additionally, understanding how to control an electron's angle of return could prove useful for molecular imaging and orbital reconstruction. For instance, HHG spectroscopy uses the alignment of the molecule to select which channel the electron ionises from when tracking electron hole dynamics [70]. Using this extra degree of freedom could also open up this technique to molecules that are difficult to align. In fact it was shown in Ref. [72] that using an elliptically polarised field allowed for the retrieval of energy and angular dependence of the photorecombination cross section of p-states, which was not possible with linearly polarised fields. Preparing a desired spread of recollision angles could also allow molecular-orbital reconstruction from a tailored single-shot measurement. This would be useful for dynamic processes in which space, energy and time coherence are important. Furthermore, this control over the electron angle could also be useful in other fields such as laser induced electron diffraction (LIED) in which the electrons that are ionised from a molecule are used to probe the molecule when they rescatter on their return [73, 74, 75, 76]. Reconstruction of the molecular orbital can be achieved by retrieving structural information in the diffraction patterns [77].

Moreover, manipulation of the shifted minimum itself can be useful. In Ref. [78] they showed that the minimum could provide a window to reveal contributions to the high harmonic spectrum from other orbitals, which would normally be washed out by the HHG signal from the HOMO. Orthogonally polarised fields could provide more freedom to tweak the window provided by the interference minimum. One should note, however, that there may also be imprints caused by the dynamics of the core [56, 63]. The Coulomb potential, like the driving laser field can modify the trajectories of the propagating electrons [79]. Such effects will not be addressed in this work, but a detailed investigation of

the behaviour of destructive interference in HHG spectra from molecules in orthogonally polarised fields will be helpful when disentangling its effects from the influence of the Coulomb potential in future studies and experiments.

1.3 Modelling strong field phenomena

In order to learn any information about the target atom or molecule from the high harmonic spectra or photo-electron momentum distributions of ATI and NSDI, we must disentangle the imprint on the spectra left by the field from the features related to the target. It is therefore important to chose a theoretical method, for which there are various employed within the strong field community, that allow you to do this.

Numerical methods such as solving the time dependent Schrödinger equation (TDSE) provides a benchmark for other models as there are no physical approximations and solution are close to the experimental result. However, the underlying physics is hard to disentangle. Furthermore, although current computational capabilities mean solving for one-electron systems can be easily done, the numerical effort increases exponentially with the increase in the system's degrees of freedom, requiring a great deal of computer power for more complex systems, [80, 81, 82]. In order to avoid the "experimental wall" one needs to employ all sorts of approximations in order model these phenomena. Classical methods do just this and approximate the behaviour of the quantum mechanical wavefunction using an ensemble of classical trajectories that the electron can follow when in the continuum. This provides insight into the physics of the phenomena, which the numerical methods above could not. It could predict the energy in which a high harmonic spectrum would cut-off, but it could not reproduce the interference patterns, plateau or cut-off when calculating the harmonic spectrum.

The strong field approximation (SFA) [83] is a successful model that treats the problem semi-analytically, providing a transparent physical interpretation in terms of electron orbits, while retaining quantum-mechanical features such as spatial and temporal interference. For this reason the SFA is the model of choice in this study as it allows us to assess these difference types of quantum interference and understand how their signatures in high harmonic spectra and photo-electron momentum distributions are affected by the introduction of a second orthogonally polarised field. The main assumptions of the SFA are that if the electron is in the continuum any influence from the binding potential of the atom or molecule will be ignored. This is done by describing the free electrons in the continuum as field dressed plane waves called Volkov states [84]. In turn the influence of the laser field will be ignored when the electron is bound. Although these assumptions are the reasons for its success, they can lead to short comings and a loss of physics when modelling strong field phenomena. For instance the two centre interference minimum

for N_2 has never been observed experimentally [25, 85, 86] despite being predicted to be present using SFA models. In Ref. [87], the influence of the field on the HOMO of N_2 was included, showing that the missing structural minimum was due to a distortion of the HOMO of N_2 by the field. The SFA is also unable to reproduce certain features in the spectra of strong field phenomena such as the fan-shaped structure in the photo-electron momentum distributions of direct ATI [88, 89, 90, 91, 92]. This is because the origin of these features are a consequence of the presence and influence of the Coulomb potential modifying the trajectories of the electrons in the continuum, which is not included in this model. These assumptions also mean that the SFA is not gauge invariant, yielding different results depending on whether the velocity or length gauge of the Hamiltonian are used in the computation. If the Schrödinger equation is solved exactly, both gauges would produce equivalent results. Therefore, it is important to choose the appropriate gauge when employing the SFA, which is a hotly debated subject in the strong field community. In the work that follows the length gauge has been used as it reproduces structures associated with two centre interference patterns which is one of the main focuses of this study. In the velocity gauge these patterns are absent as they are shifted beyond the cut off of HHG [93, 94, 95]. Nevertheless, the SFA is a very powerful and highly flexible model allowing the analysis of the quantum mechanical aspects of strong field phenomena, such as interference, using a intuitive picture in terms of electron trajectories. In fact in Ref. [96] it was shown that the SFA can still be employed to model HHG spectra from more complex molecules such acetylene (C_2H_2) and allene (C_3H_4). The work in this thesis has been done within the framework of the SFA utilising the single-active electron (SAE) and single-active orbital approximations, which mean only the least bound electron and the HOMO are assumed to contribute to most of the physics of the phenomena studied. It is also assumed that ground state depletion and electron transitions to different continuum states do not occur and that the all other dynamics and the core are frozen. Such effects as well as imprints caused by the dynamics of the core [56, 63], will not be addressed in this work. In our study of HHG we employ intense orthogonally polarised fields on diatomic targets and similarly to other studies, which are performed within the strong field approximation we have extended it for molecular systems [97, 59, 98, 93, 94, 69, 99, 100, 57, 66, 68].

1.4 Macroscopic propagation of HHG

It is a reasonable question to ask, whether features found when modelling the HHG spectrum using the SFA can be seen in experimentally measured HHG spectra. High harmonic radiation generated and measured in the lab is not observed from a single atom or molecule interacting with a strong laser field. Instead it is the coherent sum of all the

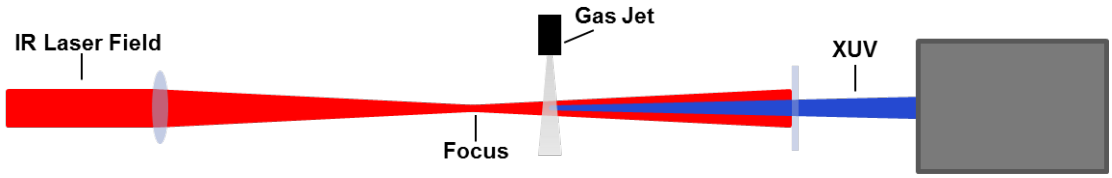

Figure 1.3: Simple representation of the experiment set-up used to measure HHG in the laboratory

constructively interfering harmonics, generated from all the atoms or molecules supplied by the gas jet that are interacting with the strong laser field [101]. Are the features lost in the macroscopic high harmonic response and do they survive propagation into the far field? At this level phase matching has a considerable influence over the resultant XUV field that is measured in the lab [102, 103], where the phase of newly generated harmonics must be in phase with the phase front of the already propagating harmonics generated earlier. Whether the harmonics will phase match constructively or destructively depends on the intensity and phase of the driving laser across the interaction region, which is where the gas jet and the strong laser field interact. Because these properties of the laser field vary across the gas jet causing a variation at the single atom response level. At the single atom response level the phase of the emitted harmonic will depend on the trajectory the electron takes while propagating in the continuum. For any given harmonic on the plateau region of the high harmonic spectrum there are two dominant paths. Because these two paths spend a different amount of time propagating in the field they accumulate different phases. This means that it is possible for the two trajectories to phase match differently giving us the opportunity to suppress one of the trajectories with well chosen macroscopic conditions [104, 105]. This type of selection has been used successfully in the past to optimise attosecond pulse production [104, 101]. In fact, it has even been shown that to obtain clear enough interference patterns between both orbits requires a very delicate tuning on the propagation conditions [44, 106]. In general placing the gas jet after the focus gives rise to good phase matching condition for the short trajectory and placing before the focus gives good phase matching conditions for the long trajectory.

What must also be taken into account is how the medium in the interaction region affects the propagating IR and XUV laser fields. Effects such as linear dispersion and absorption by free-electron and neutral atoms can reshape the driving pulse and affect the generated propagating harmonics differently. After this propagation through the interaction region, the high harmonic radiation must propagate to the far-field through a vacuum towards the detector where is it measured. In order to model experimentally

measured HHG seen in the laboratory one needs to describe the singe atom or molecule response the laser matter interaction as well as the collective macroscopic response. In this study we follow the example of [101, 107] and model the single atom response using the strong field approximation allowing us to keep our intuitive description in terms of trajectories and numerically integrate the Maxwell's wave equation to model the experimental data. In doing so it allows us to understand if features we find modelling HHG at the single molecule response level survive propagation effects and are hence observable in an experiment. It is therefore a useful tool that can be used to encourage and facilitate the setting up of an experiment and is helpful in determining the preferable parameters and conditions required to observe the desired features. Of course this model incorporates the SFA and does not take into account the effect of the core on the trajectories while propagating and retains all the problems mentioned in Sec 1.3. In Ref. [108], a numerical integration of the TSDE and the SFA were compared and were found to disagree on which trajectory contributes more to the spectrum, with the TSDE predicting the shortest and the SFA predictive the second shortest. This leads to discrepancies in macroscopic prediction. Nevertheless, modelling the macroscopic harmonic response using the SFA at the single molecule response level is a very powerful, controllable model, which avoids the "exponential wall" when computing systems with increasing degrees of freedom such as molecules.

1.5 Structure of the thesis

The structure of this thesis is organised as follows. In Chapter 2 we present the basic formalism for the ionisation of an electron by a laser field from a single active electron system and employed the SFA to it. This will then be used later in in Chapters 3 and 8 to derive the SFA transition amplitude for direct HHG and ATI, respectively.

In Part II we focus on high harmonic generation (HHG) and derive the HHG transition amplitude employing the SFA derived in Chapter 2 to which we will then apply the saddle point approximation and uniform approximation. This model will be extended to a diatomic molecular system in Sec 3.6 and a modified two centre interference condition for orthogonally polarised fields will be presented in Sec 3.7. The model is extended further to the macroscopic harmonic response level in Sec 3.8.

In Chapters 4 to 7, we present all our results regarding HHG from diatomic molecules in orthogonally polarised fields.

In Chapter 4 we compute HHG spectra at the single molecule response level using a bichromatic field composed of two orthogonal, linearly polarised waves. We show that the orthogonally polarised fields introduce an effective dynamic shift in the angle for which the two-centre interference maxima and minima occur. This angle depends

on the ratio between the field-dressed momentum components of the returning electron parallel and perpendicular to the major polarisation axis along each possible orbit, and therefore incorporates the electrons angle of return. It is shown that this dynamic shift is responsible for a blurring and splitting similar to that observed in Ref. [66].

In Chapter 5 we model the macroscopic harmonic response and propose the optimal conditions for observing these shifted two centre interference minima. We use phase matching conditions and polarisation gating, so these minima can be measured experimentally with the possibility of extracting the electrons angle of return.

In Chapter 6 we investigate two centre interference in the elliptically polarised fields. We propose a new opportunity in which one may observe the dynamic shift of the two centre interference, without the need to remove trajectory contributions through phase matching at the macroscopic harmonic response level. We also discuss the pros and cons of using an elliptical field over an orthogonal two colour field.

In our final investigation of HHG from diatomic molecules in Chapter 7, we show that the typical suppression in the spectra associated to nodal planes is distorted, and that this distortion can be employed to map the electron's angle of return to its parent ion. In Sec 7.2, we show that the velocity form of the dipole operator is superior to the length form in providing information about this distortion, although both forms introduce artefacts that are absent in the actual momentum-space wavefunction.

In Part III we move the focus of this thesis to the direct ATI. In Chapter 8, using the derivation of the SFA in Chapter 2, we derive the transition amplitude for the direct ATI mechanism to which we employ the saddle point approximation. We present our results from our investigation of temporal interference in direct ATI momentum distribution maps. In Sec 9.1, we identify a type of intra-cycle interference that is often overlooked in other studies. Using an orthogonally polarised field we show in Sec 9.2 that the momentum distributions for individual trajectories separate, leading to a reduction in intra-cycle interference.

Chapter 2

Strong-field approximation (SFA)

In this chapter we present the theoretical approach used to investigate both ATI and HHG in linearly and orthogonally polarised fields. The SFA approach allows us to analyse the quantum mechanical aspects of ATI and HHG using a intuitive picture in terms of electron trajectories. Below we introduce the basic formalism for the ionisation of an electron by a laser field from a single active electron system to which the SFA will be employed. This will then be used in Chapters 3 and 8 to derive the SFA transition amplitude for HHG and direct ATI.

We can begin by evolving the wavefunction $|\Psi(t')\rangle$ from a time t', before the laser is turned on, to a time t when the laser field is turned on using,

$$|\Psi(t)\rangle = U(t,t')|\Psi(t')\rangle. \tag{2.1}$$

$U(t,t')$ is the time evolution operator given by

$$U(t,t') = \mathcal{T}\exp[-\int_{t'}^{t} H(\tau)\mathrm{d}\tau], \tag{2.2}$$

where $\mathcal{T}$ is the time-ordering operator. It evolves the wavefunction under the influence of the full Hamiltonian, given by

$$H = H_0 + H_I(t), \tag{2.3}$$

which satisfies

$$i\frac{\partial}{\partial t}|\Psi(t)\rangle = H|\Psi(t)\rangle. \tag{2.4}$$

In Eq. (2.3), H_0 is the field-free Hamiltonian and $\mathrm{H}_I(\mathrm{t})$ is the interaction Hamiltonian of the atom or molecule with the laser field. The field-free Hamiltonian is given by

$$H_0(t) = \frac{\hat{\mathbf{p}}^2}{2} + V(r), \tag{2.5}$$

which satisfies,

$$i\frac{\partial}{\partial t}|\Psi(t)\rangle = H_0|\Psi(t)\rangle, \tag{2.6}$$

where $\hat{\mathbf{p}}^2/2$ is the kinetic energy of the electron and V(r) is the Coulomb potential of the system. The expression for the interaction Hamiltonian depends on the gauge. In the length gauge it is given by

$$H_I^{(l)}(t) = \mathbf{r}\cdot\mathbf{E}(t), \tag{2.7}$$

and the velocity gauge by

$$H_I^{(v)}(t) = -\nabla\cdot\mathbf{A}(t) + \frac{\mathbf{A}^2(t)}{2} \tag{2.8}$$

If the Schrödinger equation is solved exactly both gauges are equivalent, but if it is solved using approximations, such as the strong field approximation the invariance is broken and the two gauges yield different results. In the work that follows the length gauge has been used so that the interaction Hamiltonian H_I is given by Eq. (2.7). We can now make use of the following Dyson equation

$$U(t,t') = U_0(t,t') - i\int_{t'}^{t} \mathrm{d}t'' U(t,t'')H_I(t'')U_0(t'',t'), \tag{2.9}$$

where $U_0(t,t') = e^{-iH_0(t-t')}$ is the field-free time evolution operator which evolves the system according to the field-free Hamiltonian given by Eq. (2.5) and satisfies

$$\begin{aligned} i\frac{\partial}{\partial t}U_0(t,t') &= H_0(t)U_0(t,t') \\ -i\frac{\partial}{\partial t'}U_0(t,t') &= U_0(t,t')H_0(t'). \end{aligned} \tag{2.10}$$

Substituting Eq. (2.9) into Eq. (2.1) gives us,

$$|\Psi(t)\rangle = U_0(t,t')|\Psi_0(t')\rangle - i\int_{t'}^{t} \mathrm{d}t'' U(t,t'')H_I(t'')U_0(t'',t')|\Psi_0(t')\rangle \tag{2.11}$$

The first term in this equation describes the evolution of a bound electron under the influence of the field-free Hamiltonian from time t' to time t. It does not feel the laser field and does not contribute to ionisation. The second term however, describes a system that is initially evolving without the presence of the laser field, where it accumulates phase described by the field-free evolution operator. At time t'' the field turns on and the bound electron interacts with the laser field described by the interaction Hamiltonian $H_I(t'')$, which causes a transition to a continuum state. The evolution of the system is then described by the complete time evolution operator $U(t,t'')$ in which the electron

interacts with the laser field and the field-free atomic potential, via the full Hamiltonian. So far no approximations have been made and Eq. (2.11) is an exact solution of Eq. (2.4). In this work the laser fields of interest are strong, with intensities of $I > 10^{13}$ W/cm^2 comparable to that the atomic potential. This means we can make the approximation that when the electron is in the continuum it is dominated by the laser field and thus we can neglect the influence of the Coulomb potential. This is the strong field approximation which we can employ by using an approximate time evolution operator called the Volkov propagator, given by

$$U_V(t, t') = e^{-\int_{t'}^{t} H_V(\tau) \mathrm{d}\tau}. \tag{2.12}$$

The Volkov propagator evolves the wavefunction according to the Volkov Hamiltonian, which in the length gauge reads,

$$H_V(t) = \frac{\hat{\mathbf{p}}^2}{2} + \mathbf{E}(t) \cdot \mathbf{r}, \tag{2.13}$$

and satisfies

$$\begin{aligned} i\frac{\partial}{\partial t} U_V(t, t') &= H_V(t) U_V(t, t') \\ -i\frac{\partial}{\partial t'} U_V(t, t') &= U_V(t, t') H_V(t'). \end{aligned} \tag{2.14}$$

We employ the SFA to Eq. (2.11) by replacing the complete time evolution operator $U(t, t')$ with the Volkov time evolution operator $U_V(t, t')$, giving us

$$|\Psi(t)\rangle = U_0(t, t')|\Psi_0(t')\rangle - i \int_{t'}^{t} \mathrm{d}t'' U_V(t, t'') H_I(t'') U_0(t'', t')|\Psi_0(t')\rangle, \tag{2.15}$$

where the first term in the equation describes the evolution of an electron that has not ionised and the second term describes ionisation of an electron, after which it's evolution is only influenced by the laser field. Unlike Eq. (2.11), the advantage of Eq. (2.15) is that the solution to the Volkov time evolution operator is known analytically.

As successful as the SFA has been at modelling strong field phenomena and giving us insights into the mechanics behind them, there are some shortcomings that all come from the fact that the Coulomb potential is ignored as part of the approximation. This has the following repercussions:

1. The propagation of the electron is not correctly modelled as the Coulomb potential would in reality modify the trajectories of the electrons.

2. The ionisation amplitudes are under-estimated because the potential in the SFA is assumed to be zero range. For a long range Coulomb potential the barrier would be

smoother and additional ionisation pathways would be provided via highly excited states.

3. Volkov states are dependent on the gauge of the Hamiltonian. This leads to different results when using the length and velocity gauges to calculate the photoelectrons and high-order harmonic spectra.

4. The Volkov states used to approximate the continuum states are not orthogonal to the ground state. This results in an over complete basis set which leads to further inaccuracies in the prefactor. In particular it leads to a loss of translation invariance when the length form of the dipole operator used to calculate HHG spectra. The form of dipole is discussed in more detail in Chapter 3.

Nonetheless, despite these shortcomings the SFA is a very powerful model that allows the analysis of the quantum mechanical aspects of strong field phenomena, such as interference, via a clear and intuitive picture of electron trajectories.

Part II

High-order harmonic generation

Chapter 3

Theoretical background (HHG)

In this Chapter we present the theoretical approaches used to investigate HHG in orthogonally polarised fields. We follow the example of [109] and apply the SFA derived in Chapter 2 to HHG to get the transition amplitude within the framework of the SFA. The saddle point and uniform approximations are then employed at the single atom response level for linearly polarised fields. We will consider how this model is modified if orthogonally polarised fields are used in Sec 3.5 and extend it for a molecule by approximating the highest occupied molecular orbital (HOMO) using a linear combination of orbitals (LCAO) in Sec 3.6. We will then present a modified structural interference condition in Sec 3.7 that can be used to predict the position of the minima in the HHG spectrum for any field composed of two orthogonal linearly polarised waves. In Sec 3.8 we extend our model for HHG from the single atom response level to the macroscopic harmonic response level. By doing so we can understand whether features found at the single molecule response level can survive harmonic propagation and essentially be observed in an experimental setting. This is done by numerically integrating Maxwell's wave equation to model experimental data.

3.1 Single-atom response

Light emitted by an accelerating charge is proportional to the dipole acceleration

$$\mathbf{a}(t) = \ddot{\mathbf{D}}(t) = \frac{\partial^2}{\partial t^2}\mathbf{D}(t). \tag{3.1}$$

where $\mathbf{D}$(t) is the laser induced dipole given by the expectation value of the dipole moment, $\hat{\mathbf{d}}$,

$$\mathbf{D}(t) = \langle \Psi(t) | \hat{\mathbf{d}} | \Psi(t) \rangle. \tag{3.2}$$

Hence, in order to calculate the harmonic spectrum emitted from an atom or molecule in strong laser field one must calculate the Fourier transform of the second derivative of the expectation value of the dipole operator along the field polarisation given by

$$\mathbf{a}(\omega) = \frac{1}{\sqrt{2\pi}} \int_{-\infty}^{\infty} e^{-i\omega t} \ddot{\mathbf{D}}(t) \cdot \hat{e}_\eta \mathrm{d}t, \tag{3.3}$$

where η and ω are the field polarisation direction and the angular frequency of the driving laser frequency, respectively. If we consider a pulse of length T starting at time t=0, Eq. (3.3) becomes

$$\begin{aligned} \mathbf{a}(\omega) &= \frac{1}{\sqrt{2\pi}} \int_{0}^{T} e^{-i\omega t} \ddot{\mathbf{D}}(t) \cdot \hat{e}_\eta \mathrm{d}t \\ &= \frac{1}{\sqrt{2\pi}} \left(e^{-i\omega T} \dot{\mathbf{D}}(T) + i\omega e^{-i\omega T} \mathbf{D}(T) - \omega^2 \int_{0}^{T} e^{-i\omega t} \mathbf{D}(t) \mathrm{d}t \right) \cdot \hat{e}_\eta, \end{aligned} \tag{3.4}$$

The first two terms in the Eq. (3.4) are dependent on the final momentum and position of the returning wavefunction. These terms grow with the length of the simulation giving rise to background noise when calculating the harmonic spectrum from intense driving laser fields [110]. For this reason they can be neglected, giving us

$$\mathbf{a}(\omega) = -\frac{\omega^2}{\sqrt{2\pi}} \int_{0}^{T} e^{-i\omega t} \mathbf{D}(t) \cdot \hat{e}_\eta \mathrm{d}t. \tag{3.5}$$

The harmonic yield can then be found by calculating the absolute value of Eq. (3.5)

$$S(\omega) = |\mathbf{a}(\omega)|^2. \tag{3.6}$$

Following [109], we can calculate the harmonic spectrum using the expectation value of the dipole moment, given by Eq. (3.2). We can employ the SFA by substituting Eq. (2.15) into the expectation dipole moment, giving us

$$\begin{aligned} D(t) = &\langle \Psi_0(t) | U_0(t,t'') \hat{\mathbf{d}} U_0(t'',t') | \Psi_0(t') \rangle \\ &- i \int_{-\infty}^{t} \mathrm{d}t \langle \Psi_0(t) | U_0(t,t'') \hat{\mathbf{d}} U_V(t'',t) H_I(t) U_0(t,t') | \Psi_0(t') \rangle \\ &+ i \int_{-\infty}^{t} \mathrm{d}t' \langle \Psi_0(t) | U_0(t,t') H_I(t') U_V(t',t'') \hat{\mathbf{d}} U_0(t'',t') | \Psi_0(t') \rangle \\ &- i \int_{-\infty}^{t} \mathrm{d}t \int_{-\infty}^{t} \mathrm{d}t' \langle \Psi_0(t) U_0(t,t') H_I(t') U_V(t',t'') \hat{\mathbf{d}} U_V(t'',t) H_I(t) U_0(t,t') | \Psi_0(t') \rangle. \end{aligned} \tag{3.7}$$

The first term vanishes due to the symmetry of the wavefunction and the dipole operator and the last term describing continuum-continuum transitions is neglected as it is assumed their contributions to the dipole are negligible. Eq. (3.7) now reads,

$$\mathbf{D}(t) = i \int_{-\infty}^{t} \mathrm{d}t' \langle \Psi_0(t) | \hat{\mathbf{d}} U_V(t,t') H_I(t') | \Psi_0(t') \rangle + c.c, \tag{3.8}$$

where c.c denotes the complex conjugate. Utilizing $|\Psi_0(t)\rangle = e^{-iE_0 t}|\Psi_0\rangle$ where E_0 is the bound energy of the state and expressing the Volkov time-evolution operator in terms of Volkov states

$$U_V(t,t') = \int \mathrm{d}^3\mathbf{p} |\Psi_{\mathbf{p}}^V(t)\rangle\langle\Psi_{\mathbf{p}}^V(t')|, \tag{3.9}$$

one can rewrite Eq. (3.8) giving us

$$\mathbf{D}(t) = i \int_{-\infty}^{t} \mathrm{d}t' \int \mathrm{d}^3\mathbf{p} \langle \Psi_0 | \hat{\mathbf{d}} | \Psi_{\mathbf{p}}^V(t)\rangle\langle\Psi_{\mathbf{p}}^V(t')|H_I(t')|\Psi_0\rangle e^{-iE_0(t-t')} + c.c. \tag{3.10}$$

We can approximate the electron in the continuum by the Volkov states $|\Psi_{\mathbf{p}}^V(t)\rangle$, which in the length gauge are given by plane waves (exp[i**kr**]) with a kinetic momentum **k**(t) = **p** + **A**(t), so that

$$|\Psi_{\mathbf{p}}^V(t)\rangle = e^{-iS(t)}|\mathbf{p} + \mathbf{A}(t)\rangle, \tag{3.11}$$

where

$$S(t) = \frac{1}{2}\int_{-\infty}^{t} \mathrm{d}t''[\mathbf{p} + \mathbf{A}(t'')]^2. \tag{3.12}$$

Here, **p** and **A**(t) are the canonical momentum and the vector potential of the laser field, respectively. Here the spatial dependence of the field has been neglected by employing the dipole approximation. This approximation is valid as the wavelength of the driving field is much larger than the De Broglie wavelength of the returning electronic wavepacket. The vector potential can therefore be related to the electric field via $\mathbf{E}(t) = \partial\mathbf{A}(t)/\partial t$. Using Eq. (3.11) and (3.12) and taking the Fourier transform of Eq. (3.10) over all time, one gets the following transition amplitude for HHG within the framework of the SFA,

$$\mathbf{M}(\Omega) = -i \int_{-\infty}^{\infty} \mathrm{d}t \int_{-\infty}^{t} \mathrm{d}t' \int \mathrm{d}^3\mathbf{p}\, \mathbf{d}_{\mathrm{rec}}^*(\mathbf{p}+\mathbf{A}(t))\mathbf{d}_{\mathrm{ion}}(\mathbf{p}+\mathbf{A}(t'))e^{-iS(\mathbf{p},\Omega,t,t')} + c.c, \tag{3.13}$$

where

$$\mathbf{d}_{\mathrm{rec}}(\mathbf{p}+\mathbf{A}(t)) = \langle \mathbf{p}+\mathbf{A}(t)|\hat{\mathbf{d}}|\Psi_0\rangle, \tag{3.14}$$

and

$$\mathbf{d}_{\mathrm{ion}}(\mathbf{p}+\mathbf{A}(t')) = \langle \mathbf{p}+\mathbf{A}(t')|\hat{\mathbf{r}}\cdot\mathbf{E}(t')|\Psi_0\rangle, \tag{3.15}$$

are the recombination and ionisation dipole matrix elements or prefactors, respectively. All the information about the atom or molecule are contained within these prefactors. The semi-classical action is given by

$$S(\mathbf{p},\Omega,t,t') = \frac{1}{2}\int_{t'}^{t}[\mathbf{p}+\mathbf{A}(\tau)]^2\mathrm{d}\tau - E_0(t-t') + \Omega t. \tag{3.16}$$

3.2 Form of the dipole operator

The recombination prefactor [Eq. (3.14)] is dependent on the form of the dipole operator, $\hat{\mathbf{d}}$. If the wavefunction is an exact solution to the Hermitian Hamiltonian, the forms of the dipole expectation value are equivalent. However, because of the approximations made in the SFA, the different forms of this operator will lead to differing results. For instance, different forms of the recombination dipole matrix can influence the structural interference in the HHG spectrum, [99, 111, 112]. Which form to use is still a hotly debated subject in the strong field community [113, 114, 115]. The acceleration and velocity forms yield acceptable results when compared to the TDSE, but due its computation ease and superior accuracy, the velocity form is generally considered the best [112]. Nevertheless, the length form has been successfully employed many times within strong field research [25, 66, 65, 115] and in some studies found to produce better results when compared to the velocity [99]. For this reason the length form of the dipole expectation value will be used in this work alongside the velocity form. The forms of the dipole operator should not be confused with the gauge [94, 116, 93], which determines how the Hamiltonian is written. Explicitly, the length, velocity and acceleration forms of the dipole operator read $\hat{\mathbf{d}}^{(l)} = \hat{\mathbf{r}}$, $\hat{\mathbf{d}}^{(v)} = \hat{\mathbf{p}}$, $\hat{\mathbf{d}}^{(a)} = -\nabla V(\hat{\mathbf{r}})$. The expectation value of the dipole moment in the velocity and acceleration form can be derived from the length form using Ehrenfest's theorem, which uses the Heisenberg equation

$$\frac{\partial}{\partial t}\langle A\rangle = \frac{i}{\hbar}\langle[H,A]\rangle, \tag{3.17}$$

where A is a quantum mechanical operator and H is the Hamiltonian of the system. In this work we calculate the dipole matrix elements in the length and velocity form only and it is useful, in order to calculate these, to express them in terms of bound states of the momentum wavefunction $\psi_0(\mathbf{p})$. In the length form this is achieved by inserting $\hat{\mathbf{d}}^{(l)} = \hat{\mathbf{r}}$ and the position space closure relation in to the recombination prefactor, so that

$$\begin{aligned}\mathbf{d}_{\mathrm{rec}}^{(l)} &= \langle \mathbf{p}|\hat{\mathbf{r}}|\Psi_0\rangle, \\ &= \int \langle \mathbf{p}|\mathbf{r}\rangle\langle \mathbf{r}|\hat{\mathbf{r}}|\Psi_0\rangle \mathrm{d}^3\mathbf{r}, \\ &= \frac{1}{(2\pi)^{3/2}} \int e^{-i\mathbf{p}\cdot\mathbf{r}}\langle \mathbf{r}|\hat{\mathbf{r}}|\Psi_0\rangle \mathrm{d}^3\mathbf{r}, \end{aligned} \tag{3.18}$$

where

$$\langle \mathbf{p}|\mathbf{r}\rangle = \frac{1}{(2\pi)^{3/2}} \int e^{-i\mathbf{p}\cdot\mathbf{r}} \mathrm{d}^3\mathbf{r}. \tag{3.19}$$

Using the fact that that momentum wavefunction and the position operator in momentum space are given by

$$\Psi(\mathbf{p}) = \frac{1}{(2\pi)^{3/2}} \int e^{-i\mathbf{p}\cdot\mathbf{r}}\langle \mathbf{r}|\Psi_0\rangle \mathrm{d}^3\mathbf{r}, \tag{3.20}$$

and

$$\hat{\mathbf{r}} = i\frac{\partial}{\partial \mathbf{p}}, \tag{3.21}$$

respectively, we can express the recombination prefactor in terms of bounds state of the momentum operator,

$$\mathbf{d}_{\mathrm{rec}}^{(l)}(\mathbf{p}) = -i\frac{\partial \Psi_0(\mathbf{p})}{\partial \mathbf{p}}, \tag{3.22}$$

The same can be achieved for the velocity form of the recombination prefactor, where $\hat{\mathbf{d}} = \hat{\mathbf{p}}$, giving us

$$\begin{aligned}\mathbf{d}_{\mathrm{rec}}^{(v)}(\mathbf{p}) &= \langle \mathbf{p}|\hat{\mathbf{p}}|\Psi_0\rangle, \\ &= \int \mathbf{p}\langle \mathbf{p}|\mathbf{r}\rangle\langle \mathbf{r}|\Psi_0\rangle \mathrm{d}^3\mathbf{r}, \\ &= \frac{1}{(2\pi)^{3/2}} \int e^{-i\mathbf{p}\cdot\mathbf{r}}\mathbf{p}\langle \mathbf{r}|\Psi_0\rangle \mathrm{d}^3\mathbf{r}, \end{aligned} \tag{3.23}$$

$$, \tag{3.24}$$

using Eq. (3.20) we get

$$\mathbf{d}_{\mathrm{rec}}^{(v)}(\mathbf{p}) = \mathbf{p}\Psi_0(\mathbf{p}). \tag{3.25}$$

3.3 Saddle point equations

In order to solve Eq. (3.13) one can take advantage of the fact that the action oscillates very quickly in comparison to the prefactor [117]. This means that we can employ the

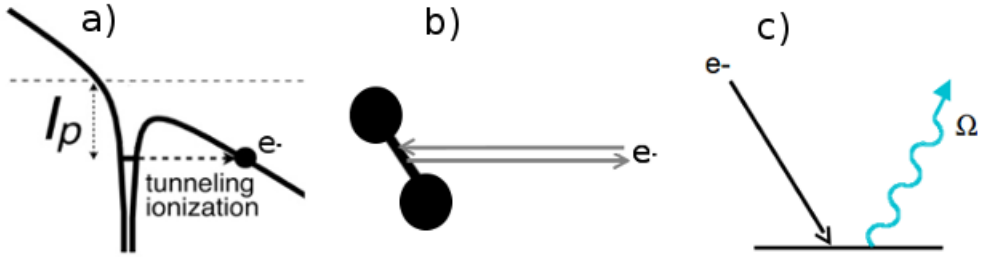

Figure 3.1: Illustration showing the three-step mechanism of HHG

saddle point approximation, by which the stationary points of the semi-classical action can be use to calculate the integral as they make the largest contributions to Eq. (3.13). For HHG the action is a function of three variables, t', $\mathbf{p}$ and t. Therefore we need to find the solutions of $\partial S(\mathbf{p}, t, t')/\partial t' = 0$, $\partial S(\mathbf{p}, t, t')/\partial \mathbf{p} = \mathbf{0}$ and $\partial S(\mathbf{p}, t, t')/\partial t = 0$, which respectively give the following saddle point equations

$$\frac{[\mathbf{p} + \mathbf{A}(t')]^2}{2} + E_0 = 0, \tag{3.26}$$

$$\int_{t'}^{t} \mathrm{d}\tau [\mathbf{p} + \mathbf{A}(\tau)] = \mathbf{0}, \tag{3.27}$$

$$\frac{[\mathbf{p} + \mathbf{A}(t)]^2}{2} + E_0 = \Omega. \tag{3.28}$$

These equations can be related back to the three step model. Eq. (3.26) can be interpreted as the conservation of energy for the active electron upon tunnel ionisation in the first step shown in Fig. 3.1a. The solutions to this equation are complex, this is due to the quantum mechanical nature of tunnel ionisation. Eq. (3.27) imposes a return condition on the propagating electron, fixing its intermediate momentum so that it returns to the site of its release (see Fig. 3.1b). For a diatomic molecule this site is assumed to be its geometrical centre, r = 0. Finally, Eq. (3.28) gives the conservation of energy of the active electron upon recombination in the third step of the HHG mechanism, in which its kinetic energy is converted into a high-harmonic photon of frequency Ω,(Fig. 3.1c).

The major contributions to the momentum integral in Eq. (3.13) come from the region around the value of $\mathbf{p}$ for which the action is stationary. Using Eq. (3.27), we can write an expression for the stationary moment, $\mathbf{p}_\mathrm{s}$,

$$\mathbf{p}_\mathrm{s} = \mathbf{p}_\mathrm{s}(t, t') = \frac{-1}{t - t'} \int_{t'}^{t} \mathrm{d}\tau \mathbf{A}(\tau). \tag{3.29}$$

Using the saddle point method we can approximate the momentum integral by employing a Taylor expansion of the action around the saddle point, $\mathrm{p_s}$,

$$\begin{aligned} S(\mathbf{p},t,t',\Omega) &= S(\mathbf{p}_\mathrm{s},t,t',\Omega) + \frac{\partial S(\mathbf{p}_\mathrm{s},t,t',\Omega)}{\partial \mathbf{p}}(\mathbf{p}-\mathbf{p}_\mathrm{s}) + \frac{1}{2}\frac{\partial^2 S(\mathbf{p}_\mathrm{s},t,t',\Omega)}{\partial \mathbf{p}^2}(\mathbf{p}-\mathbf{p}_\mathrm{s})^2 + ... \\ &\approx S(\mathbf{p}_\mathrm{s},t,t',\Omega) + \frac{1}{2}(t-t')(\mathbf{p}-\mathbf{p}_\mathrm{s})^2. \end{aligned} \tag{3.30}$$

Here, orders higher than the second-order are ignored and since $\mathbf{p}_\mathrm{s}$ is a stationary point the first-order derivatives of the action vanish. Looking back at Eq. (3.16), it is easy to see that we can simplify the second-order terms to $(t-t')$. Inserting Eq. (3.29) into Eq. (3.30), the integral over the intermediate momentum becomes,

$$\begin{aligned} \int \mathrm{d}^3\mathbf{p} D(\mathbf{p}_\mathrm{s},t,t',\Omega) e^{-iS(\mathbf{p},\Omega,t,t')} &\approx D(\mathbf{p}_\mathrm{s},t,t') e^{-iS_{\mathbf{p},\Omega}(t,t')} \int e^{-i\frac{1}{2}(t-t')(\mathbf{p}-\mathbf{p}_\mathrm{s})^2} \mathrm{d}^3\mathbf{p}, \\ &\approx \left(\frac{2\pi}{t-t'}\right)^{3/2} D(\mathbf{p}_\mathrm{s},t,t') e^{-iS_{\mathbf{p},\Omega}(t,t')}, \end{aligned} \tag{3.31}$$

where $D(\mathbf{p}_\mathrm{s},t,t') = \mathbf{d}^*_\mathrm{rec}(\mathbf{p}_\mathrm{s}+\mathbf{A}(t))\mathbf{d}_\mathrm{ion}(\mathbf{p}_\mathrm{s}+\mathbf{A}(t'))$, which varies more slowly then the action and can be considered constant and moved outside of the integral over the momentum. Inserting Eq. (3.31) into the transition amplitude Eq. (3.13) we get.

$$\mathbf{M}(\Omega) \approx -i\left(\frac{2\pi}{t-t'}\right)^{3/2} \int_{-\infty}^{\infty} \mathrm{d}t \int_{-\infty}^{t} \mathrm{d}t' \; \mathbf{d}^*_\mathrm{rec}(\mathbf{p}_\mathrm{s}+\mathbf{A}(t))\mathbf{d}_\mathrm{ion}(\mathbf{p}_\mathrm{s}+\mathbf{A}(t')) e^{-iS_{\mathbf{p},\Omega}(t,t')} + c.c, \tag{3.32}$$

where $\tau = t-t'$. We can simplify Eq. (3.13) even further and approximate the integrals over time by a sum over the individual trajectories of propagating electron. We start with a Taylor expansion around the saddle points t_s and t'_s,

$$\begin{aligned} S_{\mathbf{p},\Omega}(t,t') = S_{\mathbf{p},\Omega}(t_\mathrm{s},t'_\mathrm{s}) + \frac{1}{2}\Bigg[&\frac{\partial^2 S_{\mathbf{p},\Omega}(t_\mathrm{s},t'_\mathrm{s})}{\partial t^2}(t-t_\mathrm{s})^2 + \\ &+ \frac{\partial^2 S_{\mathbf{p},\Omega}(t_\mathrm{s},t'_\mathrm{s})}{\partial t'^2}(t'-t'_\mathrm{s})^2 + 2\frac{\partial^2 S_{\mathbf{p},\Omega}(t_\mathrm{s},t'_\mathrm{s})}{\partial t_\mathrm{s}\partial t'_\mathrm{s}}(t-t_\mathrm{s})(t'-t'_\mathrm{s})\Bigg]. \end{aligned} \tag{3.33}$$

Where the first-order terms are zero because t_s and t'_s are at stationary points and higher

order terms are ignored. This gives,

$$\begin{aligned}\mathbf{M}(\Omega) &\approx -i\left(\frac{2\pi}{t-t'}\right)^{3/2} D(\mathbf{p}_\mathrm{s}, t_\mathrm{s}, t'_\mathrm{s}) e^{-iS_{\mathbf{p},\Omega}(t_\mathrm{s},t'_\mathrm{s})} \int_{-\infty}^{\infty} \mathrm{d}t \int_{-\infty}^{t} \mathrm{d}t' e^{-i\frac{1}{2}B} \\ &\approx -i\left(\frac{2\pi}{i}\right)\left(\frac{2\pi}{t-t'}\right)^{3/2} \frac{D(\mathbf{p}_\mathrm{s}, \Omega, t_\mathrm{s}, t'_\mathrm{s})}{\sqrt{\det[S''_{\mathbf{p},\Omega}(t_\mathrm{s}, t'_\mathrm{s})]}} e^{-S_{\mathbf{p},\Omega}(t_\mathrm{s},t'_\mathrm{s})} \\ &= \left(\frac{2\pi}{t-t'}\right)^{5/2} \frac{D(\mathbf{p}_\mathrm{s}, \Omega, t_\mathrm{s}, t'_\mathrm{s})}{\sqrt{\det[S''_{\mathbf{p},\Omega}(t_\mathrm{s}, t'_\mathrm{s})]}} e^{-iS_{\mathbf{p},\Omega}(t_\mathrm{s},t'_\mathrm{s})}, \end{aligned} \tag{3.34}$$

where in the first row B is given by

$$B = \frac{\partial^2 S_{\mathbf{p},\Omega}(t_\mathrm{s}, t'_\mathrm{s})}{\partial t^2}(t-t_\mathrm{s})^2 + \frac{\partial^2 S_{\mathbf{p},\Omega}(t_\mathrm{s}, t'_\mathrm{s})}{\partial t'^2}(t'-t'_\mathrm{s})^2 + 2\frac{\partial^2 S_{\mathbf{p},\Omega}(t_\mathrm{s}, t'_\mathrm{s})}{\partial t_\mathrm{s} \partial t'_\mathrm{s}}(t-t_\mathrm{s})(t'-t'_\mathrm{s}). \tag{3.35}$$

As above, the prefactors vary slowly compared to the action, so that we can consider them constant and take them out of the integrals over time. Using Eq. (3.34) we can approximate Eq. (3.13) as a summation of all the saddle point contributions,

$$M(\Omega) = \sum_\mathrm{s} A_\mathrm{s} e^{iS_{\mathbf{p},\Omega}(t_\mathrm{s},t'_\mathrm{s})}, \tag{3.36}$$

$$S_{\mathbf{p}.\Omega}(t_\mathrm{s}, t'_\mathrm{s}) = -\frac{1}{2}\int_{t'_\mathrm{s}}^{t_\mathrm{s}} [\mathbf{p}_\mathrm{s} + \mathbf{A}(\tau)]^2 \mathrm{d}\tau - E_0(t_\mathrm{s} - t'_\mathrm{s}) + \Omega t_\mathrm{s}, \tag{3.37}$$

and

$$A_\mathrm{s} = (2\pi)^{5/2} \frac{\mathbf{d}_\mathrm{ion}(\mathbf{p}_\mathrm{s} + \mathbf{A}(t'_\mathrm{s}))\mathbf{d}^*_\mathrm{rec}(\mathbf{p}_\mathrm{s} + \mathbf{A}(t_\mathrm{s}))}{(t-t')\sqrt{\det S''_{\mathbf{p},\Omega}(t_\mathrm{s}, t'_\mathrm{s})}}, \tag{3.38}$$

where, $\det S''_{\mathbf{p},\Omega}(t_\mathrm{s}, t'_\mathrm{s})$ represents a 2×2 determinant of the second derivative of the action and p_s, t_s and t'_s are the solutions of the saddle point equations.

The solutions of the saddle point equations above can be associated with classical trajectories of the electron in the laser field. For HHG there are two sets of solutions/trajectories per laser half cycle which leave the vicinity of the parent ion and return within one period of the field with the same kinetic energy. These two trajectories are well known and are often referred to as the " long" and " short" orbits [104], referring to the time it takes the electron to propagate along them. Both orbits ionised around the peak of the electric field with the long orbit ionised before the short orbit. When they return, the long orbit recombines after the crossing of the electric field and the short before. Respectively, the real parts of t' and t can be interpreted as the trajectory start and return times. The imaginary parts of these times reflect the quantum nature of these trajectories, for instance, $\mathrm{Im}[t']$ can be associated to the width of the barrier the electron

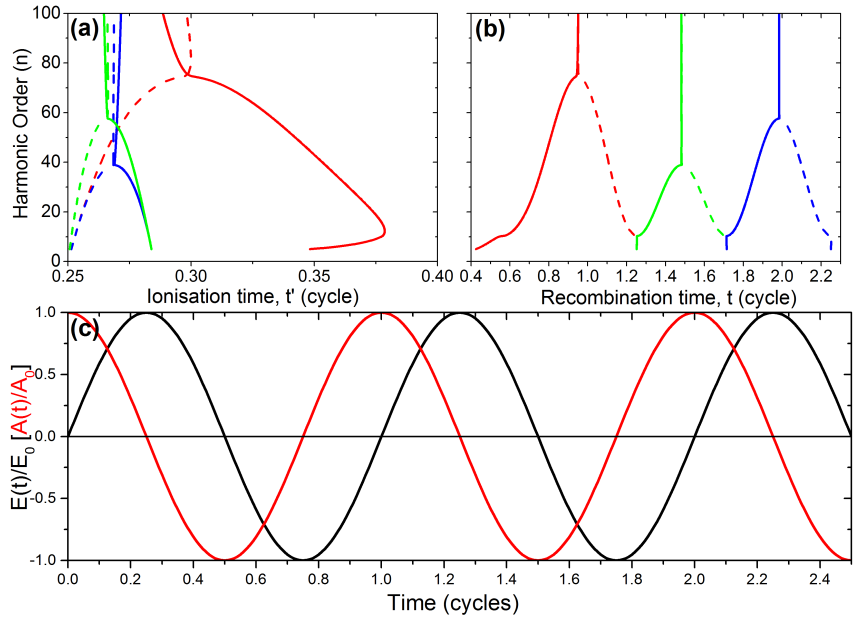

Figure 3.2: Panels (a) and (b) show the start and return times of the electron's propagation in the continuum via the short and long trajectory pair (solid and dashed curves respectively) ionising from a H_2 molecule (ionisation potential, I_p= 0.58 a.u. and internuclear separation, R = 1.4 a.u.) by the driving field described in panel (c). The three shortest electron trajectory pairs ionising from the same half cycle are shown. These trajectories recombined in the second, third or fourth half cycles (red, green and blue curves, respectively). Panel (c) is a schematic representation of the electric field $\mathbf{E}(t)$ (black curve) and the vector potential $\mathbf{A}(t)$ (red curve) of a monochromatic linearly polarised field with a wavelength of $\lambda = 800$ nm and driving intensity $I_0 = 5 \times 10^{14}$ W/cm^2. For simplicity, all fields in panel (c) have been normalised to the electric field amplitude E_0 and vector potential amplitude $A_0 = E_0/\omega$.

tunnels through at the time of ionisation and can be interpreted as the probability of ionisation [83, 118]. The real part of these times have been plotted in Fig. (3.2) which show that the electron typically ionised around the peak of the electric field and recombined at the crossing.

This figure also shows that the time difference between the long and short excursions decreases as the kinetic energy of the electron increases until they converge upon a single set of solutions/trajectory. Electrons returning along this single trajectory will gain the maximum kinetic energy from the field whilst propagating in the continuum. The resultant radiation given off when the electron recombines will be the highest order harmonic in a plateau of harmonics of relatively similar intensity and represents the cut-off of this plateau, after which the yield of the spectrum quickly drops off. Ionising electrons can recombine within one cycle, or spend some more time in the continuum propagating and recombine in the subsequent half cycles. These longer trajectories contribute less to the high harmonic spectrum due to wavepacket spreading, which increases for longer excursions in the continuum.

If the saddle point solutions are well separated, the SPA is well suited to calculating the transition amplitude of HHG. However, as the return kinetic energy increases towards the cut-off, the real parts of the ionisation and recombination times begin to coalesce [see Fig. 3.2]. The trajectories will then pass through a stokes transition, in which the real part of the action for both trajectories are identical

$$\mathrm{Re}[S_i(t_\mathrm{s}, t'_\mathrm{s})] = \mathrm{Re}[S_j(t_\mathrm{s}, t'_\mathrm{s})], \tag{3.39}$$

where i and j denote a pair of trajectories. This is a problem for the SPA, which will no longer be able to treat the solutions as independent because the second derivatives of the action in Eq. (3.36) tends to zero, causing the approximation to become increasingly inaccurate. After this transition the imaginary component of the action $\mathrm{Im}[S_j(t_\mathrm{s}, t'_\mathrm{s})]$ will decrease for one of the trajectories and increase for the other. The trajectory with the increasing imaginary component will begin to diverge. As the kinetic energy of the returning electrons increases, further the trajectories pass through an Anti-Stokes transition in which the imaginary part of the action for both trajectories is identical

$$\mathrm{Im}[S_i(t_\mathrm{s}, t'_\mathrm{s})] = \mathrm{Im}[S_j(t_\mathrm{s}, t'_\mathrm{s})], \tag{3.40}$$

At this point the diverging trajectory is no longer valid and its contributions cause an un-physical increase in harmonic intensity after the cut-off. This problem can be avoided if the diverging saddle is removed by hand [119] after the cutoff, but this leaves us with a cusp around the cut off region of the calculated harmonic spectrum. For this reason, in the work that follows, the SPA is limited to calculating HHG contributions from individual trajectories only.

3.4 Uniform approximation

When calculating the contributions from a pair of trajectories to the HHG spectrum, we employ the uniform approximation (UA). The advantage of this approximation is that it minimises cusps around the cut-off and produces a smooth transition across the stokes line. This is achieved by expanding the action to orders higher then the second-order used for the SPA. We can then calculate the transition amplitude, using contributions from a pair of trajectories, i and j, using two equations. The first calculates the transition amplitude before the cut-off

$$\begin{aligned} M_{i+j} =& \sqrt{2\pi\Delta S/3} e^{i\bar{S}+i\pi/4} \\ & \times [\bar{A}(J_{1/3}(\Delta S) + J_{-1/3}(\Delta S)) + \Delta A(J_{2/3}(\Delta S) - J_{-2/3}(\Delta S))], \end{aligned} \tag{3.41}$$

where,

$$\Delta S = \frac{S_i - S_j}{2}, \bar{S} = \frac{S_i + S_j}{2}, \tag{3.42}$$

$$\Delta A = \frac{A_i - iA_j}{2}, \bar{A} = \frac{iA_i + A_j}{2}, \tag{3.43}$$

and is written in terms of Bessel J functions [3]. To calculate the transition amplitude after the cut-off, we use

$$M_{i+j} = \sqrt{2i\Delta S/\pi} e^{i\bar{S}} [\bar{A} K_{1/3}(-i\Delta S) + i\Delta A K_{2/3}(-i\Delta S)], \tag{3.44}$$

which is written in terms of Bessel K functions. Written in this way the UA does not need any additional information about the electron trajectory pairs, other than the information needed when using the saddle point approximation. Therefore, in order to calculate Eq. (3.41) and Eq. (3.44), all we need S and A, which are the action and prefactors given by Eq. (3.37) and Eq. (3.38), respectively. In fact, when the saddle points are well separated the Eq. (3.41) reduced back to the SPA.

3.5 Orthogonally polarised fields

We will now assume that the external driving field is orthogonally polarised, i.e., made up of two orthogonal linearly polarised laser fields. This implies that the time dependent electric field $\mathbf{E}(t) = -\mathrm{d}\mathbf{A}(t)/\mathrm{d}t$ and the vector potential $\mathbf{A}(t)$ may be written as

$$\mathbf{E}(t) = E_{\parallel}(t)\hat{\epsilon}_{\parallel} + E_{\perp}(t)\hat{\epsilon}_{\perp}, \tag{3.45}$$

and

$$\mathbf{A}(t) = A_{\parallel}(t)\hat{\epsilon}_{\parallel} + A_{\perp}(t)\hat{\epsilon}_{\perp}, \tag{3.46}$$

where the unit vector along the major and the minor polarisation axis are denoted by $\hat{\epsilon}_{\parallel}$ and $\hat{\epsilon}_{\perp}$, respectively. Changing the parameters of the parallel and perpendicular fields, such as the colour or phase difference between them, can help one to tailor any specific field desired. For instance in panel (b) of Fig. 3.3, we show a circularly polarised field that is composed using two orthogonal linearly polarised waves that are out of phase by half a cycle. By decreasing the amplitude of one of the waves, we can make the resultant fields elliptical [panel (c)]. We can compose two-colour orthogonally polarised fields by increasing the frequency of one of the component waves. If for example we chose a frequency ratio of 2:1 between the two waves, we can create an interesting figure of "8" shape [see panel (d)]. With small adjustments to the parameters of these two waves, almost any field shape is possible. Eq. (3.45) and (3.46) modify the transmission

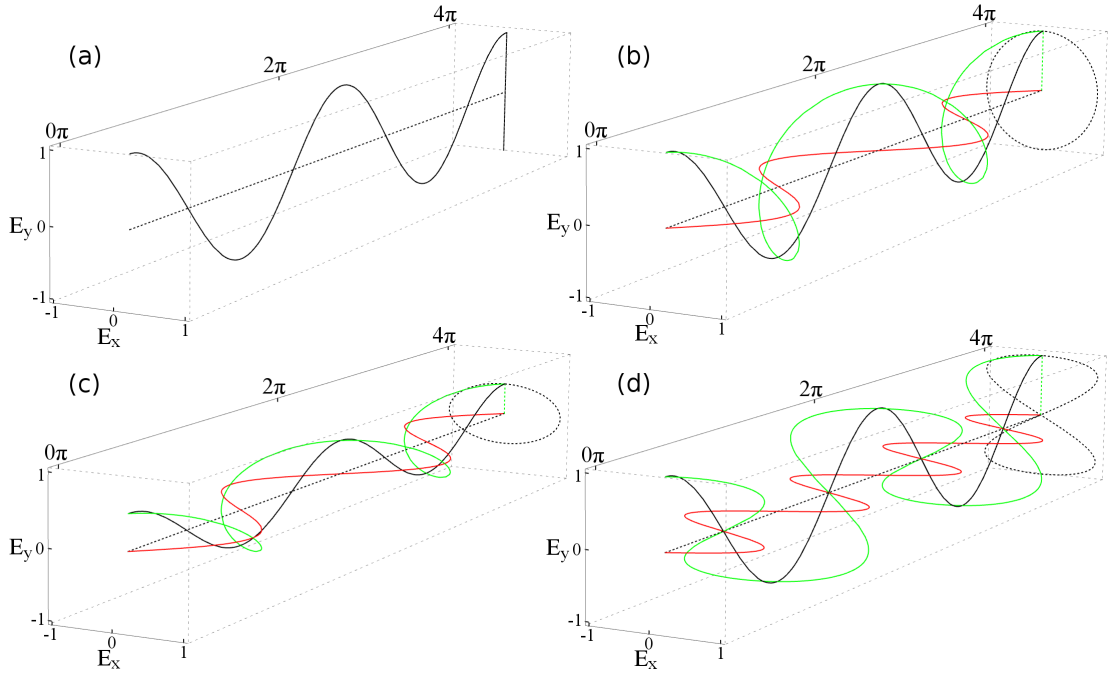

Figure 3.3: Schematic representation of a (a) linearly, (b) circularly, (c) elliptically and (d) two-colour orthogonally polarised field. The black and red curves indicate the parallel and perpendicular waves, respectively. The green curve indicates the field resulting from the combination of the both waves. The amplitude of the fields in the xy plane are indicated by the dashed black curves.

amplitude such that the calculated harmonic spectrum is proportional to

$$S(\Omega) \propto \sum_b |M_b(\Omega)|^2, \tag{3.47}$$

where $b = \parallel, \perp$ refer to the components of the HHG transition amplitude $\mathbf{M}(\Omega)$ parallel and perpendicular to the major polarization axis of the laser field [66, 65]. In this work we compute the transition probability $|M_\parallel(\Omega)|^2$, which gives the polarization component of the harmonics along the major axis. This contribution is much larger than that from the perpendicular component for the ellipticity ranges used, and leads to the main features in the spectra. The parallel component of the transition amplitude is given by

$$M_\parallel(\Omega) = \sum_{\mathrm{s}} (2\pi)^{5/2} \frac{\mathbf{d}_{\mathrm{ion}}(\mathbf{p}_{\mathrm{s}} + \mathbf{A}(t'_{\mathrm{s}}))\mathbf{d}^*_{\mathrm{rec}}(\mathbf{p}_{\mathrm{s}} + \mathbf{A}(t_{\mathrm{s}}))}{(t - t')\sqrt{\det S''_{\mathbf{p},\Omega}(t_{\mathrm{s}}, t'_{\mathrm{s}})}} e^{iS_{\mathbf{p},\Omega}(t_{\mathrm{s}}, t'_{\mathrm{s}})}, \tag{3.48}$$

where the ionisation and recombination prefactors are given by

$$\mathbf{d}_{\mathrm{ion}}(\mathbf{p}) = \langle \mathbf{p} | \hat{\mathbf{r}} \cdot \mathbf{E}_\parallel(t') | \Psi_0 \rangle, \tag{3.49}$$

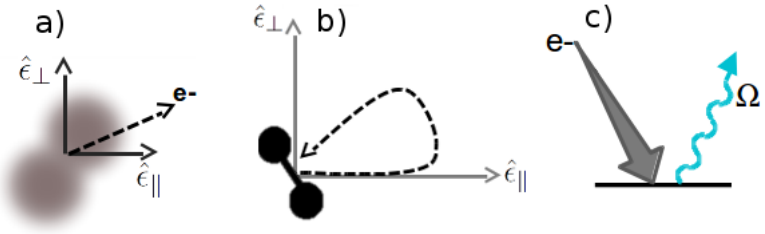

Figure 3.4: Illustration showing the three step mechanism of HHG for an orthogonally polarised field

and

$$\mathbf{d}_{\text{rec}}(\mathbf{p}+\mathbf{A}(t)) = \langle \mathbf{p}+\mathbf{A}(t)|\hat{\mathbf{d}}\cdot\hat{\epsilon}_\parallel|\Psi_0\rangle, \tag{3.50}$$

respectively. The action given by Eq. (3.37) can therefore be re-write as

$$S(t,t',\Omega,\mathbf{p}) = -\frac{1}{2}\int_{t'}^{t} \mathrm{d}\tau[p_\parallel + A_\parallel(\tau)]^2 - \frac{1}{2}\int_{t'}^{t} \mathrm{d}\tau[p_\perp + A_\perp(\tau)]^2 - I_p(t-t') + \Omega t, \tag{3.51}$$

and the saddle-point equations as

$$\frac{\partial S(t,t',\mathbf{p})}{\partial t'} = \frac{[p_\parallel + A_\parallel(t')]^2}{2} + \frac{[p_\perp + A_\perp(t')]^2}{2} + I_p = 0, \tag{3.52}$$

$$\frac{\partial S(t,t',\mathbf{p})}{\partial \mathbf{p}} = \int_{t'}^{t} \mathrm{d}\tau[\mathbf{p}_\parallel + \mathbf{A}_\parallel(\tau)] + \int_{t'}^{t} \mathrm{d}\tau[\mathbf{p}_\perp + \mathbf{A}_\perp(\tau)] = \mathbf{0}, \tag{3.53}$$

and

$$\frac{\partial S(t,t',\mathbf{p})}{\partial t} = \frac{[p_\parallel + A_\parallel(t)]^2}{2} + \frac{[p_\perp + A_\perp(t)]^2}{2} + I_p - \Omega = 0, \tag{3.54}$$

respectively. From Eq. (3.53) we obtain an equation for the stationary momentum for orthogonally polarised fields,

$$\mathbf{p}_{\text{st}} = p_{\text{st}\parallel}\hat{\epsilon}_\parallel + p_{\text{st}\perp}\hat{\epsilon}_\perp, \tag{3.55}$$

where

$$p_{\text{st}\parallel} = \frac{-1}{t-t'}\int_{t'}^{t} A_\parallel(\tau)\mathrm{d}\tau, \tag{3.56}$$

and

$$p_{\text{st}\perp} = \frac{-1}{t-t'}\int_{t'}^{t} A_\perp(\tau)\mathrm{d}\tau. \tag{3.57}$$

This new action (3.51), modifies the motion of the electron in the continuum, giving it perpendicular momentum components as well as parallel. We can see from (3.52), (3.53) and (3.54) that the saddle point equations now incorporate an angle in the processes

they describe [see Fig. 3.4].

In our investigation of quantum interference in HHG, we use an orthogonally polarised field of the form

$$\mathbf{E}(t) = \frac{E_0}{\sqrt{1+\xi^2}} \left[\sin(\omega t)\hat{\epsilon}_{\parallel} + \xi \sin(n\omega t - 2\pi\phi)\hat{\epsilon}_{\perp}\right], \tag{3.58}$$

where the frequency ratio of $n = 1$ gives an elliptically polarised field and $n = 2$ corresponds to an orthogonally polarised two colour (OTC) field, for which the frequency of the field component along the minor axis is twice that of the wave along the major axis. In Eq. (3.58), the strength of the field component along the minor polarisation axis relative to its component along the major axis is determined by ξ, and the relative phase ϕ controls the time delay between both waves. The field has been normalised so that the overall time-averaged intensity $\langle \mathbf{E}^2(t)\rangle_t$ remains constant. This implies that the total ponderomotive energy $U_p = \langle A_{\parallel}^2(t)\rangle_t/2 + \langle A_{\perp}^2(t)\rangle_t/2$ is kept constant for elliptical fields ($n = 1$), and that U_p will decrease with ξ for OTC fields ($n = 2$). For $\xi = 0$ the field in Eq. (3.58) reverts to a linearly field polarised along the parallel axis.[1]

3.6 Extending the SFA to diatomic molecules

Within our model we assume that only the highest occupied molecular orbital (HOMO) contributes to the dynamics. This means that the ionising electron leaves and recombines to and from the HOMO only. Unlike the case for an hydrogen atom in which there is an exact analytical expression for the ground state $|\Psi_0\rangle$, for a molecule there is no such luxury. The simplest way to approximated the HOMO is to use a linear combination of atomic orbitals (LCAO) and to neglect the motion of the atomic centres of the diatomic molecule in question. Hence, the position wavefunction of the HOMO is given by

$$\Psi(\mathbf{r}) = \sum_{\alpha} c_{\alpha} \left[\psi_{\alpha}\left(\mathbf{r} + \frac{\mathbf{R}}{2}\right) + (-1)^{\ell_{\alpha} - m_{\alpha} + \lambda_{\alpha}} \psi_{\alpha}\left(\mathbf{r} - \frac{\mathbf{R}}{2}\right)\right], \tag{3.59}$$

where the sum over α denotes the sum over the atomic orbitals (AO), $\psi_{\alpha}(\mathbf{r})$, $\mathbf{R}$ is the internuclear distance, ℓ_{α} is the orbital angular momentum quantum number, m_{α} is the magnetic quantum number and $\lambda_{\alpha} = m_{\alpha} + 1$ and $\lambda_{\alpha} = m_{\alpha}$ correspond to bonding and antibonding of the linear combination of atomic orbitals, respectively. If they are bonding the overlap of the two AO wavefunctions constructively interfere with each other. This can be seen in Fig. 3.5a and 3.5c, as an area of high probability density connecting the atomic centres. If the orbital wavefunctions are antibonding the overlap will destructively interfere between the two atomic centres, causing an area of vanishing probability density

[1] In the bichromatic case, division of the field amplitude by an overall factor $\sqrt{1+\xi^2/4}$ is required in order to keep U_p constant. This factor, however, excludes an overall constant time-averaged intensity.

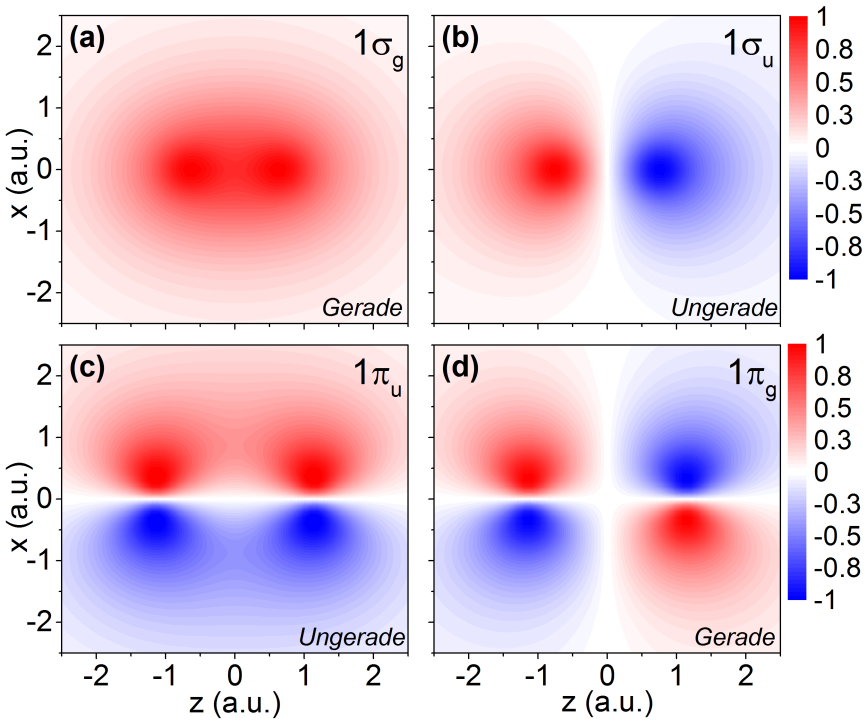

Figure 3.5: Schematic representation of bonding [first column] and anti-bonding [second column] orbitals in positions-space for H_2 [first row] and O_2 [second row]. The H_2 orbitals are $1\sigma_g$ and $1\sigma_u$, and are shown in panels (a) and (b) respectively. These are made up of a linear combination of two atomic s orbitals, where the internuclear separation is $\mathbf{R} = 1.4$ a.u. The O_2 orbitals are $1\pi_u$ and $1\pi_g$, and are shown in panels (c) and (d) respectively. These are made up of a linear combination of two atomic p orbitals, where the internuclear separation is $\mathbf{R} = 2.28$ a.u. The contours have been normalised to the maximum yield in each panel, and the blue [red] lobes correspond to the negative [positive] values of the real parts of the wave functions. In this picture, the internuclear axis is oriented along the z axis.

called a nodal plane, as seen in Fig. 3.5b and 3.5d. The nodal plane parallel to the z axis in Fig. 3.5c and 3.5d, arises from the nodes in the p orbitals around the atomic centres. The resultant molecular orbitals mentioned above are ungerade if the phase of the orbital changes when the molecule is inverted through its centre of symmetry. If the phase stays the same the molecular orbital is labelled gerade. Diatomic molecular orbitals composed of two s-type atomic orbitals have σ-symmetry. If these σ orbitals are bonding they are symmetric when inverted. Fig. 3.5a shows an example of such an orbital called $1\sigma_g$, where g signifies that it is gerade. Antibonding σ orbitals such as the $1\sigma_u$ orbital shown in Fig. 3.5b are ungerade because they are antisymmetric upon inversion of molecule, causing the phases of the orbital to change. In contrast to σ orbitals, molecular orbitals composed of p-type orbital have π-symmetry, which are ungerade if the π orbital are bonding such as $1\pi_u$ shown in Fig. 3.5c and gerade if they are antibonding such as $1\pi_g$

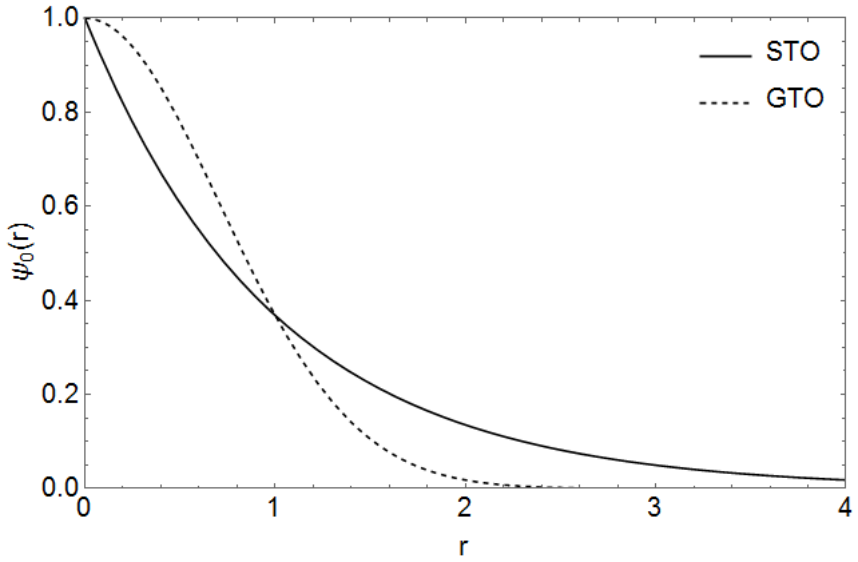

Figure 3.6: A comparison of Gaussian (GTOs) and Slater type orbitals (STOs) where $\zeta = 1$ in Eq. (3.60).

shown in Fig. 3.5d.

For the 1s state of hydrogen centred at the origin the Gaussian type orbitals (GTOs) and Slater type orbitals (STOs) [120, 121] are given by

$$\psi_0^{\mathrm{GTO}}(r) = be^{-\zeta r^2}, \tag{3.60}$$

and

$$\psi_0^{\mathrm{STO}}(r) = e^{-\zeta r}, \tag{3.61}$$

respectively, are often used to approximate AOs. As we can see in Fig. 3.6, the STOs are superior to GTOs, as they represent the electron density in the valence region well and more accurately approximate the cusp at an atomic nucleus. In contrast, GTOs have a quickly diminishing tail as the distance from the nucleus increases and have a vanishing slope at the atomic nucleus. Therefore to more accurately represent AOs using GTOs, it is necessary to use a combination of them. Nevertheless, they are easier to compute, and are widely used in the quantum chemistry community [122]. In this work we use a contraction of GTOs to approximate the atomic wavefunction ψ_α in Eq. (3.59), using the following expression

$$\psi_\alpha(\mathbf{r}) = \sum_{j,\nu} c_{\alpha,j} b_\nu \phi_\nu(\mathbf{r}), \tag{3.62}$$

where

$$\phi_\nu(\mathbf{r}) = \mathrm{x}^i \mathrm{y}^j \mathrm{z}^k e^{-\zeta_\nu \mathbf{r}^2}, \tag{3.63}$$

gives us a Cartesian Gaussian type orbital. When $\ell_\alpha = i + j + k = 0$, Eq. (3.63) gives an s-type orbital and for $\ell_\alpha = i + j + k = 1$, it gives p-type orbitals aligned along the x, y or z coordinate axis.

In practice coefficients b_ν in Eq. (3.62) and exponents ζ_ν in Eq. (3.63) have been optimised and standardised for a given atom in a given basis set. To establish coefficients c_α (Eq. (3.62)) for a given target molecule we used an open access *ab initio* quantum chemistry package, GAMESS-UK [123]. More precisely a set of Hartree-Fock equations is solved self consistently. In this way based on variational principle one can optimize the coefficients c_α by minimising the energy for a given basis set. The values of the LCAO coefficient $c_{\alpha,j}$, expansion coefficient b_ν and the exponential coefficient ζ_ν for the desired basis set are then obtained from calculations performed by this package and used to approximate the wavefunction in Eq. (3.62).

For atomic interactions with strong fields it is normally the valence electrons that will take part. For this reason we use a split valence-shell basis set to approximate the molecular orbital [124, 125, 126], which commonly represents the core with one basis function and the valence orbitals with more than one basis function. There are many variations of split basis contracted GTOs which are labelled using the following X-YZG format. Here, X represents the number of primitive Gaussians summed to describe the inner orbital basis function, whilst Y and Z indicate that the valence orbital are composed of two basis functions. The first basis is a linear combination of Y Gaussian functions, the other of a linear combination of Z Gaussian functions, [127]. For instance in this work we approximate the HOMO of the argon molecule Ar_2 using a 6-31G split basis set. This means for the inner orbitals $1s$, $2s$ and $2p$, are modelled using 6 Gaussians. For the valence orbitals, $3s$ and $3p$, we model them using a set of three Gaussians and a single Gaussian. A split basis set using fewer Gaussians will decrease computation times, but the accuracy of the approximation will be compromised. In terms of picking the best basis set, the bigger the basis set the better if you have the time and computation power. In this work we use the 3-21G basis set when calculating the HOMO of H_2 and the 6-31G basis set when calculating the HOMO of Ar_2 and O_2.

From Eq. (3.18) and (3.25) we know that we can calculate the recombination prefactor using the momentum-space wavefunction given by

$$\psi_a(\mathbf{p}) = \frac{1}{(2\pi)^{3/2}} \int \mathrm{d}^3 r \psi_a(\mathbf{r}) e^{-i\mathbf{r}\cdot\mathbf{p}}. \tag{3.64}$$

For a diatomic molecule this can be rewritten as

$$\Psi(\mathbf{p}) = \sum_{\alpha} e^{\frac{\imath \mathbf{p}\cdot\mathbf{R}}{2}} \psi_{\alpha}(\mathbf{p}) + (-1)^{\ell_\alpha - m_\alpha + \lambda_\alpha} e^{\frac{-\imath \mathbf{p}\cdot\mathbf{R}}{2}} \psi_{\alpha}(\mathbf{p}), \tag{3.65}$$

where,

$$\psi_{\alpha}(\mathbf{p}) = \sum_{j,\nu} c_{\alpha,j} b_{\nu} \phi_{\nu}(\mathbf{p}), \tag{3.66}$$

and

$$\phi_{j,\nu}(\mathbf{p}) = (-\imath \mathbf{p}_{\beta})^{\ell_\alpha} \frac{\pi^{\frac{3}{2}}}{2^{\ell_\alpha} (\zeta_\nu)^{\frac{3}{2}+\ell_\alpha}} e^{-\frac{\mathbf{p}^2}{4\zeta_\nu}}, \tag{3.67}$$

when only s and p types orbitals are considered, which has been done throughout this work.

The reference frame of the molecule is rotated by the alignment angle θ_L with regard to the major polarisation axis of the field. If we consider xz as the polarisation plane, this means that one may relate the $p_\parallel$, $p_\perp$ components to the components p_x, p_z parallel and perpendicular to the molecular axis via

$$\begin{pmatrix} p_\parallel \\ p_\perp \end{pmatrix} = \begin{pmatrix} \cos\theta_L & \sin\theta_L \\ -\sin\theta_L & \cos\theta_L \end{pmatrix} \begin{pmatrix} p_x \\ p_z \end{pmatrix}, \tag{3.68}$$

Using the equations above means we can rewrite the recombination prefactor in the length form as

$$d^{(l)}_{\mathrm{rec}}(\mathbf{p}(t)) = \sum_a c_a \left[e^{i\mathbf{p}(t)\cdot\frac{\mathbf{R}}{2}} + (-1)^{\ell_a - m_a + \lambda_a} e^{-i\mathbf{p}(t)\cdot\frac{\mathbf{R}}{2}} \right] i\partial_{p_\parallel(t)} \psi_a(\mathbf{p}(t)) + \frac{\mathbf{R}}{2} \Lambda(\mathbf{p}), \tag{3.69}$$

where

$$\Lambda(\mathbf{p}) = \sum_a c_a \left[e^{i\mathbf{p}(t)\cdot\frac{\mathbf{R}}{2}} + (-1)^{\ell_a - m_a + \lambda_a} e^{-i\mathbf{p}(t)\cdot\frac{\mathbf{R}}{2}} \right] \psi_a(\mathbf{p}(t)), \tag{3.70}$$

and in the velocity form by

$$d^{(v)}_{\mathrm{rec}}(\mathbf{p}(t)) = \sum_a c_a \left[e^{i\mathbf{p}(t)\cdot\frac{\mathbf{R}}{2}} + (-1)^{\ell_a - m_a + \lambda_a} e^{-i\mathbf{p}(t)\cdot\frac{\mathbf{R}}{2}} \right] p_\parallel(t) \psi_a(\mathbf{p}(t)), \tag{3.71}$$

where $\mathbf{p}(t) = \mathbf{p} + \mathbf{A}(t)$. In Eq. (3.69), the last term on the right hand side arises due to the lack of orthogonality between bound states and continuum states that occurs in the SFA. Its value increases with internuclear separation, blurring the interference caused by the molecules structure. In this work it has been removed by hand which is a widely used procedure (see [93, 116, 94] for discussions).

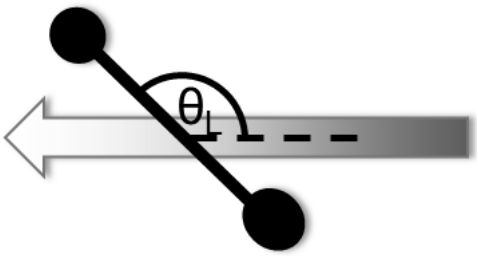

Figure 3.7: Indicates θ_L as the angle between the internuclear separation of the diatomic molecule and major polarisation of the field.

3.7 Two centre interference condition

When high harmonics are generated from aligned molecules, a multi-slit like interference pattern with pronounced maxima and minima form in the HHG spectra. This interference is dependent on the internuclear distance and the orientation of the molecule with respect to the polarisation of the laser field [See Fig. 3.7]. This is a structural effect that results from the electron wave packet recombining to spatially different centres. For the simplest scenario, i.e., a diatomic molecule, these interference patterns have been predicted since the early 2000s [53] (for reviews see, e.g., [128, 129]). Many of such studies have been performed within the strong-field approximation (SFA), which has been generalised to molecular systems (see, e.g., [97, 59, 98, 93, 94, 69, 99, 100, 57, 66]). In 2009, a generalised two-centre interference condition for high-order harmonic generation in homonuclear diatomic molecules subjected to a linearly polarised laser field that accounts for the orbital geometry and also $s-p$ mixing has been introduced [57]. We extend this two centre interference condition so that it takes in to account orthogonally polarised light. To do so we follow the procedure presented in [57] and focus on the explicit expression for the recombination prefactor $d_{\rm rec}$. The ionisation prefactor $d_{\rm ion}$ will only influence the overall intensity in the spectrum, and is not relevant for a qualitative discussion of two-centre interference effects [94]. We first consider the dipole matrix element $d_{\rm rec}(\mathbf{p}+\mathbf{A}(t))$ in the length form (3.69) for the wavefunction (3.59). The quantity of interest is $d^*_{\rm rec}(\mathbf{p}(t)\cdot\mathbf{E}(t))$ along the field-polarisation direction. Explicitly,

$$\begin{aligned} d^*_{\rm rec}(\mathbf{p}(t)\cdot\mathbf{E}(t)) \;&=\; \sum_a c_a\Big[e^{-i\mathbf{p}(t)\cdot\frac{\mathbf{R}}{2}}+(-1)^{\ell_a-m_a+\lambda_a}e^{i\mathbf{p}(t)\cdot\frac{\mathbf{R}}{2}}\Big] \\ &\quad\times(-i)\sum_b \partial_{p_b(t)}\psi^*_a(\mathbf{p}(t))E_b(t), \end{aligned} \tag{3.72}$$

where b= $||$, $\perp$ indicate the components along the major and minor polarisation axis. Eq. (3.72) can be rewritten as

$$d^*_{\rm rec}(\mathbf{p}(t)\cdot\mathbf{E}(t)) \;=\; A_+\cos\left(\mathbf{p}(t)\cdot\frac{\mathbf{R}}{2}\right)+iA_-\sin\left(\mathbf{p}(t)\cdot\frac{\mathbf{R}}{2}\right), \tag{3.73}$$

where

$$A_\pm=\sum_a c_a\left[(-1)^{\ell_a+m_a+\lambda_a}\pm 1\right]\eta(\mathbf{p}+\mathbf{A}(t),t), \tag{3.74}$$

and

$$\eta(\mathbf{p},t)=-i\left[\partial_{p_\parallel}\psi^*_a(\mathbf{p})E_\parallel(t)+\partial_{p_\perp}\psi^*_a(\mathbf{p})E_\perp(t)\right]. \tag{3.75}$$

Note that, because there is an electric field component $E_\perp(t)$ and a field-dressed momentum component $p_\perp(t)$ along the minor polarisation axis, the function $\eta(\mathbf{p},t)$, the s-p mixing embedded in $A_\pm$, will be different from the expressions obtained in Ref. [57] for linear polarisation. Re-writing Eq. (3.76) as

$$d^*_{\rm rec}(\mathbf{p}(t)\cdot\mathbf{E}(t))=\sqrt{A_+^2-A_-^2}\sin\left[\mathbf{p}(t)\cdot\frac{\mathbf{R}}{2}+\alpha\right], \tag{3.76}$$

where $\alpha=\arctan\frac{-iA_+}{A_-}$, we expect interference minima at

$$\alpha+\mathbf{p}(t)\cdot\frac{\mathbf{R}}{2}=n\pi. \tag{3.77}$$

For orthogonally polarised fields we have

$$\mathbf{p}(t)\cdot\frac{\mathbf{R}}{2}=p_{||}(t)\frac{R}{2}\cos\theta_L+p_\perp(t)\frac{R}{2}\sin\theta_L, \tag{3.78}$$

where θ_L is the angle between the molecular internuclear axis and the major polarisation axis of the field. Using

$$\sqrt{(\mathbf{p}+\mathbf{A}(t))^2}\cos\beta=[p_{||}+A_{||}(t)]\cos\theta_L+[p_\perp+A_\perp(t)]\sin\theta_L, \tag{3.79}$$

where

$$\sqrt{(\mathbf{p}+\mathbf{A}(t))^2}=\sqrt{(p_\parallel+A_\parallel(t))^2+(p_\perp+A_\perp(t))^2}, \tag{3.80}$$

and defining

$$\frac{[p_{||}+A_{||}(t)]}{\sqrt{(\mathbf{p}+\mathbf{A}(t))^2}}=\cos\zeta(t,t'), \tag{3.81}$$

$$\frac{[p_\perp+A_\perp(t)]}{\sqrt{(\mathbf{p}+\mathbf{A}(t))^2}}=\sin\zeta(t,t'), \tag{3.82}$$

we obtain

$$\sqrt{(\mathbf{p}+\mathbf{A}(t))^2}\frac{R}{2}\cos(\theta_L-\zeta(t,t'))=n\pi-\alpha, \tag{3.83}$$

where

$$\zeta(t,t')=\arctan\left[\frac{p_\perp+A_\perp(t)}{p_{||}+A_{||}(t)}\right]. \tag{3.84}$$

Physically, this equation demonstrates that a field composed of two orthogonally polarised waves introduces an effective shift $\zeta(t,t')$ in the alignment angle θ_L at which the interference minimum in the harmonic spectrum occurs, with regard to the linearly polarised case. Using Eq. (3.83) and Eq. (3.54) we find that the destructive interference leading to minima in the harmonic spectrum is determined by the expression

$$\Omega=\frac{2[n\pi-\alpha]^2}{R^2\cos^2(\theta_L-\zeta(t,t'))}+I_p. \tag{3.85}$$

This condition holds for arbitrary shapes, relative phase and frequencies of these components. It is applicable to elliptically polarized fields, and to bichromatic fields such as in Ref. [24]. In the limit of vanishing ellipticity, the interference condition in Ref. [57] is recovered.

From Eqs. (3.81) and (3.82) it is clear that the value of ζ depends upon the field dressed momentum components $p_\parallel+A_\parallel(t)$ and $p_\perp+A_\perp(t)$ of the returning electron, and hence on its return time t along each orbit. Furthermore, $p_\parallel$ and $p_\perp$ are functions of the return and ionisation times t and t' according to the saddle-point Eqs. (3.56) and (3.57). Therefore, the location of the minimum in the harmonic spectrum given by Eq. (3.85) is dependent on the electron orbit, i.e., the orthogonal polarisation introduces a dynamical shift. This implies that, whereas in the case of linearly polarised fields there is a clear harmonic at which destructive interference occurs for any given alignment angle, and the interference condition is purely structural, in the case of an orthogonally polarised field, we expect to find minima in various places in the harmonic spectrum depending upon the intermediate momentum components. As the overall spectrum is constructed from the coherent sum of a large number of electron orbits, the above condition is likely to result in blurring and in splitting of the two-centre minima found in the harmonic spectrum.

If the HOMO of the target molecule is composed of s type orbitals only, such as, the HOMO of H_2, which is a $1\sigma_g$ orbital, the interference condition reduces to

$$\Omega=I_p+\frac{(2n+1)^2\pi^2}{2R^2\cos^2(\theta_L-\zeta(t,t'))}. \tag{3.86}$$

If it is composed of only p type orbitals the interference condition reduces to

$$\Omega=I_p+\frac{2n^2\pi^2}{R^2\cos^2(\theta_L-\zeta(t,t'))}. \tag{3.87}$$

3.8 HHG propagation model

In the laboratory the single-atom or molecule harmonic response is not observed. What is observed is the macroscopic harmonic response generated by an intense laser pulse focused into gaseous medium, typically supplied by a gas jet directed perpendicularly across the beam. To model experimental data, we must numerically integrate Maxwell's wave equations with source terms distributed across this extended medium. The simulations are carried out in a comoving, cylindrically symmetric reference frame. After applying the slowly evolving wave approximation (SEWA) $\partial^2 E/\partial z^2 = 0$, Maxwell's equations can be expressed in the time domain as

$$\nabla_\perp^2 E(r,z,t') - \frac{2}{c}\frac{\partial^2}{\partial z \partial t'} E(r,z,t') = -\frac{4\pi}{c^2}\frac{\partial^2}{\partial t'^2} P(r,z,t'), \tag{3.88}$$

or in frequency space as [103]

$$\frac{\partial}{\partial z}\tilde{E}(r,z,\omega) + \frac{ic}{2\omega}\nabla_\perp^2 \tilde{E}(r,z,\omega) = -\frac{2\pi i\omega}{c}\tilde{P}(r,z,\omega), \tag{3.89}$$

where $\tilde{E}(r,z,\omega)$ is the electric field which contains both the driving laser field and the generated harmonic field, and $\tilde{P}(r,z,\omega)$ is the polarisation response of the medium. We assume that the radiation generated by non-linear interactions does not influence the strong driving field, which is a good approximation for the parameter range of interest [103, 101]. This means that we can separate the driving IR laser field $\tilde{E}_\mathrm{l}(r,z,\omega)$ and the generated XUV field $\tilde{E}_\mathrm{h}(r,z,\omega)$, allowing us to solve Eq. (3.89) for each component independently using the appropriate approximations for each case. In this work we consider atomic gas densities between 10^{16} and 10^{17} atoms/cm^3 and interaction lengths of approximately a few mm. These conditions allow us to ignore all linear dispersion and absorption effects for the driving field and consider only the polarisation response $\tilde{P}_\mathrm{ion}(r,z,\omega)$ due to the oscillation of the free electrons created through ionisation of the gas medium. For the laser component, Eq. (3.89) then simplifies to

$$\frac{\partial}{\partial z}\tilde{E}_\mathrm{l}(r,z,\omega) + \frac{ic}{2\omega}\nabla_\perp^2 \tilde{E}_\mathrm{l}(r,z,\omega) = -\frac{2\pi i\omega}{c}\tilde{P}_\mathrm{ion}(r,z,\omega), \tag{3.90}$$

where the second term on the left describes diffraction of the field and the term on the right-hand side describes non-linear polarisation. We then make the approximation that over small distances Δz, the diffraction and polarisation terms may act independently [130]. We can therefore propagate the field from z to $z + \Delta z$ in two steps. In the first step the driving IR field is diffracted in frequency space, thus eq. (3.90) is give by

$$\frac{\partial}{\partial z}\tilde{E}_\mathrm{l}(r,z,\omega) = -\frac{ic}{2\omega}\nabla_\perp^2 \tilde{E}_\mathrm{l}(r,z,\omega). \tag{3.91}$$

This is propagation is performed using the Crank-Nicholson finite-difference method [131]. In the second step we calculate the non-linear polarisation in the time domain via

$$\frac{\partial^2}{\partial t'^2}\tilde{P}_{\rm ion}(r,z,t') = \omega_p^2(r,z,t') + \tilde{E}_{\rm l}(r,z,t') \tag{3.92}$$

where the plasma frequency and the free electron number density are given by

$$\omega_p^2(r,z,t') = \sqrt{4\pi n_e(r,z,t')}, \tag{3.93}$$

and

$$n_e(r,z,t') = n_a(z)(1 - e^{-\int_{-\infty}^{t'}\Gamma(E(r,z,t''))\mathrm{d}t''}), \tag{3.94}$$

respectively. In Eq. (3.94), $\Gamma(E(r,z,t''))$ is the Ammosov-Delone-Krainov (ADK) [132] ionisation rate and $n_a(z)$ is the gas density

$$n_a(z) = N_a e^{-4\ln 2(\frac{z-z_j}{z_\omega})^2}, \tag{3.95}$$

which we have defined using a Gaussian profile. In the above-stated equation, N_a is the peak gas density, z_j marks the z position of the centre of the gas jet, and z_ω is the full width at half maximum (FWHM) width of the jet.

Using Eq. (3.92), the non-linear polarisation step of the propagation is performed by integrating Eq. (3.88) with respect to t' to give

$$\begin{aligned}\frac{\partial}{\partial z}E_{\rm l}(r,z,t') &= -\frac{2\pi}{c}\frac{\partial}{\partial t'}P(r,z,t') \\ &= -\frac{8\pi^2}{c}\int_{-\infty}^{t'} n_e(r,z,t'')E_{\rm l}(r,z,t'')\mathrm{d}t''.\end{aligned} \tag{3.96}$$

This is solved using a second-order Runge-Kutta algorithm [131]. For the propagating XUV component of the field we can ignore the effect of the free electron. This is because these frequencies quickly exceed the plasma frequency [133]. However, we must include the non-linear dipole response of the atomic or molecular gas $\tilde{P}(r,z,\omega)$ and absorption of the XUV field by neutral atoms using XUV absorption coefficients $\alpha_{\rm abs}$ [134]. In the present calculations the linear dispersion due to neutral atoms has not been included. This simplification is justified for H_2, as this molecule exhibits no resonances in the continuum for the frequency range of interest. For the XUV component of the electric field, Eq. (3.89) becomes

$$\frac{\partial}{\partial z}\tilde{E}_{\rm h}(r,z,\omega) + \frac{ic}{2\omega}\nabla_\perp^2\tilde{E}_{\rm h}(r,z,\omega) + n_a(z)\alpha_{\rm abs}(\omega)\tilde{E}_{\rm h}(r,z,\omega) = -\frac{2\pi i\omega}{c}\tilde{P}(r,z,\omega). \tag{3.97}$$

The propagation of the XUV field can be performed in two steps. The first step is equiv-

alent to the first step performed on the driving IR field, i.e. the XUV field is diffracted in frequency space using Eq. (3.90). In the second step the non-linear polarisation step can be performed in the frequency domain. We can also split this step into two pairs, addressing the absorption and dipole terms separately. For the absorption step we get

$$\frac{\partial}{\partial z}\tilde{E}_{\mathrm{h}}(r,z,\omega) = -n_a(z)\alpha_{\mathrm{abs}}(\omega)\tilde{E}_{\mathrm{h}}(r,z,\omega), \tag{3.98}$$

is advanced as

$$\tilde{E}_{\mathrm{h}}(r,z+\Delta z,\omega) = -n_a(z)\alpha_{\mathrm{abs}}(\omega)\tilde{E}_{\mathrm{h}}(r,z,\omega)e^{-n_a(z)\alpha(\omega)\Delta z}. \tag{3.99}$$

For the non-linear dipole response, the contribution is advanced using

$$\frac{\partial}{\partial z}\tilde{E}_{\mathrm{h}}(r,z,\omega) = -\frac{2\pi i\omega}{c}\tilde{P}(r,z,\omega), \tag{3.100}$$

where

$$\tilde{P}(r,z,\omega) = n_a(z)M_{\tilde{\epsilon}}(r,z,\omega), \tag{3.101}$$

and $M_{\tilde{\epsilon}}(r,z,\omega)$ is the frequency spectrum of the dipole acceleration along $\tilde{\epsilon}$. In this thesis this is calculated using the single-atom response model of Sec. 3.1.

So far we have calculated the generated harmonics in the near field, immediately after the interaction region. After exiting the interaction region, both the driving IR field and the XUV field are propagated through the vacuum to model the far field spectrum observed in the lab. This is calculated analytically in the frequency domain via a Huygen's integral, so that our field after a propagation distance of l in the vacuum is given by

$$\tilde{E}_{\mathrm{h}}(r,z+l,\omega) = \frac{i\omega}{cl}\int_{\infty}^{0} r'\tilde{E}_{\mathrm{h}}(r,z,\omega)e^{-\frac{i\omega}{2cl}(r^2+r'^2)}J_0(\frac{rr'\omega}{cl})\mathrm{d}r', \tag{3.102}$$

where J_0 is the zeroth-order Bessel function.

The measured XUV field is the coherent sum of all the harmonics generated from all the atoms in the non-linear medium. Harmonics generated at certain position along the z axis must be in phase with harmonics generated at earlier z position for them to interfere constructively, which is mostly in the forward direction. The two main influences to this phase matching (see Refs. [135] and [136]) is the variation of the intensity and phase of the driving laser across the interaction region, which causes a corresponding variation in the intensity dependent single-atom harmonic response generated throughout the medium. The spatial distribution of the propagated harmonic spectrum is therefore highly dependent on the position of the gas jet relative to the laser focus. Depending on these parameters the newly generated harmonics will constructively or destructively interfere, modulating the coherent accumulation of the macroscopic harmonic field. This

dependence can be utilised to single out certain parts of the propagating XUV field that you want to observe far field. When considering the macroscopic response and propagation of HHG we approximate the field as a sum of parallel and perpendicular components given by

$$E_{\parallel} = E_{\omega} f(t) \cos(n\omega t), \tag{3.103}$$

and

$$E_{\perp} = E_{n\omega} f(t) \cos(2\omega t - 2\phi\pi), \tag{3.104}$$

where, $f(t)$ is the pulse shape given by a Gaussian function.

Chapter 4

Shifted two-centre interference minima

In 2009, a generalised two-centre interference condition for high-order harmonic generation in homonuclear diatomic molecules subjected to a linearly polarised laser field that accounts for the orbital geometry and also $s-p$ mixing was introduced in [57]. Studies of the above-mentioned two-centre interference for elliptically polarised fields, however, are comparatively few. Most of the studies are focused on the harmonic yield, as a function of the driving-field polarisation [62], or on the ellipticity of the high-order harmonics as a way to probe the anisotropy of a molecular medium [63, 64, 65]. In particular, recent investigations have shown that the minimum related to two-centre interference becomes increasingly blurred and appears to split if the ellipticity of the driving field is increased [66]. Therein, an interference condition for the perpendicular molecular orientation was presented, which was different along the major and the minor polarisation axis of the driving field. The focus of such papers, however, was on the vector character of the HHG transition probabilities [66], and on the ellipticity of the high-order harmonics [65]. So far, the above-mentioned blurring and splitting has not been addressed. In this chapter we test our modified two-centre interference condition, (3.85), for aligned diatomic molecules in driving fields of the form given by Eq. (3.58), where the frequency ratio is chosen as $n = 2$. This corresponds to a two-colour field composed of a monochromatic wave of frequency ω along the major polarisation axis and of its second harmonic along the minor axis, respectively.

4.1 Testing the interference condition

As a starting point, we will focus on whether the effective shift $\zeta(t, t')$ can be identified and whether it agrees with Eq. (3.85). For that purpose, we will compute the transi-

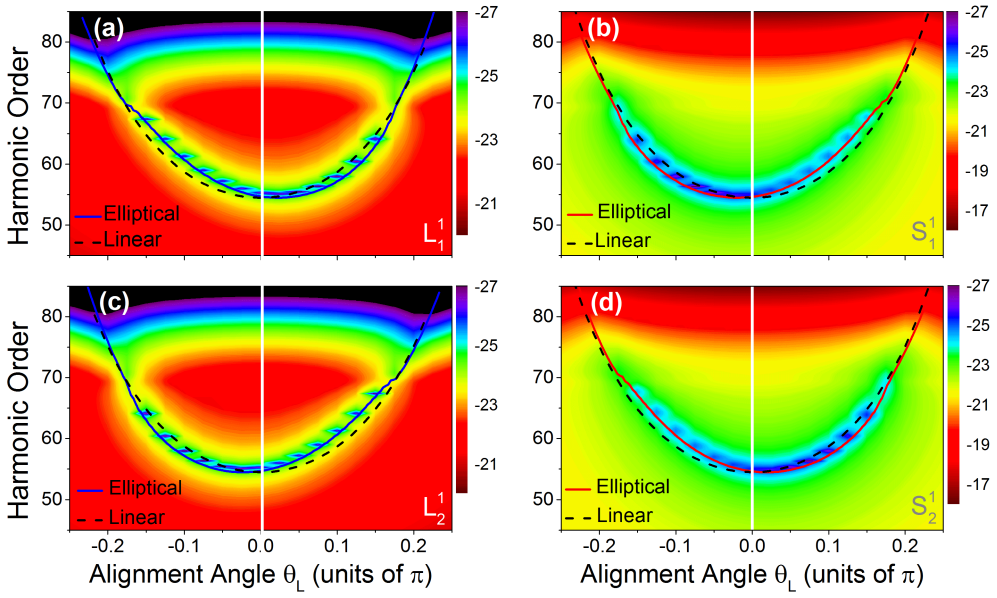

Figure 4.1: Harmonic spectra along the major polarisation axis as functions of the alignment angle θ_L for H_2 (I_p =0.5 a.u. and internuclear separation $R = 1.4$ a.u.) in an OTC field described in Eq. (3.58) with $n = 2$, $\omega = 0.057$ a.u., I=5×10^{14} W/cm^2, $\xi = 0.3$ and time delay $\phi = 0.2$. Panels (a) and (c) show the spectra for the long electron orbits L_1 and L_2 starting in the first and second half cycle, respectively, while panels (b) and (d) exhibit the spectra obtained for the short orbits S_1 and S_2 starting in the first and second half cycle, respectively. The generalised interference condition (3.85) is indicated by the solid lines in the figure, whereby we have just considered the real parts Re$[\zeta(t,t')]$ of the time-dependent shifts. For comparison, we plot the two-centre interference condition for linearly polarised fields as the dashed lines. The central white lines indicate vanishing alignment angle $\theta_L = 0$. The harmonic yield is given in a logarithmic scale. The increase in the harmonic yields after the cut-off observed in the right hand side panels are related to a breakdown of the standard saddle-point approximation for the short orbits (for details see Ref. [3]).

tion probabilities $|M(\omega)|^2$ associated with individual trajectories along which the active electron returns to the core, starting from the dominant, shortest pair of trajectories, which correspond to electron excursion times of the order of three quarters of a field cycle. For simplicity, we will first consider H_2 as a target. Since its HOMO is a $1\sigma_g$ molecular orbital composed of s-type atomic orbitals only, H_2 is very useful for investigating whether Eq. (3.85) holds. The overall field intensity has been taken to be the same as in Ref. [137]. For simplicity the long and short orbits will be labelled L_i^j and S_i^j, respectively, where $i = 1, 2$ indicates whether the trajectory ionised from the first or second half cycle, respectively and j indicates how many half cycles the trajectory spends propagating in the continuum.

In Fig. 4.1, we display the individual contributions of L_1^1 and S_1^1 [panels (a) and (b), respectively] as functions of the alignment angle θ_L between the internuclear axis

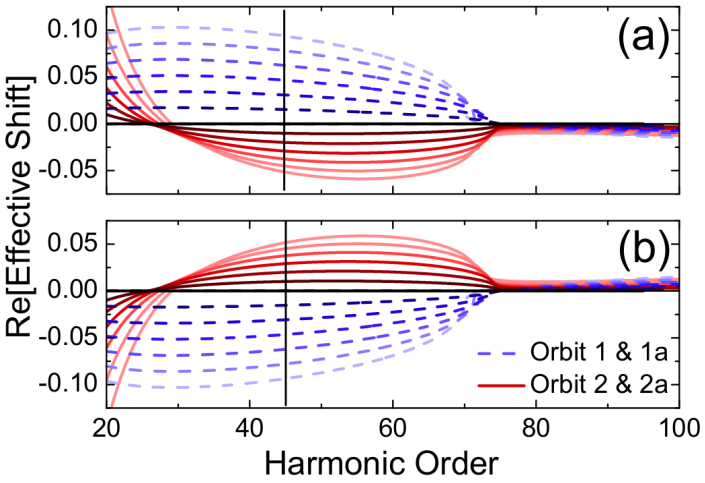

Figure 4.2: Real parts of the effective shifts $\zeta(t,t')$ as functions of the harmonic order computed for orbits L_1 and S_1 [panel (a)] and orbits L_2 and S_2 [panel (b)], using H_2 in a two-colour laser fields of increasing ellipticity and the same relative phase ϕ, intensity and frequency as in Fig. 4.1. The ellipticity has been increased from $\xi = 0$ to $\xi = 0.3$ in increments of $\Delta\xi = 0.05$. A lighter colour indicates a higher ellipticity. For clarity, the harmonic range in which Fig. 4.1 starts is indicated by a black vertical line and a vanishing shift is indicated by a horizontal black line. The dashed lines refer to the orbits L_1 and L_2, while the solid lines correspond to orbits S_1 and S_2.

and the major polarisation axis. These orbits start in the first half cycle of the driving field, slightly after the first field peak, and return close to the field crossing at the end of the first field cycle $t = T = 2\pi/\omega$. In the lower panels of the figure, we display the contributions from the long (L_2^1) and short (S_2^1) orbits from the second half cycle [panels (c) and (d), respectively], whose start and return times are displaced by half a cycle with regard to L_1^1 and S_1^1. Throughout, the two-centre interference conditions are indicated, both for linear and OTC fields (dashed and solid lines, respectively). In the OTC case, we have considered the real parts of the dynamic shift, i.e., $\mathrm{Re}[\zeta(t,t')]$ when plotting the two-centre minimum. We have verified that this approximation is accurate enough for individual orbits, as $\mathrm{Im}[\zeta(t,t')]$ is vanishingly small in the harmonic ranges of interest.

As an overall feature, we observe an excellent agreement between Eq. (3.85) and the outcome of the SFA computations, with the two-centre minimum varying from orbit to orbit. Moreover, in contrast to what happens for linearly polarised fields, the minimum is no longer symmetric upon $\theta_L \to -\theta_L$. These features can be explained in terms of the time dependence of the effective shift $\zeta(t,t')$. For a specific orbit, the times t and t' will only vary with the harmonic energy Ω. Hence, shifting θ_L to $-\theta_L$ does not imply shifting $\zeta(t,t')$ to $-\zeta(t,t')$, and the above-mentioned symmetry will be broken. Furthermore, because t and t' are orbit dependent, we observe different shifts $\zeta(t,t')$ for different orbits. In fact, for orbits L_1^1 and S_2^1, the shifts displace the interference minimum

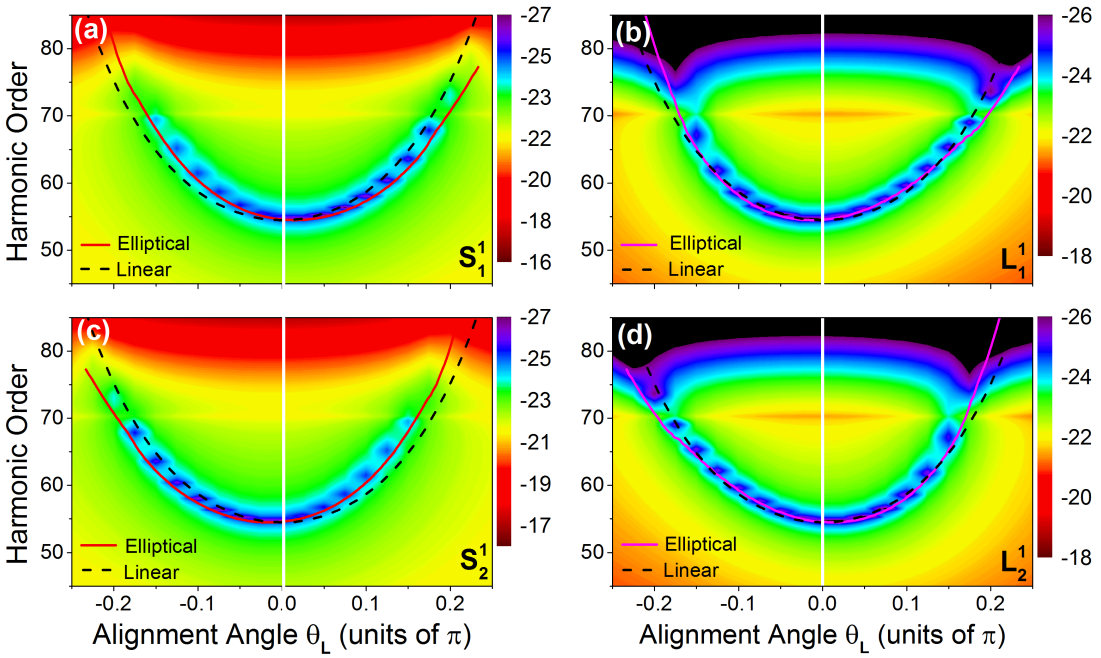

Figure 4.3: Transition probabilities associated with individual orbits for H_2 in an OTC field with the same parameters as in Fig. 4.1, but time delay $\phi = 0$ between the ω and the 2ω waves. Panels (a) and (c) correspond to the long orbits L_1 and L_2, while panels (b) and (d) give the contributions of the short orbits S_1 and S_2. The interference minima for the linear and OTC polarised fields are indicated by the dashed and solid lines, respectively, in the figure. The increase in the harmonic signal after the cut-off observed in the left panels is related to a breakdown of the standard saddle-point approximation for the long orbits (for details see Ref. [3]). The harmonic yields are displayed in a logarithmic scale.

to the right, while for orbits L_2^1 and S_1^1, this displacement is to the left. Interestingly, the shifts observed for orbits L_1^1 and S_1^1 are the mirror image of those obtained for orbits L_2^1 and S_2^1, respectively. This is due to the specific behaviour of the two-colour driving field for $t \to t \pm T/2$, where $T/2 = \pi/\omega$. In this case, $A_\parallel(t \pm T/2) = -A_\parallel(t)$, and $A_\perp(t \pm T/2) = A_\perp(t)$. Hence, direct inspection of Eq. (3.84) shows that $\zeta(t, t') = -\zeta(t \pm T/2, t' \pm T/2)$. For a monochromatic elliptically polarised field, i.e., $n = 1$ in Eq. (3.58), $\zeta(t, t') = \zeta(t \pm T/2, t' \pm T/2)$, i.e., the shift will remain invariant if the ionisation and return times are displaced in half a cycle. This will be investigated in more detail in Chapter 6

The above-stated observation is confirmed by Fig. 4.2, in which the real parts of the effective shifts $\zeta(t, t')$ are plotted for driving fields of increasing ellipticity. The case considered in the previous figure, i.e., $\xi = 0.3$, is given by the outer curves. For the harmonic range considered in Fig. 4.1, i.e., $45 \leq \Omega/\omega \leq 90$, $\mathrm{Re}[\zeta(t, t')] > 0$ for orbits L_1 and S_2. This is consistent with the fact that the interference minimum shifts to the right for both orbits [see Figs. 4.1(a) and (d)]. Indeed, when subtracted from a positive

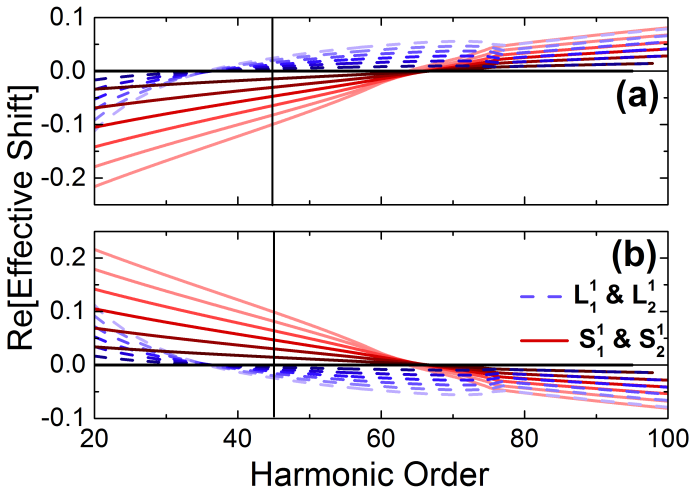

Figure 4.4: Real parts of the shifts $\zeta(t,t')$ computed for an OTC field (3.58) where $n = 2$ and $\phi = 0$. Panels (a) and (b) refer to the orbits released in the first and second half cycle, respectively. The remaining molecular and field parameters are the same as in Fig. 4.2.

alignment angle θ_L, a positive shift will displace the interference condition (3.85) towards lower harmonics. For $\theta_L < 0$, on the other hand, subtracting a positive shift will bring the minimum towards higher energies. Beyond the cut-off, the real parts of the shifts decrease substantially. Consequently, the interference condition will approach that obtained for a linearly polarised field. This is clearly seen in Fig. 4.1, for harmonic order $\Omega/\omega \geq 69$. A similar analysis can be performed for orbits S_1 and L_2, for which the U-shaped minimum is displaced to the left in Fig. 4.1(b) and (c). In this latter case, $\mathrm{Re}[\zeta(t,t')] < 0$ in the harmonic range of interest. Note, however, that there is a small residual shift beyond the cut-off, whose real part is negative for the orbits starting at the first half cycle, and positive for those starting at the second half cycle [Figs. 4.2(a) and (b), respectively]. Hence, the minimum for orthogonal polarisation will approach its counterpart for linearly polarised fields from the right in Figs. 4.1(a) and (b), and from the left in Figs. 4.1(b) and (d).

One should note, however, that these shifts are strongly dependent on the time delay between the low-frequency and high-frequency waves. An example is provided in Fig. 4.3, for which both driving waves are in phase, i.e., $\phi = 0$. The minima for the dominant orbits L_1, L_2, S_1 and S_2 once more follow the generalised interference condition (3.85). The curves, however, are markedly different from those displayed in Fig. 4.1. A noteworthy feature is that there are now large residual shifts beyond the cut-off. This is explicitly shown in Fig. 4.3. There is once more a very good agreement between Eq. (3.85) and the minima encountered, but there are large residual shifts at and beyond the cut-off.

This agrees with Fig. 4.4, in which the real parts of the shifts are displayed for the

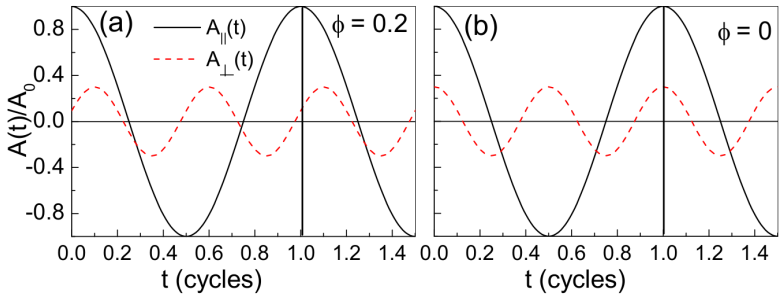

Figure 4.5: Schematic representation of the major and minor components of the vector potential $A(t)$ for ellipticity $\xi = 0.3$, frequency ratios $1:2$ [$n = 2$ in Eq. (3.58)], and relative phases $\phi = 0.2$ and $\phi = 0$ [panels (a) and (b), respectively]. The electron return time at $t = 2\pi/\omega$ is indicated by the thick black lines in the figure. For simplicity, all fields have been normalised to the vector potential amplitude $A_0 = E_0/\omega$.

dominant orbits and $\phi = 0$. In contrast to what has been observed in Fig. 4.2, $\mathrm{Re}[\zeta(t,t')]$ has a non-vanishing value at the cut-off. For instance, for orbits L_1 and S_1, the residual shift at the cut-off is positive. However, if the electron returns half a cycle later, i.e., along orbit L_2 or S_2, this shift is negative. This is expected as the major component $A_\parallel(t)$ and $A_\parallel(t \pm T/2)$ have different signs.

The behaviour with the time delay ϕ may be understood if one takes into consideration that this phase difference has a strong influence on the velocity $p_\perp + A_\perp(t)$ of the electron upon return along the minor polarisation axis. We have verified that, for a wide range of phases ϕ, including $\phi = 0$ and $\phi = 0.2$, the electron return times are practically identical to those obtained for linearly polarised fields. Thus, at the cut-off, the electron will return near a crossing of the electric field $E_\parallel(t)$ along the major polarisation axis. If $\phi = 0.2$, the amplitude $|E_\perp(t)|$ will be close to its maximum. This implies that $|A_\perp(t)|/A_0 \ll 1$. Hence, $\mathrm{Re}[\zeta(t,t')]$ is very small for the harmonics at and beyond the cut-off. On the other hand, if $\phi = 0$, the perpendicular component $A_\perp(t)/A_0 = \pm 1$ for the cut-off return times. This implies that the residual shifts will be large.

This can be seen in Fig. 4.5, where we provide an illustration of the vector potentials $A_\parallel(t_c)$ and $A_\perp(t_c)$ for the return times at a crossing. For $\phi = 0.2$ [Fig. 4.5(a)], the vector potential $A_\perp(t_c)$ is very small, and so is the shift at and beyond the cut-off. There is, however, a residual shift as the vector potential is not exactly zero. For $\phi = 0$, the transverse vector potential $A_\perp(t_c) = \xi E_0/(2\omega)$ is at its maximum at $t = t_c$, as shown in Fig. 4.5(b), so that the transverse velocity of the electron upon return will be non-vanishing. Hence, at and beyond the cut-off $\mathrm{Re}[\zeta(t,t')] \neq 0$. This will leave large residual shifts beyond the cut-off, as shown in the previous figures.

In order to see the behaviour outlined in Fig. 4.2 more clearly, it is desirable to seek a parameter range for which several minima are present over a wide harmonic energy range.

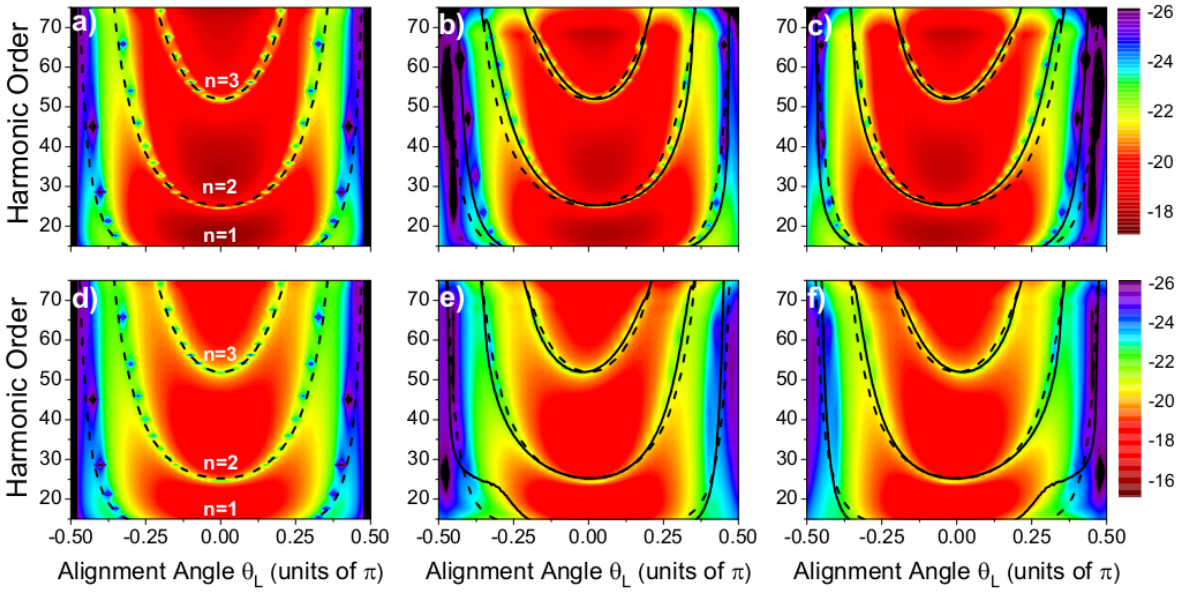

Figure 4.6: Harmonic spectra along the major polarisation axis computed for individual orbits as functions of the alignment angle θ_L for Ar_2 (ionisation potential $I_p = 0.58$ a.u. and internuclear separation $R = 7.2$ a.u.). For comparison, the individual-orbit contributions obtained for linear polarisation are displayed in the far left panels (a) and (d), while in the middle and far right panels (b), (c), (e) and (f) the same $\omega - 2\omega$ OTC field as in Fig. 4.1 has been employed. Panels (b) and (c) exhibit the contributions from the long orbits L_1^1 and L_2^1, respectively, while panels (e) and (f) depict the contributions from the short orbits S_1^1 and S_2^1, respectively. The interference conditions for OTC and linearly polarised fields are indicated as the solid and dashed lines in the figure, respectively. The harmonic yield is given in a logarithmic scale. The increase in the harmonic yields after the cut-off observed in panels (e) and (f) are related to a breakdown of the standard saddle-point approximation for the short orbits (for details see Ref. [3]).

This can be achieved by choosing a target with a large equilibrium internuclear distance, such as Ar_2. The spectra computed for this target using individual orbits is displayed in Fig. 4.6, for the same driving field as in Figs. 4.1 and 4.2. For each panel, one may identify three interference minima. The lowest-order minimum spans the whole harmonic range displayed in Fig. 4.2, the intermediate minimum starts at approximately $\Omega = 30\omega$, and the highest minimum covers similar harmonic frequencies to those studied in Fig. 4.1. The figure shows very distinct behaviours for the long and short orbits. For the long orbits there is a monotonic shift, either to the right [Fig. 4.6(b)], or to the left [Fig. 4.6(c)], while for the short orbits the sign of $\mathrm{Re}[\zeta(t,t')]$ varies. As a direct consequence, the elliptical minima "wiggle" around their linear counterparts. For example, for orbit S_1^1 [Fig. 4.6(e)], there is a shift to the right for harmonic frequencies $\Omega \lesssim 30\omega$ in the two lower minima. Around this harmonic energy, the minimum crosses that obtained for linear polarisation, and moves to the left. This is consistent with the behaviour of the red solid curves in Fig. 4.2(a). For orbit S_2^1, the minimum follows the red curves in

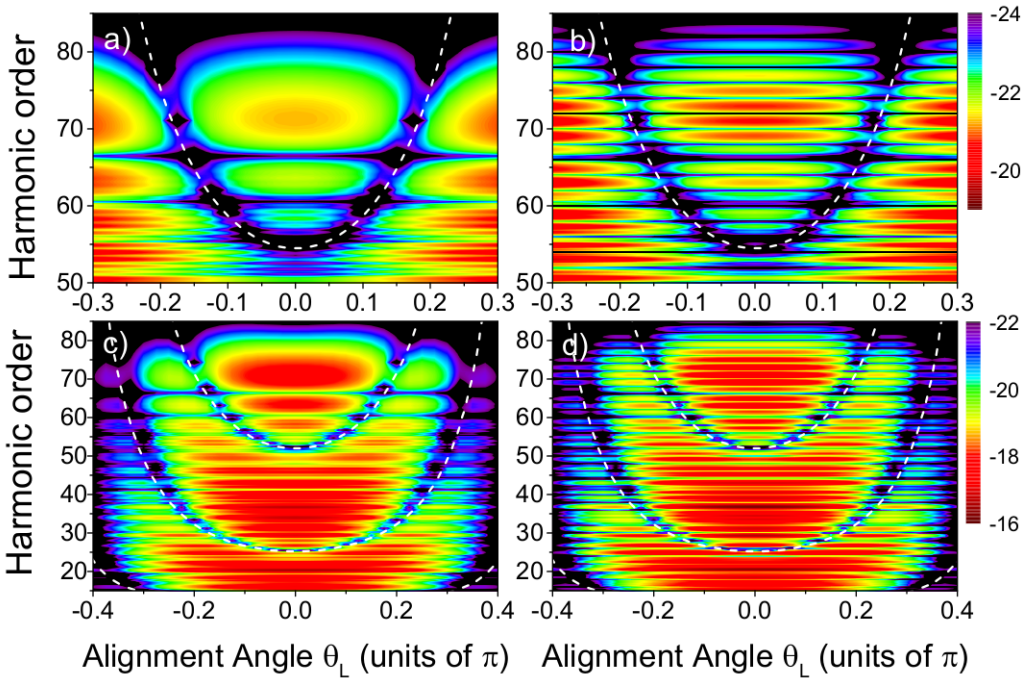

Figure 4.7: Spectra computed for H_2 [panels (a) and (b)] and Ar_2 [panels (c) and (d)] in a linearly polarised field ($\xi = 0$), including the six shortest pairs of orbits starting in the first [panels (a) and (c)] and in both half cycles [panels (b) and (d)]. The field intensity and frequency have been chosen as $I = 5 \times 10^{14}$ W/cm^2 and $\omega = 0.057$ a.u., respectively. The internuclear distances are $R^{(H_2)} = 1.4$ a.u and $R^{(Ar_2)} = 7.2$ a.u. The white dashed lines indicate the energy positions of the two-centre interference minima. The yield is displayed in a logarithmic scale.

Fig. 4.2(b), i.e., they are the mirror image of those in Fig. 4.6(e) with regard to the shift $\theta_L \to -\theta_L$. This is explicitly shown in Fig. 4.6(f). Once more, beyond the cut-off the elliptical and the linear minima approach each other for $\phi = 0.2$. In general, the outcome of the strong-field approximation follows the minima predicted by Eq. (3.85) reasonably well. An exception is, however, the interference minimum $n = 1$ obtained for the short orbits in very low ($\Omega < 20\omega$) and very high (i.e., beyond the cut-off) harmonic ranges [see Figs. 4.6(e) and (f)]. These discrepancies are possibly due to the fact that, in these regions,the imaginary parts $\mathrm{Im}[\zeta(t, t')]$ increase considerably for orbits S_1^1 and S_2^1. Thus, the approximation employed in the figure ceases to be accurate. Nevertheless, we have verified that the analytic condition (3.85) is also valid in this energy region for $\xi \leq 0.2$ (not shown).

4.2 Coherent superposition of orbits

In this section, we will study how the dynamic shifts discussed above will add up if a coherent superposition of orbits is taken into account. This is important as, in a

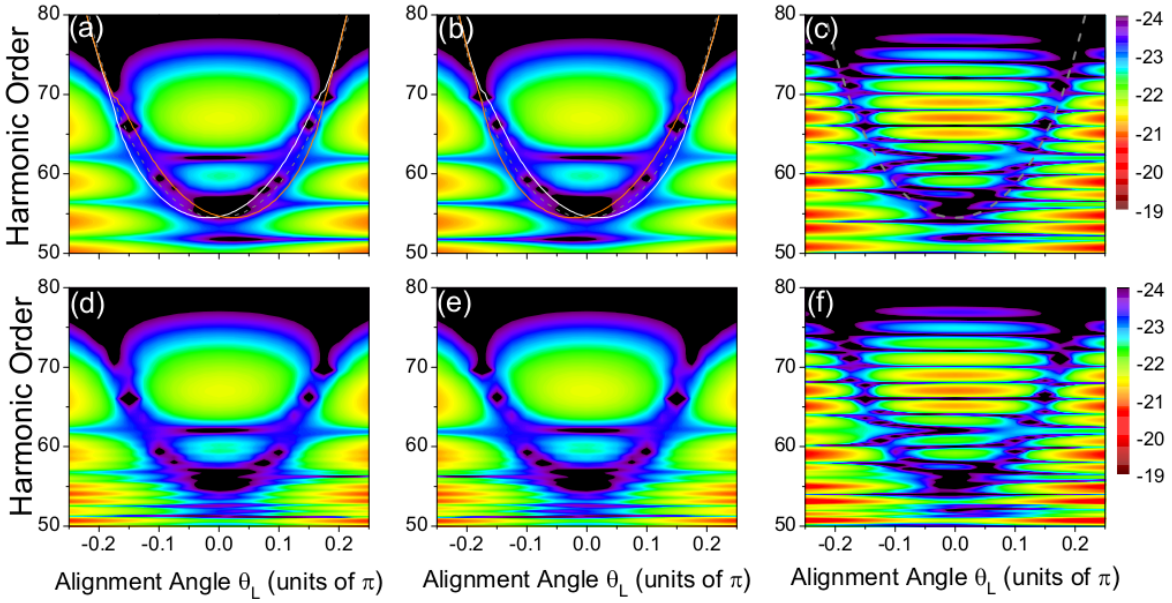

Figure 4.8: Spectra computed for the same field and molecular parameters in Fig. 4.1 ($\phi = 0.2$), but considering the coherent sums of the transition amplitudes associated to: Orbits L_1^1 and S_1^1 [panel (a)]; orbits L_2^1 and S_2^1 [panel (b)]; orbits L_1^1, S_1^1, L_2^1 and S_2^1 [panel (c)]; the three shortest pairs of orbits starting at the first half cycle; i.e., the pairs composed of orbits (L_1^1, S_1^1), (L_1^2, S_1^2) and (L_1^3, S_1^3) [panel (d)]; the three shortest pairs of orbits ($L_2^{1,2,3}$ and $S_2^{1,2,3}$) starting at the second half cycle [panel (e)]; the three shortest pairs of orbits from both half cycles, i.e., orbits ($L_{1,2}^{1,2,3}$ and $S_{1,2}^{1,2,3}$) [panel (f)]. The modified interference conditions for the long and short orbits are given by the solid orange and white curves in panels (a) and (b), while the condition for linearly polarised fields is indicated by the dashed grey lines in panels (a), (b) and (c). The yield is displayed in a logarithmic scale.

high-harmonic spectrum, there will be several possibilities for the electron to return. Quantum mechanically, the corresponding transition amplitudes will interfere, so that not only the real parts of such shifts, but also their imaginary parts, become important. For comparison, we include the spectra computed for molecules in linearly polarised fields using the three shortest pairs of orbits. These spectra are displayed in Fig. 4.7, for H_2 and Ar_2 (upper and lower panels, respectively). The figure also shows other types of interference, that arise from the coherent superposition of ionisation and recombination events displaced in time. In all panels, we notice that both the temporal interference patterns and the spatial, two-centre interference minima are symmetric upon $\theta_L \to -\theta_L$. This is expected from our previous line of argument, and holds if orbits starting in the first half cycle [Figs. 4.7(a) and (c)], or in both half cycles [Figs. 4.7(b) and (d)] are included. Another noteworthy feature is the presence of well defined odd harmonics when the orbits starting at subsequent half cycles are added coherently, which can be clearly observed in Figs. 4.7(b) and (d). They are a consequence of the periodicity of the

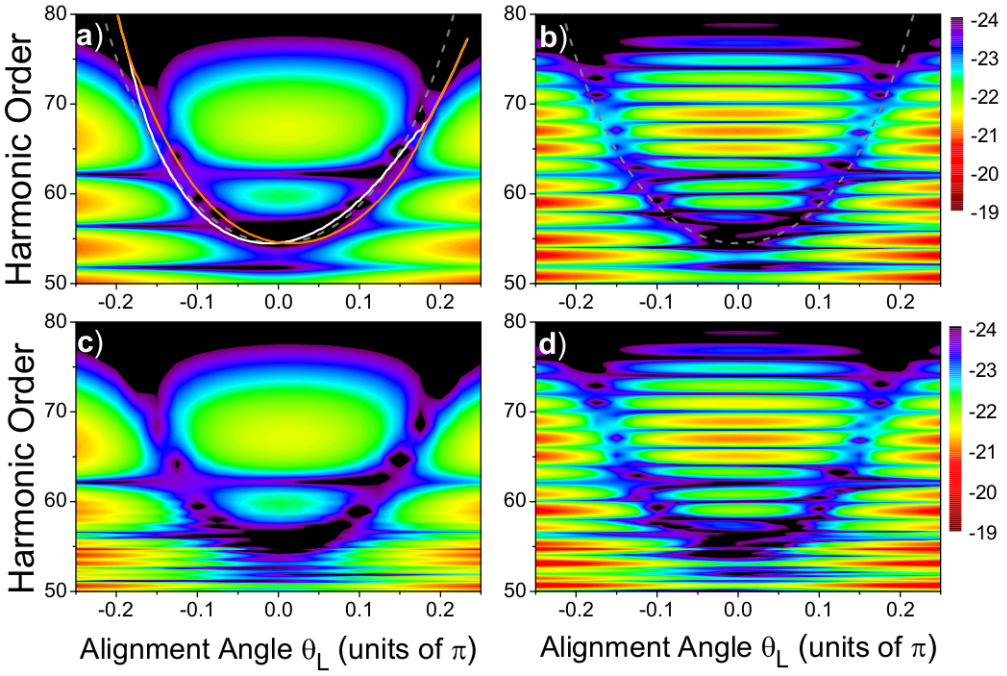

Figure 4.9: Spectra computed for the same field and molecular parameters in Fig. 4.3 ($\phi = 0$), but considering the coherent sums of the transition amplitudes associated to different combinations of orbits. Panels (a) and (b) include the dominant pair starting at the first half cycle and at both half cycles, respectively, while panels (c) and (d) include the contributions from orbits ($L_1^{1,2,3}$ and $S_1^{1,2,3}$) and ($L_{1,2}^{1,2,3}$ and $S_{1,2}^{1,2,3}$), respectively. The interference condition for linear polarisation is indicated by the dashed lines in the upper panels, while its counterpart for OTC fields is given by the solid lines in panel (a). The orange and white lines refer to modified interference condition for orbits L_1^1 and S_1^1, respectively. The yield is displayed in a logarithmic scale.

field, and are not present if the start times are restricted to the first half cycle. In Fig. 4.8, we consider several coherent superpositions of orbits for elliptically polarised fields. We will first focus on the dominant pairs of orbits, i.e., L_1^1 and S_1^1, and, L_2^1 and S_2^1, for H_2 and $\phi = 0.2$. These contributions are displayed in Figs. 4.8(a) and (b), together with the coherent superposition of the two dominant pairs [Fig. 4.8(c)]. These results are then compared to the spectra displayed in the lower panels of the figure, obtained using the three shortest pairs. Specifically, in panel (d) of Fig. 4.8, we take orbits (L_1^1, S_1^1), (L_1^2, S_1^2) and (L_1^3, S_1^3) which all ionise in the first half cycle but spend different amounts of time propagating in the continuum before recombining. For panels (e) and (f) we consider the orbits (L_2^1, S_2^1), (L_2^2, S_2^2) and (L_2^3, S_2^3) starting in the second half cycle, and then all six pairs of orbits, respectively.

All panels exhibit the U-shaped interference minimum, whose approximate position is roughly indicated by the interference conditions for linear and OTC polarisation (see the three curves in the figure). The outcomes of our simulations, however, do not follow

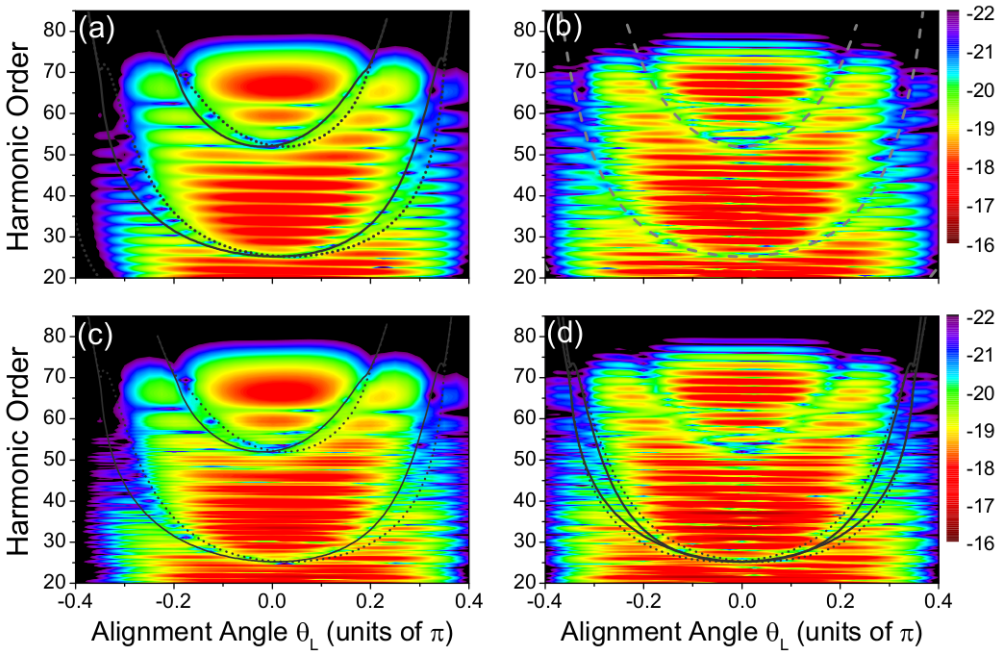

Figure 4.10: Spectra computed for Ar_2 using the an OTC field of Fig. 4.1 ($\xi = 0.3$, $\phi = 0.2$) and using different coherent superpositions of orbits. In panels (a) and (b), we included only the dominant orbits, while in panels (c) and (d) the six shortest pairs of orbits have been taken. In panels (a) and (c), we considered only ionisation events starting in the first half cycle, while in panels (b) and (d) both first and second half cycles have been taken into consideration. The dotted and solid black lines in panels (a), (c) and (d) give the interference conditions for the long and short orbits, respectively. The dashed grey lines in panel (b) give the interference condition for linear polarisation. In the figure, only the interference minima corresponding to $n = 2$ and $n = 3$ in Eq. (3.85) are visible. The yield is displayed in a logarithmic scale.

a single interference curve. This is expected as the contributions from each orbit in a pair carry comparable weights, so that temporal interference effects between the long and short orbits play a role. The interference minima appear most clearly in the cut-off region, at roughly $\Omega = 71\omega$, and at the bottom of the U-shaped minimum, near $\Omega = 55\omega$. This is due to the fact that, in these energy regions, the interference conditions are closest. At the lower-energy end of the U-shaped minimum, the three interference curves cross. Hence, the two-centre minimum is very visible. In the vicinity of this point, however, the three curves are very distinct. This implies that a blurring in the interference condition for a coherent superposition is expected in this region. At the cut-off, both $\mathrm{Re}[\zeta(t, t')]$ and $\mathrm{Im}[\zeta(t, t')]$ are closest and approach the interference condition for linear polarisation. As a direct consequence, the two-centre minimum is sharp around this frequency. Beyond the cut-off, the imaginary parts of the shifts start to increase in absolute value and move away from each other. This will have little influence if only individual orbits are taken, as shown in the previous section, but will be critical for a coherent superposition of orbits.

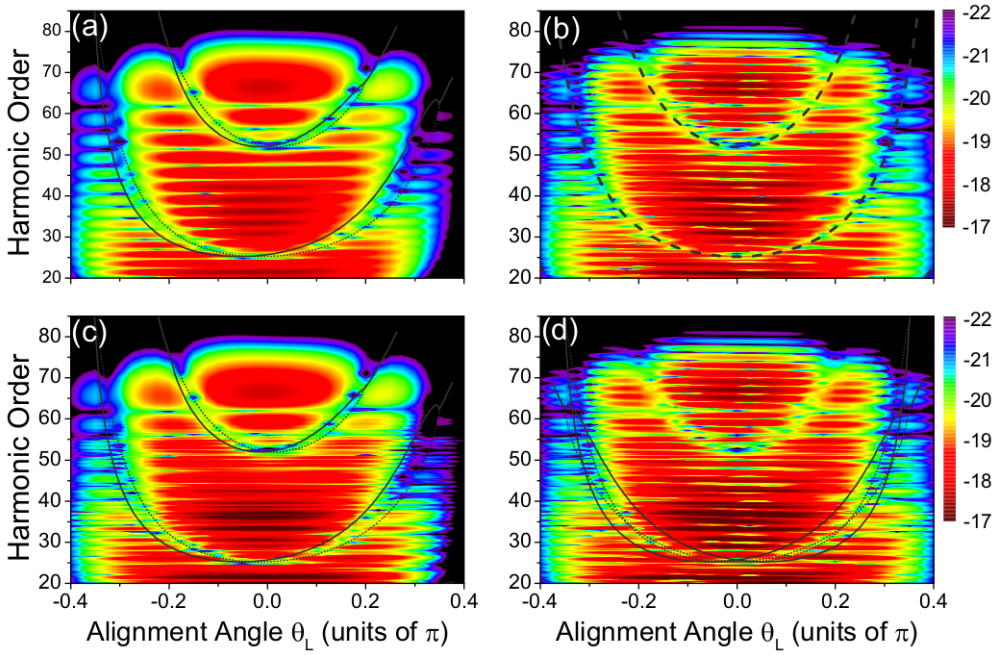

Figure 4.11: Spectra computed for Ar_2 using the same parameters and coherent superpositions of orbits as in Fig. 4.10, but with a time delay of $\phi = 0$. Panels (a) and (b) show the dominant orbits from the first half cycle (L_1^1 and S_1^1) and both the first and second half cycle ($L_{1,2}^1$ and $S_{1,2}^1$), respectively. Panels (c) and (d) show the contributions from the six shortest pairs of orbits from the first half cycle ($L_1^{1,2,3}$ and $S_1^{1,2,3}$) and the first and second half cycle ($L_{1,2}^{1,2,3}$ and $S_{1,2}^{1,2,3}$), respectively. The dashed lines in panel (b) give the interference condition for linear polarisation, and lines in the remaining panels give the interference condition (3.85). The dotted and the solid lines refer to the long and short orbits, respectively. The yield is displayed in a logarithmic scale.

For that reason, the minimum becomes blurred in this region. As in the linear case, there are high-order harmonics if orbits starting at different half cycles are included. The interference patterns, however, are no longer symmetric with regard to $\theta_L \to -\theta_L$, not even if the orbits starting in both cycles are taken into account [see Figs. 4.8 (c) and (f)]. As expected, the spectra obtained for orbits starting at the second half cycle of the field, displayed in Figs. 4.8 (b) and (e), are the mirror images of those computed using the orbits starting at the first half cycle, shown in Figs. 4.8 (a) and (d). This holds not only for the U-shaped minimum, but also for the patterns associated with the interference of events displaced in time.

If the longer orbits are included, this leads at most to additional substructure in the low-plateau region, as a direct comparison of the lower and the upper panels of Fig. 4.8 shows. This is caused by two main reasons. First, the excursion times of the electron in the continuum are much longer, in fact over one and a half cycles. Hence, a larger degree of wavepacket spreading occurs for the active electron, and this renders the contributions of such orbits less relevant. Second, the cut-off determined by such pairs is lower than

that determined by the dominant orbits [see Fig 3.2]. In fact, for the parameters employed in the figure, it lies around $I_p + 1.48U_p$ for orbits $(L^2_{1,2}, S^2_{1,2})$, and around $I_p + 2.42U_p$ for orbits $(L^3_{1,2}, S^3_{1,2})$. This implies that, beyond harmonic frequencies $\Omega \simeq 55\omega$, the contributions from such orbits are strongly suppressed. Finally, we observe an overall decrease in intensity, in comparison to the linearly polarised case. This is expected, as a non-vanishing ellipticity leads to a decrease in the tunnel ionisation rate [138] and also in the return probability for the electron [139]. There is also a displacement of the cut-off frequency towards lower energies, in agreement with previous studies in the literature [140, 141, 142].

In Fig. 4.9, we display the results obtained considering different coherent superpositions if both waves are in phase, i.e., for $\phi = 0$. Also in this case, the main effect is a blurring of the structural interference condition, except at the lowest-energy part of the interference minimum and near the cut-off. An interesting aspect is how the residual shifts that exist beyond the cut-off behave. If one considers start times in a specific sub-cycle, these shifts are apparent in the U-shaped structure. For instance, in Figs. 4.9(a) and (c), in which only orbits starting at the first half cycle have been included, one clearly sees that the suppression observed in the harmonic spectrum matches the solid lines in the cut-off region much more accurately than the interference condition for linear polarisation (dashed grey line). Apart from that, this suppression is asymmetric and much more pronounced for $\theta_L > 0$, i.e., on the right-hand side of these panels. This is in agreement with the previous discussions. If, however, the contributions from the first and second sub-cycles are added coherently, both this asymmetry and the residual shifts are washed out [see Figs. 4.9(b) and (d)]. As expected from our previous discussion, (i) odd harmonics appear due to the periodicity of the field, as shown in the right panels, and (ii) the longer orbits do not influence the spectra considerably, as shown in the lower panels. An interesting effect is a blurring in the two-centre minimum near the cut-off frequency (see harmonics $\Omega = 65\omega$ to $\Omega = 69\omega$) identified in Figs. 4.9(b) and (d). This blurring is caused by the non-vanishing residual shifts from orbits located at different half cycles. These shifts are different for the orbits starting in the first and second half cycles, and smear the minimum if a coherent superposition is taken. For comparison, see Figs. 4.8(c) and (f), computed for $\phi = 0.2$. As in this latter case the residual shift is vanishingly small near the cut-off, this blurring is absent. In Fig. 4.10 we exhibit the results computed for Ar_2 in an elliptically polarised field with $\phi = 0.2$. We focus on the two-centre minima $n = 2$ and $n = 3$ in Eq. (3.85). Apart from the above mentioned inaccuracies close to the threshold, inclusion of the minimum $n = 1$ would require a much larger range of intensities and would obscure the effects we intend to analyse. The minimum $n = 3$, located in the high-plateau region, behaves in a very similar way as that encountered for H_2, i.e., there is an overall blurring with regard to the linearly polarised case and the

minimum is clearest near the cut-off and at the bottom of the U-shaped minimum. The minimum $n = 2$ spans a much larger harmonic region, so that the features observed are more dramatic. For this minimum, we no longer observe a structure as in Fig. 4.7, but a whole region in which suppression of the harmonic signal occurs, i.e., there is a splitting in the minimum. This region is bounded by the different interference conditions obtained for the long and short orbits, indicated by the solid and dotted lines in Figs. 4.10(a) and (c). This can be seen most clearly in Fig. 4.10(a), in which only the dominant orbits starting in the first half cycle have been included. This picture, however, persists if the longer pairs of orbits are included, as shown in Fig. 4.10(c). If the orbits starting in the second half cycle are also added coherently, this region will be bounded by the largest shifts $\mathrm{Re}[\zeta(t, t')]$, which, in this case, correspond to the long orbits L_1^1 and L_2^1 [dotted lines in Fig. 4.10(d)].

Similar results, shown in Fig. 4.11, have been encountered for $\phi = 0$. However, because of the residual shifts that exist for this phase, the splitting in the interference condition for the minimum $n = 2$ is far more visible. This is specially true if the start times are restricted to a single half cycle, as shown in Fig. 4.11(a) and (c). In this latter case, there is also much larger asymmetry in the yield near the cut-off region for $n = 2$. This is very visible if one compares the harmonic yield observed in the region $60 < \Omega/\omega < 70$ and alignment angle $\theta_L \simeq \pi/3$ with its counterpart for $\theta_L \simeq -\pi/3$. For the former angle, this yield is much more suppressed in this harmonic range. If however, one includes starting times in both half cycles [see Figs. 4.11(b) and (d)], this asymmetry is lost.

4.3 Conclusions and questions

In this chapter, we have studied high-order harmonic generation in diatomic molecules in OTC laser fields. We have shown that, even within a very simple model, namely the strong-field approximation and the single active electron, single active orbital approximation, a non-vanishing driving field ellipticity introduces a dynamic shift in a two-centre interference condition which, for linear polarisation, is purely structural. This shift depends very strongly on the orbit along which the active electron returns to its parent molecule, and on its kinetic energy upon return. What happens is that the angle with which the electron returns is effectively incorporated in the two centre interference condition. Furthermore, depending on whether the electron returned with a non-vanishing transverse velocity at a field crossing, there may be a residual dynamic shift at and beyond the cut-off region for a given pair of orbits. A concrete example has been provided for the situation in which both low- and high-frequency driving waves were in phase.

For HHG transition probabilities related to individual orbits, we have found that,

in general, our numerical results match very nicely the predictions from our generalised interference condition. If coherent superpositions of orbits are taken into account, the different shifts cause a blurring, and, in some cases, a splitting in the two-centre minima. For non-vanishing ellipticity, these minima are no longer sharp, but, rather, there will be a region in the spectra for which the harmonic signal is suppressed. This region is bounded by the different interference conditions encountered for individual orbits. A similar splitting is also visible, though not discussed, in Ref. [66].

Can the shift be measured in an experimental setting?

The above-stated results show that, in principle, the angle with which the electron returns to its parent molecule can be extracted from the shifts in the two-centre interference patterns. In Ref. [24], this angle has been inferred from the ratio between even and odd harmonics. One should note, however, that, because the shifts are orbit dependent, they will be difficult to extract from the interference patterns unless a particular return event can be singled out. This would avoid the blurring and splitting related to coherent superpositions of orbits.

Both the blurring and the splitting happen in most harmonic ranges, except in the cut-off region or when the modified interference conditions coincide. Hence, in a realistic situation, these dynamical shifts would mainly blur the two-centre minima unless they converged to a single residual shift at the cut-off, or one of the orbits in a dominant pair could be suppressed. If the ionisation events are restricted to a single half cycle of the driving field, clear shifts may be observed under two conditions. First, if the relative phase ϕ is chosen such that the residual shift at the cut-off is large, it may be identified for harmonics in that energy range. Second, if such a phase choice is not possible, then one of the orbits in the dominant pair must be suppressed by adequate macroscopic propagation conditions [104]. Indeed, it is a well-known fact that the long and the short orbits phase match differently [135]. This allows a high degree of control on which orbit is dominant in which spatial region [44, 106].

In addition to that, however, if the contributions to the spectra from other half cycles are comparable, blurring may still occur, as discussed in Sec. 4.2. Hence, it is necessary to suppress such events by an adequate field choice, such as for instance, few cycle pulses [143]. Finally, one should note that, in this work, we have used the single-active electron, single-active orbital approximation. However, it may happen that multielectron effects and the core dynamics modify the structural interference condition obtained using the highest occupied molecular orbital (HOMO). Hence, for the interference condition computed in this work to be valid, it is necessary that the core can still be assumed to be static and that the contributions from the HOMO are dominant.

Chapter 5

Macroscopic HHG spectra-extracting an electron's angle of return

In the previous chapter we showed that an electron's angle of return is effectively incorporated in to the shifted two-centre interference minima within the HHG spectrum. A legitimate question is, however, whether this shift can be observed under more realistic conditions, such as experiments.

In Chapter 4 we anticipated a series of difficulties that may arise. First, even at the single-molecule response level, there are coherent superpositions of orbits, which will be detrimental for the identification of individual shifts. Second, the core dynamics may mask these shifts further and has not been incorporated in this model [56, 63]. Third, these shifts depend on the driving-field intensity, which will vary across the beam profile. Fourth, there is no evidence that these shifts survive effects that occur during HHG propagation in a macroscopic medium.

On the other hand, propagation may facilitate the observation of these shifts, since the long and the short orbits in the dominant pair phase match differently [104, 105]. Thus, by carefully choosing the propagation conditions one may be able to select the contributions, and the shifts, associated with individual orbits. This type of selection has been successfully used in the past to optimize attosecond-pulse production (for a seminal paper and a comprehensive review on this topic see, e.g. [104], and [101]). In fact, it has even been shown that to obtain clear enough interference patterns between both orbits requires a very delicate tuning of the propagation conditions [44, 106]. Further trajectory selection may be achieved by creating temporal or spatial gates, by playing around with the pulse shape, polarization and/or macroscopic conditions. Examples of different trajectory-selection mechanisms are provided in the reviews [101, 136]. In this

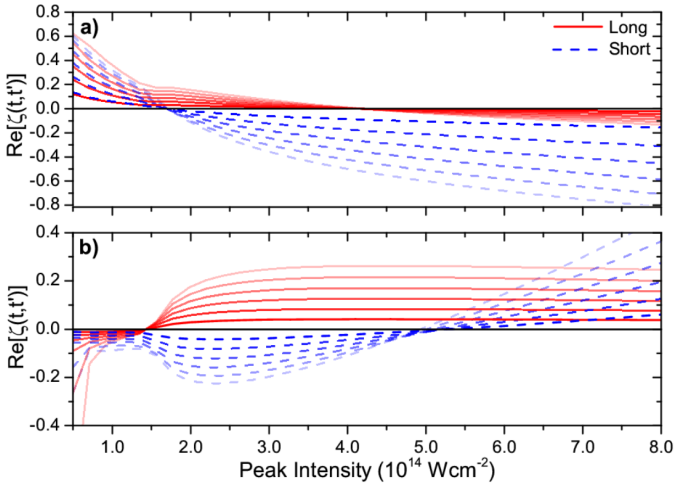

Figure 5.1: Real parts of the effective shifts $\zeta(t, t')$ as functions of the driving-field intensity I_ω of the fundamental for a harmonic of frequency $\Omega = 31\omega$, using H_2 (I_p= 0.59 a.u.) in two-colour laser fields of increasing ellipticity. The fundamental and the second harmonic have been approximated by monochromatic waves where $I_{2\omega} = \xi I_\omega$. The ellipticity has been increased from $\xi = 0$ to $\xi = 0.3$ in increments of $\Delta\xi = 0.05$. A lighter colour indicates a higher ellipticity. The dashed and solid lines refer to the short and long orbits, respectively. Panel (a) and (b) refer to relative phases of $\phi = 0$ and $\phi = 0.1\pi$, respectively.

chapter, we investigate the possibility of observing these shifts in a more realistic, macroscopic scenario and perform a detailed analysis of how these shifts manifest themselves in a macroscopic medium, for individual orbits. In our investigations we consider H_2 to avoid multielectron effects associated with the core dynamics. In order to obtain a structural minimum within the plateau for intensities well below saturation, we choose an internuclear separation of $R = 2$ a.u., which is larger than the equilibrium value. We consider both linearly polarized fields and bichromatic orthogonally polarized fields given by Eq.(3.103) and (3.104) of frequencies ω and 2ω, respectively. Unless otherwise stated, in this chapter the fundamental pulse (3.103) has wavelength $\lambda = 800$ nm, peak intensity $I_\omega = 2.5 \times 10^{14}$ W/cm^2, and a full width at half maximum of 30 fs (approximately 10 cycles), which are within the experimentally relevant parameter range. For the sake of simplicity, unless otherwise stated (Fig. 5.6), we consider only the ionisation events in the half cycle of the pulse closest to the peak of the pulse.

5.1 Intensity dependence

We will first get an insight on how the phase shift $\zeta(t, t')$ depends on the driving-field intensity. Since this parameter varies strongly across the laser beam profile, a simplified preliminary investigation is useful in order to understand its overall behaviour. To facilitate the interpretation, we will approximate the pulses (3.103) and (3.104) by

monochromatic waves.

In Fig. 5.1, the real parts of $\zeta(t, t')$ are plotted for a specific harmonic, as functions of the driving-field intensity. The figure shows that the shifts depend strongly on the field ellipticity, on the phase difference ϕ between the two waves and on the driving-field intensity. This is expected as variations in the intensity will change the energy position occupied by a specific harmonic. This is related to the fact that, for low enough intensities, these shifts nearly coincide for the long and short orbits. In this case, the harmonic employed is located either at or beyond the cut-off frequency. As the intensity increases, there is a splitting in the shift, indicating that the plateau region has been reached.

The behaviour with regard to the field parameters depends very strongly on the orbit. If the two waves are in phase, for instance [Fig. 5.1(a)], the distinguishing features are a large residual shift after the cut-off and a very pronounced negative shift for the short orbit in the plateau region. Physically, this means that if the electron is returning along the short orbit, for $\phi = 0$ the angle of return is much larger. Hence, it may be easier to single out in a realistic scenario, especially at high intensities.

This behaviour, however, changes with the relative phase. An example is provided in Fig. 5.1(b), which exhibits a smaller residual shift in the cut-off region and comparable shifts of opposite signal if the chosen harmonic is in the high-plateau energy region. Increasing the intensity will lead to a non-trivial behaviour for the shift associated with the short orbit, while the shift related to the long orbit will exhibit a monotonic behaviour. Physically, this implies that the electron's angle of return will vary much more dramatically across the beam for the short orbit.

5.2 Spatial effects across the beam profile

We will first establish how the structural minimum manifests itself in the macroscopic case, and then discuss the situation with OTC fields. Throughout, we have chosen the propagation conditions so that the short orbit is favoured. In general, this is achieved by placing the centre of the gas jet after the focus. This type of configuration leads to an enhancement of on-axis harmonic emission, with low divergence. Furthermore, we have chosen the ionisation times to start shortly after the central maximum of the pulse, so that the corresponding return times will occur near the subsequent crossing.

In Fig. 5.2, we examine the structural minimum across the beam for a linearly polarised field, both near the interaction region and in the far field. This minimum is indicated by the straight vertical lines, which correspond to the interference condition Eq. (3.86), where $\zeta(t, t') = 0$, and agree well with the suppression in the yield. The energy position related to this suppression remains the same regardless of whether con-

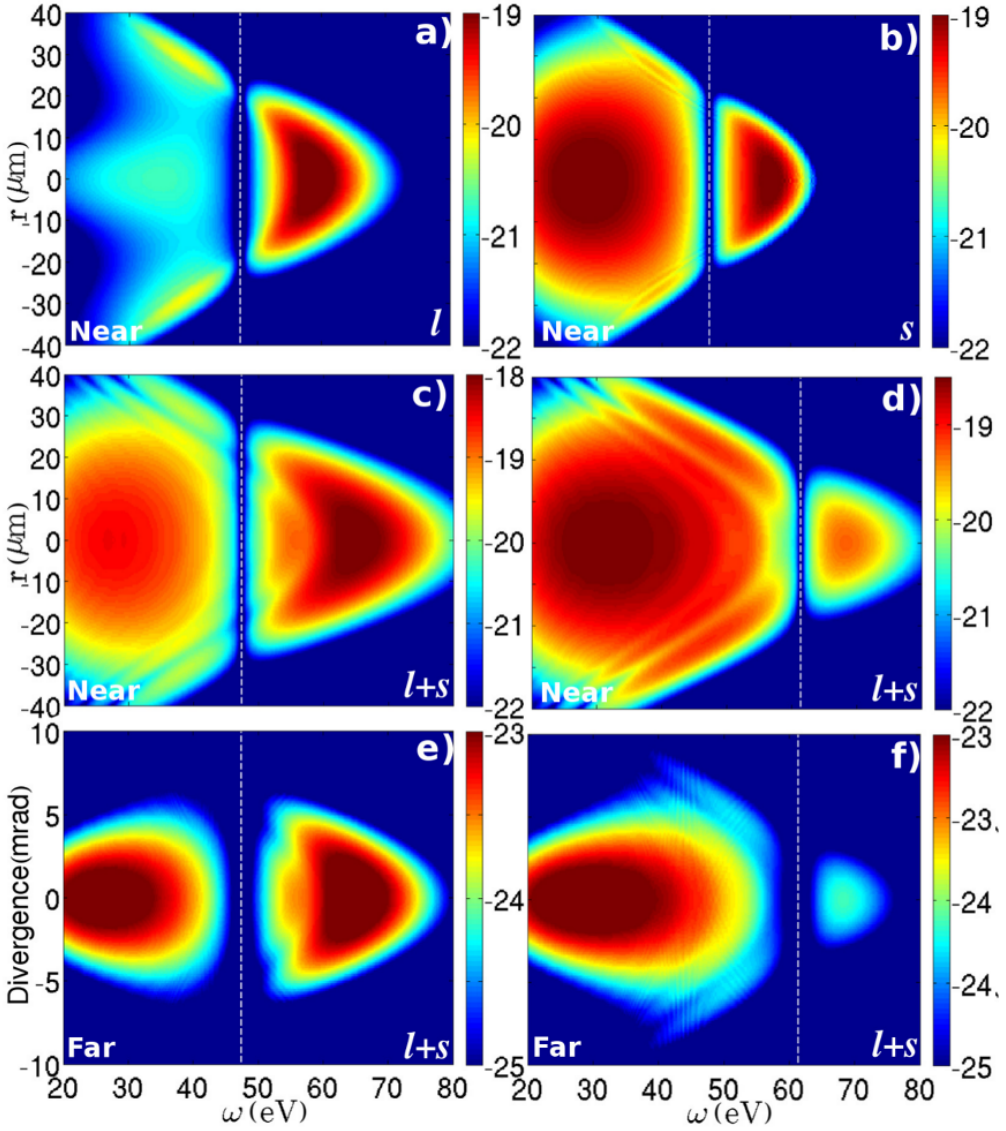

Figure 5.2: HHG macroscopic response of H_2 in a linearly polarised field of wavelength $\lambda = 800$ nm, plotted in a logarithmic scale. The beam waist is $w = 30$ μm, and the gas jet is placed at $z_g = 4$ mm after the focus. The FWHM of the gas jet is 0.5 mm and the FWHM of the intensity envelope is 30 fs. Panels (a) and (b): Individual contributions of the long and short orbits, for a driving-field intensity $I_\omega = 2 \times 10^{14}$ W/cm^2, and alignment angle $\theta_L = 0$; note that the oscillations in Panel (b) are caused by an artefact due the inaccuracy of the standard saddle-point approximation in the cut-off region. Panels (c) and (d): spectra from the coherent superpositions of the long and short orbits, for a driving-field intensity $I_\omega = 2.5 \times 10^{14}$ W/cm^2, and alignment angles $\theta_L = 0$ [panel (c)] and $\theta_L = \pi/6$ [panel (d)]. Panels (e) and (f): far-field harmonic spectra, for the same intensity and alignment angles as in panels (c) and (d). The white dashed line indicates the position of the structural two-centre minimum. The labels s, l and $l+s$ indicate contributions from the short orbit, long orbit, or from a coherent superposition of both, respectively.

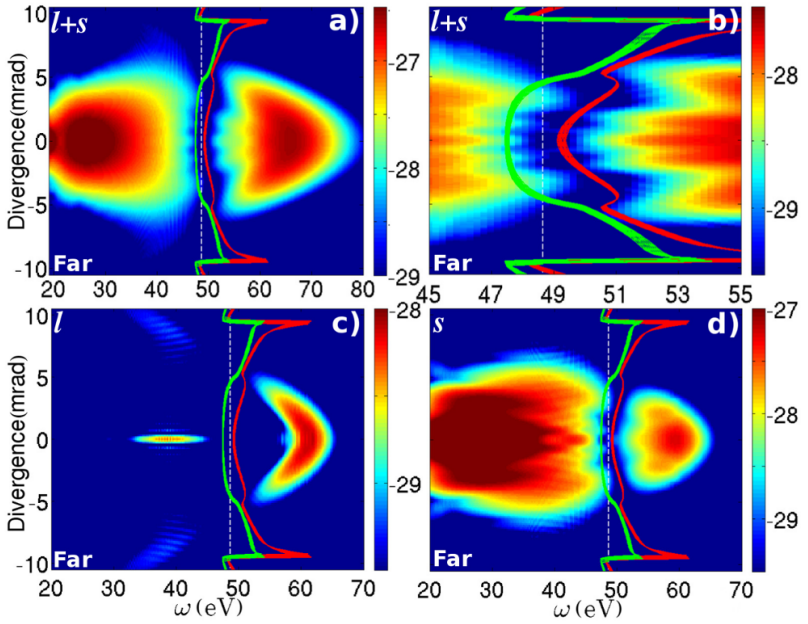

Figure 5.3: Propagated HHG spectra for H_2 in a Gaussian pulse, where the peak intensities of the ω and 2ω waves are $I_\omega = 2.5 \times 10^{14}$ W/cm^2 and $I_{2\omega} = 7.5 \times 10^{13}$ W/cm^2 defined at the gas jet (their intensity ratio is around 0.3) and relative phase $\phi = 0.1\pi$. The wavelength of the fundamental is $\lambda = 800$ nm. The beam waist is $w = 30$ μm and the centre of the gas jet is located at $z_g = 4$ mm after the focus. The FWHM of the intensity envelope is 30 fs. Panels (a) and (b) display the far-field result for a coherent superposition of orbits denoted by the labels $l + s$, where (b) is a close-up of the region around the shifted minimum seen in (a). Panels (c) and (d) show the individual contributions to far field spectra for the long and short orbit respectively. The dashed lines and the solid curves indicate the position of the unshifted and shifted two-centre minima, respectively. The red and the green solid curves give the positions of the shifted minima for the short and long orbits, respectively. The curves have been calculated across the interaction region along z such that $z_g - \Delta z \leq z \leq z_g + \Delta z$, with $\Delta z = 0.5$ mm. All spectra have been plotted in arbitrary units and in a logarithmic scale.

tributions of individual orbits are taken, as shown in panels (a) and (b), or if they are combined, as shown in the remaining panels. Furthermore, it does not change with the driving-field intensity [panel (c)] or in the far-field regime [panels(e) and (f)]. Only when the alignment angle is varied, namely for panels (d) and (f), does this minimum change. All this is consistent with the fact that the two-centre minimum described by Eq. (3.86) is purely structural. The fringes in panels (c) to (f) are caused by the interference of the long and short orbits.

In the upper panels of Fig. 5.3 we present the macroscopic HHG spectrum computed for orthogonally polarised fields considering a coherent superposition of the long and short orbits, and a phase difference of $\phi = 0.1\pi$ between the ω and 2ω waves. This figure illustrates a particular case for which the shift associated with the short orbit, given by the red lines, is visible in a realistic scenario, and survives in the far field. The

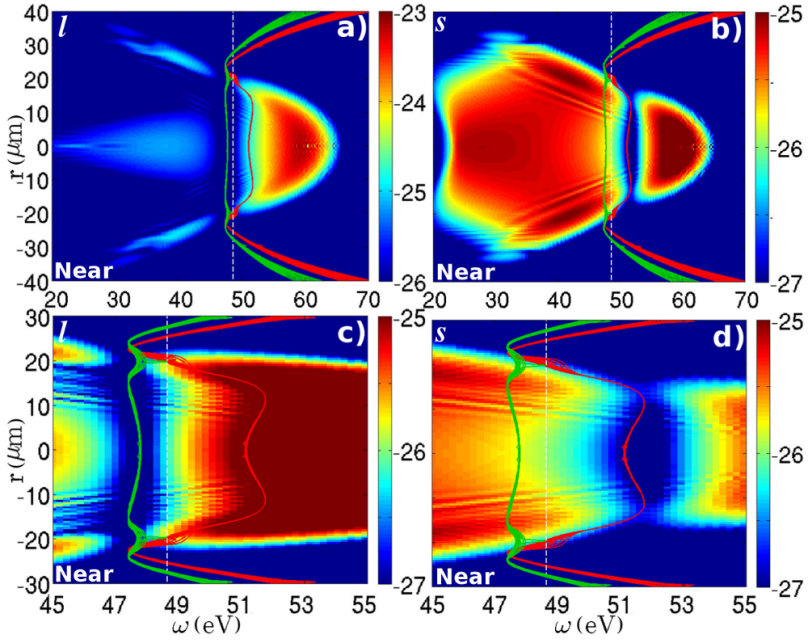

Figure 5.4: Individual contributions of the long and short orbits (left and right panels, respectively) for the HHG macroscopic response of H_2 in a Gaussian pulse. The peak intensities of the ω and 2ω waves are $I_\omega = 2.5 \times 10^{14}$ W/cm^2 and $I_{2\omega} = 7.5 \times 10^{13}$ W/cm^2 defined at the gas jet (their intensity ratio is around 0.3) and relative phase $\phi = 0$. The centre of the gas jet is located at $z_g = 2$ mm after the focus.The wavelength of the fundamental is $\lambda = 800$ nm. The beam waist is $w = 30$ μm, and the FWHM of the intensity envelope is 30 fs. Panels (a) and (b): HHG yield from the individual orbits; panels (c) and (d): zoom in of the upper panels close to the interference minimum. The white dashed lines and the solid curves indicate the position of the unshifted and shifted two-centre minima, respectively. The red and the green curves give the positions of the shifted minima for the short and long orbits, respectively. The curves have been spread equally across the interaction region such that $z_g - \Delta z \leq z \leq z_g + \Delta z$, with $\Delta z = 1$ mm. All panels have been plotted in arbitrary units and in a logarithmic scale. The labels l and s are associated to the long and the short orbit, respectively.

close-up near the interference minimum [Fig. 5.3(b)] shows that it follows the generalised interference condition related to the short orbit very closely. Only at the beam edges there are small discrepancies from this condition, and the suppression approaches the shifted minimum associated to the long orbit, which is given by the green line.

The reason behind this clear picture can be seen in panels (c) and (d) of Fig. 5.3, in which we present the individual contributions from the long and short orbits. They show that the contributions from the long orbit are strongly suppressed in the plateau region, and that those from the short orbit are much more significant. This stems from the fact that the relative phase $\phi = 0.1\pi$ selects the short orbit at the single-molecule level via polarisation gating [107]. This selection is then reinforced by the appropriate propagation conditions. Also for that reason there are no visible fringes when the coherent

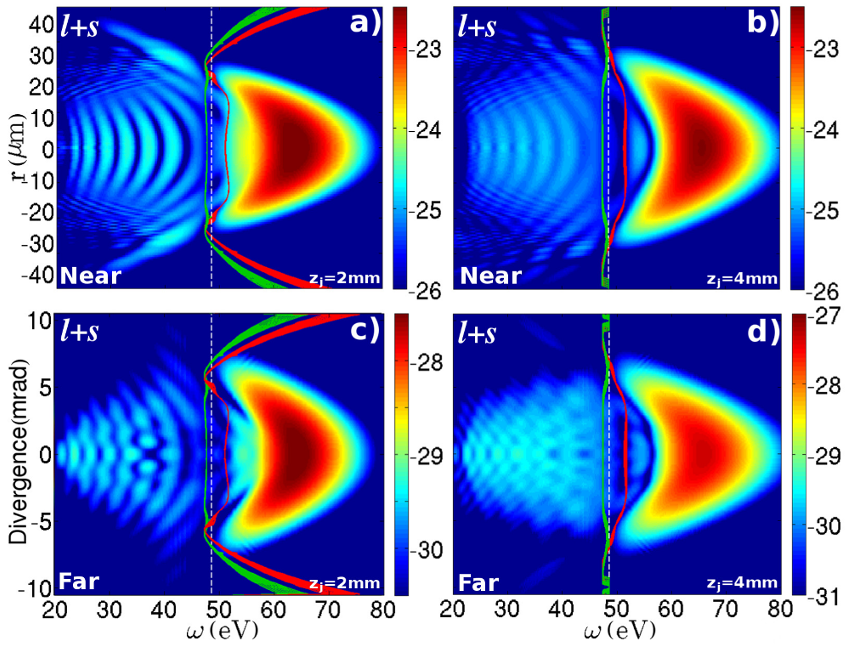

Figure 5.5: Propagated spectra considering a coherent superposition of the long and short orbits, for the same field parameters as in Fig. 5.4. Most propagation conditions have also been kept as in Fig. 5.4 except the centre of the gas jet, which has been chosen to be at $z_g = 2$ mm and $z_g = 4$ mm after the focus (left and right panels, respectively). Panels (a) and (b) display the spectra in the interaction region, while panels (c) and (d) show the far-field results. The white dashed lines and the solid curves indicate the position of the unshifted and shifted two-centre minima, respectively. The red and the green curves give the positions of the shifted minima for the short and long orbits, respectively. The curves have been computed spread equally across the interaction region such that $z_g - \Delta z \leq z \leq z_g + \Delta z$, with $\Delta z = 1$ mm. All spectra have been plotted in arbitrary units, and in a logarithmic scale.

superposition of both orbits is considered (Fig. 5.3).

Next, we will analyse the generalised interference condition for individual orbits in more detail. With that aim in mind, we (i) choose a phase difference $\phi = 0$, for which these shifts are expected to be large [1]; (ii) consider the near-field regime so that diffraction effects are ruled out. These results are plotted in Fig. 5.4, for the short and long orbits. The figure shows that these shifts depend very strongly on the orbit. While, for the long orbit, the shift moves the minimum away from the cut-off and towards lower frequencies, for the short orbit it causes it to move towards the cut-off [see panels (a) and (b)]. Furthermore, a zoom-in of the shifts, presented in panels (c) and (d), shows that they approach each other around the cut-off and follow the modified interference condition (3.85) very closely. In particular, the shift is much larger for the short orbit and, as long as the cut-off has not been reached, it varies very little within the interaction region. For the long orbit, the shift varies slightly more with regard to z. Beyond the

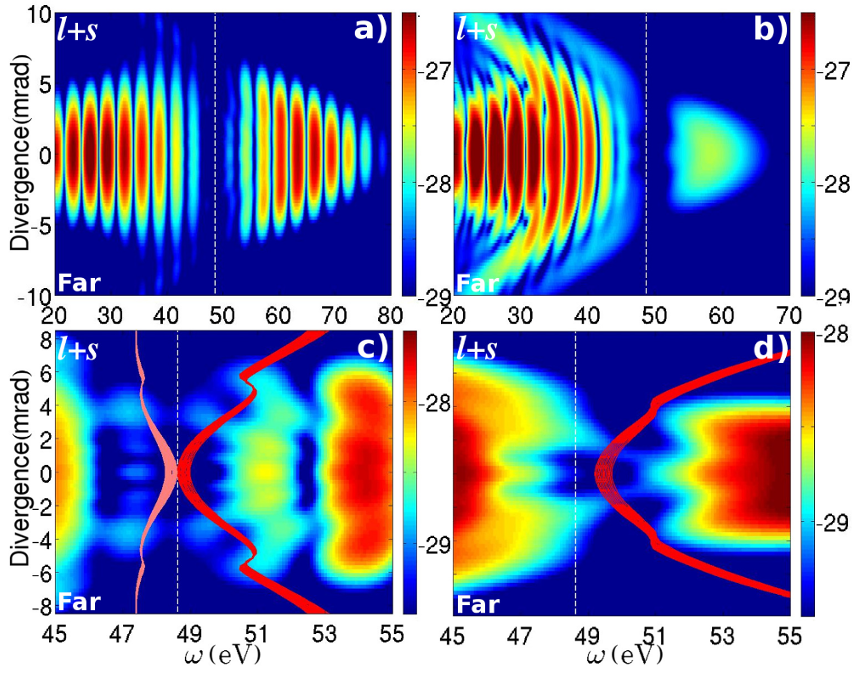

Figure 5.6: Propagated, far-field HHG spectra considering two half cycles, for the same driving-field parameters in Fig. 5.3, but different FWHM of the intensity envelope. In panels (a) and (c), this width is 30 fs, while in panels (b) and (d) it is 5.5 fs. The upper and lower panels show the whole spectra, and a close-up near the interference minimum, respectively. In the lower panels we show only the shift related to the short orbit, which dominates throughout. These shifts are displayed as the thick solid curves in the figure, while the static interference condition is given by the white dashed line. The shifts associated with the first and second half cycle are shown as the red curves in panels (c) and (d), and the pink curve in panel (c), respectively. All spectra have been plotted in arbitrary units and in a logarithmic scale.

cut-off, the variation is more extreme. This region, however, is not of interest to the present problem.

Unfortunately, however, these shifts cannot be seen if a coherent superposition of orbits is considered. We have plotted this superposition in Fig. 5.5, for the near and far field regimes [upper and lower panels in the figure, respectively]. The overall behaviour shows many interference fringes and no clear shifted minimum. This happens because, at the single-molecule response level, a phase $\phi = 0$ will enhance the long orbit and suppress the short orbit [107]. Hence, there are conflicting conditions from the the single-molecule response and propagation, which is not ideal. This is clearly seen in panels (a) and (c) of the figure, which exhibit fringes in the whole plateau region due to the interference between the short and long orbits. Close to the two-centre minimum the results are inconclusive as (i) the suppression near the green curve seems much more related to the interference between the long and short orbit than to the electron's angle of return

being incorporated; (ii) the shift associated to the short orbit does not manifest itself as a clear suppression. Both issues (i) and (ii) become slightly better in the far-field, as the interference between the short and long orbit is partially washed out. Nonetheless, the result is not as clear as in Fig. 5.3, for which the short orbit was favoured at the microscopic and macroscopic level.

This problem may be attenuated by moving the gas jet further away from the focus, in order to favour the short orbit [see Figs. 5.5(b) and (d)]. In this case, the interference fringes in the plateau become more blurred, so that the shift related to the short orbit can be identified.

One should bear in mind, however, that we have restricted the contributing orbits to a single half cycle of the driving field. This does not correspond to a situation attained in all experiments as the pulse may have multiple cycles. A specific problem is that, in a bichromatic $\omega - 2\omega$ field with orthogonally polarised waves, the long and short orbits starting at the subsequent half cycle gives rise to shifts $\zeta(t, t')$ of opposite signs as seen in Chapter 4, [1]. In practice this causes a blurring in the generalised interference condition. This problem may be overcome if one employs a few-cycle pulse.

This is shown in Fig. 5.6, in which we present the far-field spectra calculated using the two dominant half cycles of the pulse in Fig. 5.3, and of a few-cycle pulse with the same parameters, except the full width at half maximum of the intensity envelope (left and right panels, respectively). For the long pulse, the contributions from both half cycles blur the minimum associated with the short orbit [panel (c)], while for the few-cycle pulse it remains very clear. It is also well described by the interference condition (3.85) [panel (d)]. This happens because the two-centre minimum is in the plateau for the first half cycle, while it is beyond the cut-off for the second half cycle of the short pulse. The different cut-off energies become clear in panel (b), which shows well-defined harmonics only for energies lower than the structural minimum. In contrast, the long pulse leads to well-defined harmonics throughout, as seen in panel (a).

5.3 Conclusions

In this chapter, we have performed theoretical studies of the macroscopic response of high-harmonic radiation from diatomic molecules in bichromatic fields composed of two orthogonally polarised driving waves. Our computations show that, for an appropriate choice of driving field and propagation conditions, the angle of return of an electron to its parent molecule manifests itself as a dynamic shift in the two-centre structural minimum. This shift depends on the driving-field intensity, on the harmonic order and on the orbit along which the electron returns. For the dominant orbits, these shifts are visible both in the near- and far-field regimes, indicating that they can, in principle, be measured in

experiments.

In order to see these shifts clearly, one must select an individual orbit by employing gating mechanisms at the single-molecule level and by using appropriate propagation conditions. It is of particular interest to enhance the short orbit and suppress the long orbit, as it phase matches on axis and leads to more dramatic variations in the angle of return with the laser-field parameters. If conflicting microscopic and macroscopic conditions are provided, the interference between long and short orbits may lead to inconclusive results. In order to avoid this problem, we have selected the phase difference between both ω and 2ω driving waves as $\phi = 0.1\pi$ and have placed the focus before the gas jet. These choices are known to enhance the short orbit at the single-molecule [107] and macroscopic [135, 136] levels, respectively. Nonetheless, there exist two obstacles towards seeing this shift, which, however, are well under control. First, for bichromatic fields, the shifts coming from the other half cycle will have opposite sign. This flip may be avoided for few-cycle pulses, by creating a spectral and temporal gate in order to select electron orbits from a single half cycle [136, 144]. This can be performed if for one of the dominant half cycles, the shifted minimum lies beyond the cut-off energy, and within the plateau for the other half cycle, as shown in Fig. 5.6.

Second, for molecules with a more complex electronic structure, the core dynamics may also play an important role, such that the single-active orbital, single-active electron approximation is not applicable [56]. The regime for which this happens, however, can be avoided. Indeed, recent experiments in CO_2 have shown that interference effects stemming from the core dynamics are only relevant if the structural minimum provides a window for them to be observed. For high enough intensities, the energy position of the dynamical minimum lies outside this window and can no longer be observed [78]. This is in agreement with the experimental findings in [145], which support the structural instead of the dynamical interference picture, and with the computations in [146], which show that multielectron effects are important in the cut-off, but not in the mid-plateau energy region.

Finally, our results suggest that, in principle, the angle with which the electron returns to the core can be controlled, either by changing the relative phase between both waves, or the driving-field intensity. As the intensity increases, a specific harmonic moves from the cut-off region across the plateau towards the ionisation threshold, and this will alter the angle of return. This behaviour is particularly critical for the short orbit, which, as discussed above, is the most favourable for macroscopic observations of this shift. Furthermore, this angle can be mapped into a shift near the structural minimum, which can be modified by an appropriate parameter choice. This may be desirable in future experiments in order to investigate dynamic effects which would be obfuscated otherwise.

Chapter 6

Shifted two-centre interference using elliptically polarised fields

In this chapter we will explore the advantages of using an elliptically polarised field over an orthogonal two colour field, when observing the shifted interference minima in HHG spectra. We investigate this at the single molecule response level using an H_2 and Ar_2 as diatomic targets to compare with the results in Chapter 4. We then use Ar_2 to investigate this at the macroscopic response level.

6.1 Single molecule response

In the results that follow we consider an elliptically polarised field given by Eq. (3.58), where $n = 1$ and the phase difference between the parallel and perpendicular fields is $\phi = 0.25$. As in Chapter 4, S_i^j and L_i^j will be used to identify the short and long trajectories, respectively, where i indicates the half cycle the trajectory ionised from and j indicates how many half cycles the trajectory spends propagating in the continuum. We first consider H_2 as a target in Fig. 6.1, where panels (a) and (c) display the individual contributions of the S_1^1 and L_1^1 orbits as functions of the alignment angle θ_L between the internuclear axis and the major polarization axis. We can see in the computed spectra of these panels, that the minimum for the long and short orbit are shifted in opposite directions (shifted right and left, respectively). These observations are confirmed in panel (a) of Fig. 6.2, where we can see that across the whole range of harmonics the shift for long and short is equal but opposite. This can be explained by inspecting the amplitude of the perpendicular vector potential, $\mathbf{A}(t)$, when the electron returns around the crossing of the electric field, i.e $|\mathbf{E}_{||}(t)| = 0$. This is shown in panel (b) of Fig. 6.2, where before and after the field crossing (indicated by the vertical black line) there is a growing equal but opposite perpendicular vector potential $\mathbf{A}(t)$ and therefore a growing perpendicular

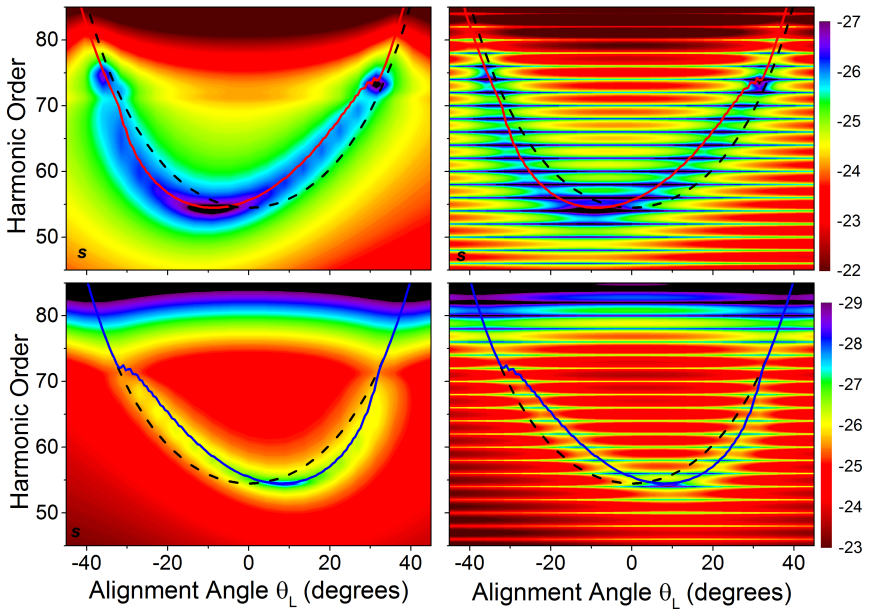

Figure 6.1: Harmonic spectra along the major polarization axis as functions of the alignment angle θ_L for H_2 (I_p =0.25 a.u. and internuclear separation $R = 1.4$ a.u.) in an elliptical field described in Eq. (3.58) with $n = 1$, $\omega = 0.057$ a.u., I=5×10^{14} W/cm^2, $\xi = 0.3$ and time delay $\phi = 0.25$. The top and bottom panels show individual contributions to the HHG spectra for the dominant short and long orbits respectively. The left hand panels consider orbits starting in the first half cycle only, while the panels on the right show a superposition of individual contributions of orbits from the first and second half cycle, respectively. The generalised interference condition (3.85) is indicated by the solid lines in the figures, whereby we have just considered the real parts Re$[\zeta(t,t')]$ of the time-dependent shifts. For comparison, we plot the two-center interference condition for linearly polarized fields as the dashed lines. The central white lines indicate vanishing alignment angle $\theta_L = 0$. The harmonic yield is given in a logarithmic scale. The increase in the harmonic yields after the cutoff observed top panels are related to a breakdown of the standard saddle-point approximation for the short orbits (for details see Ref. [3]).

component of the returning electron momentum. In panels (b) and (d) we coherently add the individual contributions over two half cycles (i.e, $S^1_{1,2}$ and $L^1_{1,2}$, respectively), and we see well defined harmonics as expected, but more interestingly we find a clear shifted minimum in each panel that closely follows the modified interference conditions. This is in contrast to what we have seen for an OTC field, where every half cycle the shift for the long and short orbits flips sign. For elliptically polarised fields the second half cycle reinforces the position of the minima of the first half cycle. The stability of the shift across half cycles can be understood by the fact that both the parallel and perpendicular vector potential change sign every half cycle ($A_{||}(t \pm T/2) = -A_{||}(t)$, $A_{\perp}(t \pm T/2) = -A_{\perp}(t)$) giving us $\zeta(t,t') = \zeta(t \pm \pi/\omega, t' \pm \pi/\omega)$. Also in comparison to what we found previously for OTC fields, the shifts we see in Fig. 6.1 are large. In fact, we can see in Fig. 6.2(a)

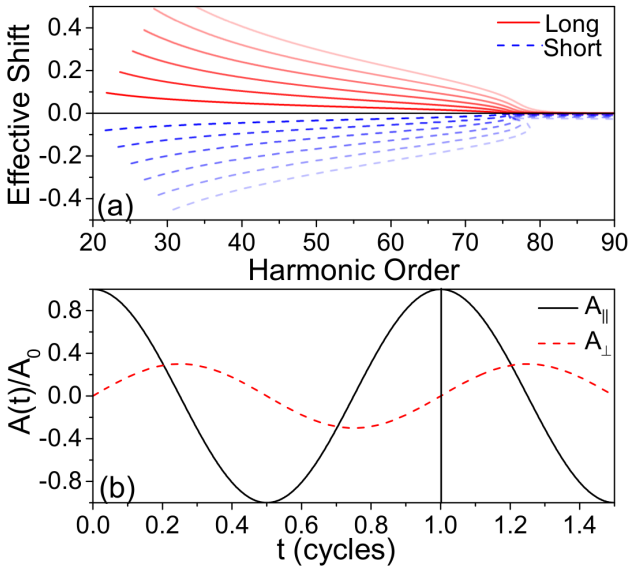

Figure 6.2: Real parts of the effective shifts $\zeta(t, t')$ as functions of the harmonic order computed for long and short orbits [panel (a)] and a schematic representation of the major and minor components of the vector potential A(t) [panel (b)], given by Eq. (3.58) where $n = 1$ and $\phi = -0.25$. The parallel driving field intensity is $I_{||}$=5×10^{14} W/cm^2 and the frequency is $\omega = 0.057$ a.u. In panel (a) the ellipticity has been increased from $\xi = 0$ to $\xi = 0.3$ in increments of $\Delta\xi = 0.05$. A lighter colour indicates a higher ellipticity. The dashed blue lines refer to the short orbit, while the solid red lines correspond to the long orbit. In panel (b) the ellipticity is kept constant at $\xi = 0.3$, and $A_{||}$ and $A_{\perp}$ are indicated by a solid black line and the dashed red lines, respectively.

that as the harmonic order decreases the size of the shift increases. This will be more pronounced if we consider Ar_2, where a large internuclear distance produces several structural interference minima that span a large range of harmonics. In Fig. 6.3, we have computed the individual contributions to the harmonic spectra generated from Ar_2 for S_1^1 and L_1^1, in panel (a) and (b), respectively. We can see that as the minimum extends to lower harmonics the shift becomes extremely large. This is useful as it is well known that elliptically polarised fields cause significant drops in the harmonic yield. For this reason it is favourable to use orthogonal two colour fields when the yield is an important factor. But because the elliptical field produces such a large shift, it means that the ellipticity of the field can be reduced, therefore reducing the detrimental effects on the HHG yield whilst still being able to observe the shift. In panels (d) and (e) we can see again that the shift is still visible when a second half cycle is considered.

In Fig. 6.3(e) we have taken a coherent superposition of S_1^1 and L_1^1. Because the shifts are equal but opposite for the long and short orbit, we lose the clear minimum observed in previous figures and a more symmetrical spectrum is observed. Looking closely at

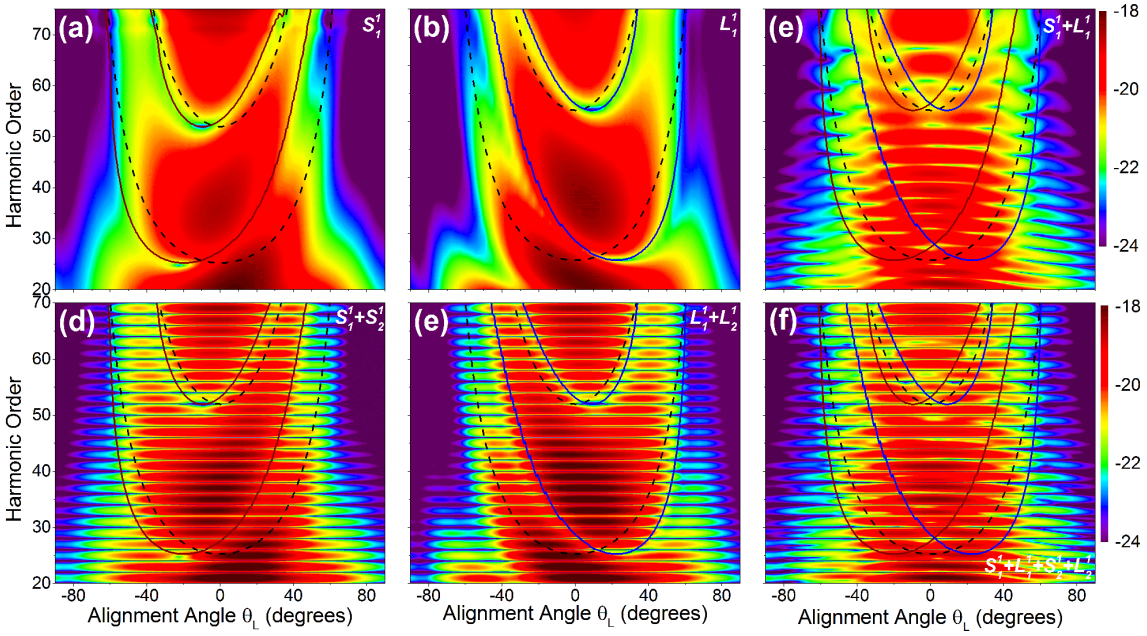

Figure 6.3: Harmonic spectra along the major polarization axis as functions of the alignment angle θ_L for Ar_2 ($I_p = 0.58$ a.u. and internuclear separation $R = 7.2$ a.u.) in an elliptical field described in Eq. (3.58) for $n = 1$, $\omega = 0.057$ a.u., I=5×10^{14} W/cm^2, $\xi = 0.3$ and time delay $\phi = -0.25$. The first of row panels show the HHG spectra when considering contributions from only short orbit, the long orbit and the coherent superposition of the short and long orbits from one half cycle of the driving laser field. The second row is the same as the first excepted orbits starting from the second half cycle are also considered. The generalized interference condition (3.85) is indicated by the solid lines in the figures, whereby we have just considered the real parts Re$[\zeta(t, t')]$ of the time-dependent shifts. For comparison, we plot the two-centre interference condition for linearly polarized fields as the dashed lines. In the figure, only the interference minima corresponding to $n = 2$ and $n = 3$ in Eq. (3.85) are shown. The harmonic yield is given in a logarithmic scale.

the minimum $n = 2$ [see Fig. 4.6 for minima labels], we can see that it has split and is partly following the shifted interference conditions for the long and short orbits, and the linear interference condition. Adding a second half cycle in panel (f) slightly washes out the splitting minimum due to the appearance of well defined harmonics. We also see in Fig. 6.3, that the shifted interference condition for the long and short orbit meet in two places: First, at the cut-off and second at the $\theta_L = 0$. Where they meet at $\theta_L = 0$, there is a strong localised suppression, which is well above the linear condition. Hence along both these trajectories the electron is returning with a non-vanishing angle. This suppression could be used to extract the angle of return of the electron from the spectrum if a coherent superposition of orbits were considered. It is easy to see why the shifted interference minima for the short and long orbit meet if we look at Eq. (3.85), which for $\theta_L = 0$ reduces to

$$\Omega = \frac{2[n\pi - \alpha]^2}{R^2 \cos^2(\zeta(t,t'))} + I_p. \tag{6.1}$$

Because the cosine squared in this equation is a even function, if the shift for the long and short orbits are equal magnitude (which is the case for a $\phi = 0.25\pi$, see Fig. 6.2), the harmonic order the minimum will appear at in the spectrum will be the same for both orbits. If the shift for long and short orbit are not equal, they will still meet in the spectrum but at non-zero values of θ_L. In the previous investigation using an orthogonal two colour field, the shifted minima for the long and short trajectories also meet at or close to $\theta_L = 0$. However, the shift is small compared to the size of the shift we find using elliptically polarised fields. Therefore, the minima meet close to the linear two-centre interference condition. This would make it difficult to measure, although not impossible.

6.2 Propagated macroscopic harmonic response

In the results that follow, we investigate how the shifted two centre interference minimum from an elliptically polarised field manifests itself in a macroscopic harmonic response. The field is given by Eq. (3.103) and (3.104), where the pulse shape $f(t)$ is a Gaussian function. In Fig. 6.4, we have chosen to use a wavelength of $\lambda = 1300$ nm in order to compute a finer comb of harmonic peaks. This makes it easier to distinguish between the minimum and signal suppression between harmonics when two or more half cycles are considered. We consider a peak intensity of $I_\omega = 1 \times 10^{14}$ W/cm^2 and a full width at half maximum of 30 fs (approximately 10 cycles). This pulse has approximately 60 cycles, which means that it may be approximated by a monochromatic wave.

We have positioned the gas jet at z_j=5 mm after the position of the focus, which produces phase matching conditions that are detrimental to the survival of the propagating long trajectories, but are favourable for the short. The effect of these phase matching conditions can be seen in panel (a) as the lack of temporal interference between S_1^1 and L_1^1 [See panel (d) of Fig. 5.2 for comparison]. In this panel there is a very noticeably large and clear suppression in the spectrum. This is the two centre minimum corresponding to $n = 2$ that has been shifted to lower harmonic energies due to the perpendicular component of the field giving the propagating electron a perpendicular push. As we know from Fig. 4.6, Ar_2 has three minima resulting from two-centre interference. These other minima are not present because they are positioned outside the range of harmonics for the spectra computed in these figures. In fact the minimum corresponding to $n = 1$ is positioned far above the cut-off of the spectrum at 91 eV and the minimum corresponding $n = 3$ is positioned below the range of the spectrum computed. In panel (b) we include contributions from $S_1^{2,3}$ and $L_1^{2,3}$. These pairs of orbits spend longer propagating

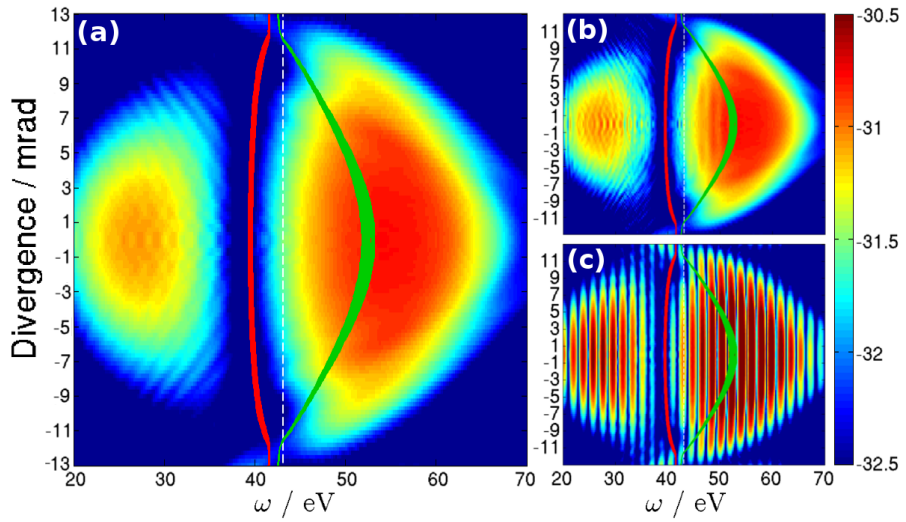

Figure 6.4: Propagated Far field HHG spectra for Ar_2 in a Gaussian pulse, where the peak intensities of the parallel and perpendicular components of the elliptically polarised field at the gas jet are $I_\omega = 1 \times 10^{14}$ W/cm^2 and $I_{2\omega} = 1 \times 10^{13}$ W/cm^2 (intensity ratio = 0.1) and relative phase $\phi = 0.25\pi$. The wavelength of both components is $\lambda = 1300$ nm. The beam waist is $w = 30$ μm and the centre of the gas jet is located at $z_g = 5$ mm after the focus. The FWHM of the intensity envelope is 30 fs. Panel (a) show a HHG spectrum from a coherent superposition of the long and short orbit from one half cycle of the field. Panel (b) is the same as (a) but includes contributions from the three most dominant pairs of orbits (i.e. orbit pairs ionising and returning between one and three half cycles). Panel (c) is also the same as panel (a) but it includes the two dominant orbits from a second half cycle of the field. The dashed lines and the solid lines indicate the position of the unshifted and shifted two-centre minima, respectively. The red and the green solid lines give the positions of the shifted minima for the short and long orbits, respectively. All spectra have been plotted in arbitrary units and in a logarithmic scale.

in the continuum and lead to a different plateau and harmonic cut-off. This can be seen in Fig. 3.2 (a) and (b), where these orbit pairs return with a smaller maximum kinetic energy when compared to S_1^1 and L_1^1 which returning within a cycle and therefore have a lower cut off in the high harmonic spectrum. These orbits have little effect on the clarity of the minimum in the spectrum calculated in panel (b), even though the minimum falls within the plateau of their contributions. The only effect is finer temporal oscillations in the lower harmonics. This is fortunate as it suggests that the suppression of these longer trajectories may be unnecessary when trying to observe the shifted minimum. However, if this did become a problem a small adjustment to the alignment angle θ_L would move this minimum to higher harmonic energies and above the cut-off for these longer orbit contributions. In fact we can see in Fig. 6.3 that around $\theta_L = -\frac{1}{18}\pi$ $(-10°)$ the shifted interference condition meets the linear condition. At either side of this alignment angle, the minimum is shifted to higher or lower harmonic energies. Thus, changing the alignment angle from $\theta_L = \frac{2}{16}\pi$ to $\theta_L = -\frac{1}{16}\pi$ would shift the minimum to higher energies for

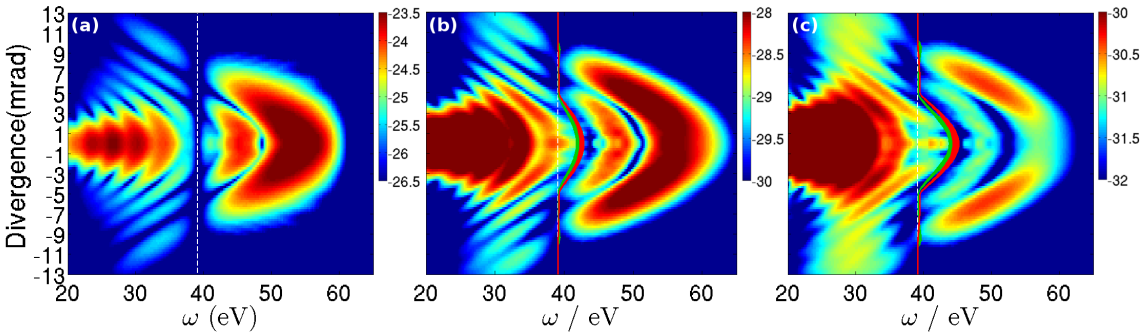

Figure 6.5: Propagated Far field HHG spectra for Ar_2 in a Gaussian pulse, where the peak intensities of the parallel component of the elliptically polarised field at the gas jet is $I_{\parallel} = 2 \times 10^{14}$ W/cm^2 and the perpendicular component is $I_{\perp} = 0 \times 10^{13}$ W/cm^2 (linear), 4×10^{13} W/cm^2(intensity ratio = 0.2) and 6×10^{13} W/cm^2 (intensity ratio = 0.3) for panel (a), (b) and (c) respectively. In all the panels, the relative phase is $\phi = 0.25\pi$ and the wavelength of both components is $\lambda = 800$ nm. The beam waist is $w = 30$ μm and the centre of the gas jet is located at $z_g = 1.5$ mm after the focus. The FWHM of the intensity envelope is 30 fs. All panels show a HHG spectrum from a coherent superposition of the long and short orbit from one half cycle of the field only. The dashed lines and the solid lines indicate the position of the unshifted and shifted two-centre minima, respectively. The red and the green solid lines give the positions of the shifted minima for the short and long orbits, respectively. All spectra have been plotted in arbitrary units and in a logarithmic scale.

these particular parameters. In panel (c) we have included the dominant pairs of orbits starting at the first and second half cycle ($S^1_{1,2}$ and $L^1_{1,2}$), ignoring the contributions from longer pairs of orbits from both half cycles. What we find is that the shift in the two-centre interference minimum for the dominant orbits ionising in the second half, is exactly the same as the first half cycle and the result is a very clear minimum. This was expected from our results in Sec 6.1 and is in contrast to what we see for bichromatic fields (see Chapters 4 and 5), where every half cycle the shift changes sign causing blurring of the minimum. Thus, individual shifts become extremely difficult to observe, unless a few cycle pulse is used.

In Fig. 6.5 the calculated HHG spectrum for Ar_2 aligned parallel to the field ($\theta_L = 0$) is shown for increasing ellipticity from $\xi = 0$ (linearly polarised) to $\xi = 0.2$ and $\xi = 0.3$. The gas jet has been positioned at $z_j = 1.5$ mm after the focus in order to produce good phase matching conditions for the long orbit as well as the short. We can see that this is the case because temporal interference patterns are present in all the panels. The note worthy feature in these panels is the presence of a shifted two-centre minimum as the ellipticity of the driving laser field is increased. In panel (a), where a linearly polarised field has been employed, we have a completely vertical minimum that cuts across the divergence of the harmonic signal. In panel (b) a perpendicular field is introduced that is 20% as intense as the parallel field. This causes the vertical minimum on-axis to "*bend*" to higher harmonic energies. Notice that the calculated shift for the long and

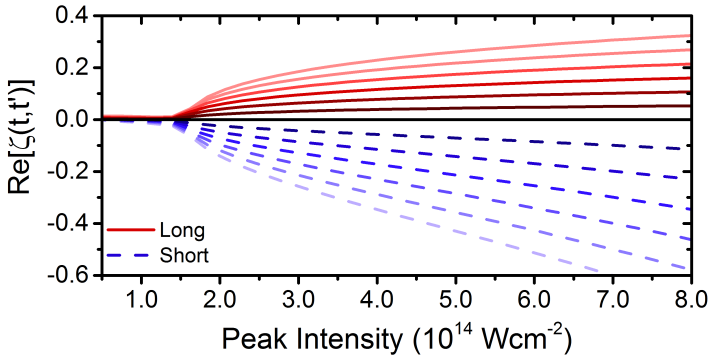

Figure 6.6: Real parts of the effective shift, $\zeta(t, t')$ as functions of the driving-field intensity I_ω of the fundamental for a harmonic of frequency $\Omega = 31\omega$, using Ar_2 (I_p= 0.58 a.u.) in an elliptically polarised laser field described in Fig. 6.5 where the ellipticity has been increased from $\xi = 0$ to $\xi = 0.3$ in increments of $\Delta\xi = 0.05$. A lighter colour indicates a higher ellipticity. The dashed and solid lines refer to the short and long orbits, respectively.

short orbit, given by the green and red curves respectively, are almost exactly the same and closely follow the shifted minima in the calculated spectra. This is predicted by Eq. (6.1), when the shift for the long and short trajectory are the same in magnitude (see Fig. 6.2). Harmonics generated on-axis are exposed to the most intense part of the profile of the driving laser field. Fig. 6.6 shows that for these particular field parameters the greater the intensity of the driving fields translates to a greater effective shift to the interference minimum. This behaviour can be seen in panel (b) and (c) of Fig. 6.5, where the largest shift to the minimum is on-axis where the divergence is zero. The size of the shift decreases off-axis as the intensity of the field decreases, until the shift is so small that it meets the linear condition. It important to note that Fig. 6.2 also shows that as the peak intensity of the driving field is increased the magnitude of the shift experienced by the short trajectory becomes increasingly greater then the that experienced by the long. This disparity should be avoided if one wants the corresponding shifted minima to meet at $\theta_L = 0$. It is also expected that the shift will increase as the ellipticity of the field is increased, which is what we find if we compare panel (b) to panel (c) of Fig. 6.5. Here the intensity ratio between the parallel and perpendicular waves of the driving field has been increased from $\xi = 0.2$ to $\xi = 0.3$, resulting in an increased "*bending*" of the minimum to higher harmonic energies.

This is an important result as previously we had to suppress one of the trajectories in order to see the shifted minimum, as a coherent superposition of equally contributing orbits led to blurring. Here we have demonstrated that it is possible to extract the electron's angle of return for situations where it is difficult to isolate the contribution of an individual trajectory to the HHG spectrum.

6.3 Conclusion

Using an elliptically polarised field instead of an orthogonal bi-chromatic field has its advantages and disadvantages. The main disadvantage is that the HHG yield is diminished much more quickly as the ellipticity of the field is increased in comparison to OTC fields. Nevertheless, in this investigation we have found many advantages. First, the shift is much larger when using an elliptically polarised field. This allows us to decrease the strength of the perpendicular component of the field in order to maintain a good harmonic yield without losing our ability to clearly observe the shifted minimum. The second advantage is that the shift is the same every half cycle, reinforcing the position of the shifted minimum every time another half cycle is coherently added. This eliminates the need to use a few cycle pulse so that any pulse of any length is usable. Lastly for this particular phase of $\phi = 0.25$, when the internuclear axis of the molecular target is in line with the parallel component of the elliptical polarised field (i.e, $\theta_L = 0$), the shifted minimum for the long and short orbit meet well above the linear condition, with a very large shift. Unlike in our previous work in chapter 5, choosing this alignment in a experimental setting eliminates the necessity to suppress one of the dominate trajectories in order to observe the shifted minimum. This may be useful in situations where it is difficult to isolate one particular orbit, or where it is desirable to keep both orbit contributions in a macroscopic setting.

Chapter 7

Shifting nodal planes suppressions in HHG spectra

Another well known structural feature in the HHG from aligned molecules is that, when a nodal plane is in alignment with the polarisation of the field, there is a drop in HHG efficiency across the whole spectrum (see, e.g., [99, 56, 48, 57]). This suppression arises from the fact that nodal planes are areas of vanishing probability density in the wavefunction of a molecule. This means that either ionisation is strongly suppressed or that the overlap between the recolliding electronic wave packet and the core wavefunction is vanishingly small [147, 148, 149]. One should note that this specific feature is related to the geometry of the orbital with which the active electron recombines, and not to the structural interference studied in [1, 2]. Thus, nodal planes provide an additional tool to those discussed in our previous work [1]. This type of suppression has been often identified in theoretical HHG harmonic spectra and ionisation probabilities as functions of the alignment angles, computed using not only the SFA [58, 66], but also other methods such as the numerical solution of the time-dependent Schrödinger equation (TDSE) [148, 149]. Further studies in [58] compared the signals of nodal planes in isoelectronic homonuclear and heteronuclear diatomic molecules in HHG spectra. For the latter case the nodal planes were distorted into nodal surfaces. This caused the suppression in the spectrum to appear at different angles, in comparison to the homonuclear molecule. Similar distortions appear in the HHG spectra calculated in [66] for HHG in elliptically polarised fields, but they have not been analysed. Therein, the suppressions related to nodal planes appear to shift and bend if the ellipticity of the driving field is increased [66]. Chapters 4 and 5 indicate that the origin of these distortions lie in dynamic effects introduced by the electron's returning angle. Furthermore, previous publications that have addressed nodal plane suppressions and elliptical fields [150, 62] have focused on ionisation, but not on recombination. They found that, although, on their own, nodal planes and elliptical

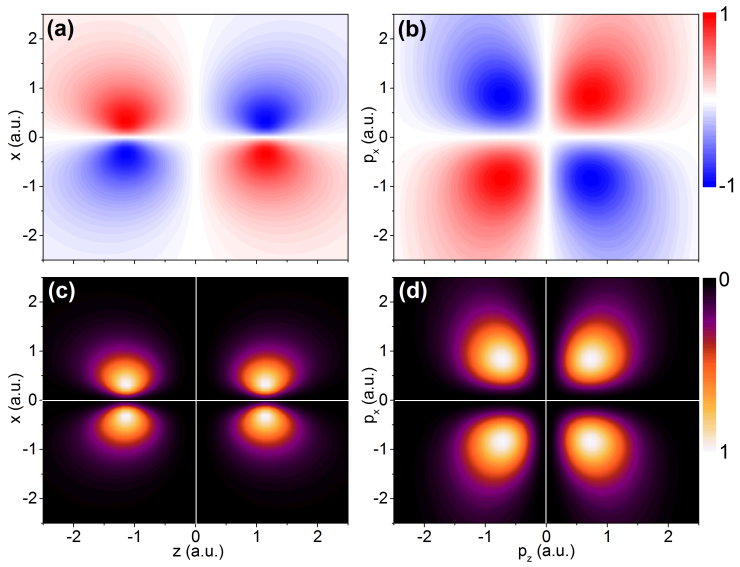

Figure 7.1: Panels (a) and (b) show the real parts of the position- and momentum- space wave functions of the HOMO of O_2, respectively, computed using Eq. (3.59) and its Fourier transform. Panels (c) and (d) show the corresponding probability densities $|\Psi_0(\mathbf{r})|^2$ and $|\Psi_0(\mathbf{p})|^2$, respectively. The HOMO of O_2 is a $1\pi_g$ orbital with ionisation potential $I_p = 0.441$ a.u. and internuclear separation $R = 2.28$ a.u., with two perpendicular nodal planes. The position of the nodal planes are designated by the white lines in the lower panels. The contours have been normalised to the maximum amplitude in each panel, and the blue [red] lobes correspond to the negative [positive] values of the real parts of the wave functions. In this picture, the internuclear axis is oriented along the z axis.

fields suppress ionisation, the combination of both can in fact compensate for each other. This increases the HHG signal when the major polarisation axis and the nodal plane are in alignment.

In this chapter, we focus on how introducing a second orthogonally polarised field influences the HHG suppression caused by nodal planes. We also investigate which type of driving fields, elliptically polarised or OTC fields, for which $n = 1$ and $n = 2$ in Eq. (3.58), respectively, is the most appropriate for observing such distortions. Using the equation for the effective shift of a returning electron presented in [1], we are able to predict where in the spectrum the nodal suppression will appear for a particular harmonic. In the previous chapters we used shifted two-centre interference patterns to learn about an electron's angle of return to its parent molecule. In this chapter we show that the typical suppression in the HHG spectra associated to nodal planes is distorted and that this distortion can also be employed to map the electron's angle of return to its parent ion, but with the advantage of larger shifts for a possibly easier extraction at a macroscopic level. This investigation is performed semi-analytically at the single-molecule response, employing the single-active electron, single-active orbital approximation and neglect core

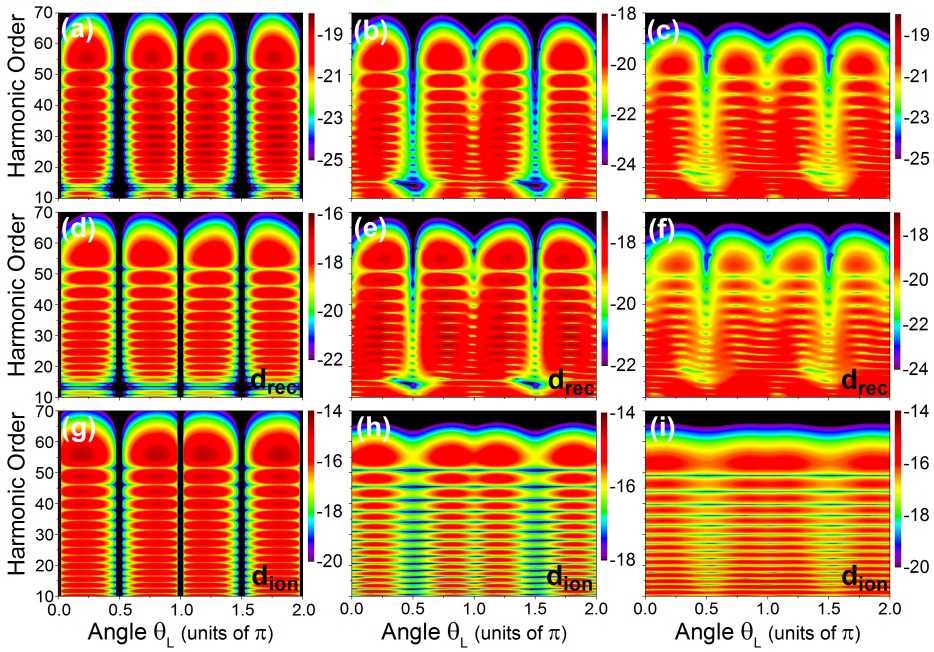

Figure 7.2: Contributions $|M(\Omega)|^2$ of the dipole component along the major polarisation axis to the HHG spectra computed using the length form of the dipole operator for a coherent superposition of the dominant long and short orbits, as functions of the alignment angle θ_L for O_2 (I_p =0.441 a.u. and internuclear separation $R = 2.28$ a.u.) in an elliptical field described in Eq. (3.58) with $n = 1$, $\omega = 0.057$ a.u., I=4×10^{14} W/cm^2 and time delay $\phi = 0.25$. The complete prefactor is calculated in the first row while only the recombination and ionisation prefactors are used to calculate the spectra in the second and third row respectively. The first, second and third column give an increasing value of the field ellipticity of $\xi = 0, 0.15$ and 0.3, respectively. In each panel the harmonic yield is given in a logarithmic scale.

dynamics. The latter issue has been addressed in, for instance, [56, 63].

In this study we also address some of the limitations of the SFA. Apart from the gauge dependence and its influence on the structural interference [93, 94, 116], different forms of the recombination dipole matrix element affect the HHG spectra [99, 111, 112]. The most appropriate form to be used has raised considerable debate in the context of the tomographical reconstruction of molecular orbitals [113, 114, 115]. It is generally accepted that the velocity form is superior when dealing with molecules, but that the artefacts introduced by the length form are under control and can be eliminated. In this work, we revisit this issue and show that orthogonally polarised fields expose artefacts in the length form of the SFA, which cannot be probed with linearly polarised fields.

Throughout we employ O_2 as a molecular target, which is particularly convenient since its HOMO is a $1\pi_g$ orbital [see Fig. 7.1], composed of two p orbitals of opposite phases. This leads to two nodal planes that are perpendicular to each other and produce suppressions in the HHG signal when the molecular axis of O_2 is aligned at $\theta_L = 0, \pi/2$,

π, and $3\pi/2$ with respect to the major polarisation axis of the field. It is also possible to avoid the effects of two-centre interference by an appropriate choice of driving-field intensity. In this specific case, the derivative of the momentum-space wavefunction in the direction of the main polarisation axis, needed to compute the length form of the recombination prefactor Eq. (3.18), reads

$$\partial_{p\parallel}\psi_a(\mathbf{p}) = \left(-\frac{i}{2}\right)^{\ell_a} b_a c_a \pi^{\frac{3}{2}} \chi_a^{-\ell_a-\frac{3}{2}} e^{-(p_\parallel^2+p_\perp^2)/(4\chi_a)} \left[\mathcal{K}_1(p_\parallel, p_\perp, \theta_L) + \mathcal{K}_2(p_\parallel, p_\perp, \theta_L)\right], \tag{7.1}$$

where

$$\mathcal{K}_1(p_\parallel, p_\perp, \theta_L) = -\ell_a \sin\theta_L (-p_\parallel \sin\theta_L + p_\perp \cos\theta_L)^{\ell_a - 1} \tag{7.2}$$

and

$$\mathcal{K}_2(p_\parallel, p_\perp, \theta_L) = -\frac{p_\parallel}{2\chi_a}(-p_\parallel \sin\theta_L + p_\perp \cos\theta_L)^{\ell_a}. \tag{7.3}$$

In Eqs. (7.1)-(7.3), b_a and χ_a give the contraction and the exponential coefficients, respectively. We employ either a coherent superposition of the two dominant, shortest pair of orbits (S_1^1 and L_1^1), or their individual contributions, as it was found in Chapter 4 and 6 that the remaining orbits do not play a very important role for orthogonally polarised fields [1]. For clarity, in the results that follow we restrict the electron ionisation times to the first half cycle of the driving field.

7.1 Individual prefactors

We begin by focusing on the overall changes introduced by an elliptically polarised field ($n = 1$ in Eq. (3.58)) of the position of the nodal-plane suppressions in the HHG spectrum for the target molecule O_2. These changes are presented in the first row of Fig. 7.2, for increasing driving-field ellipticity [Figs. 7.2(a) to (c)]. We find that the suppressions begin to weaken and that the alignment angle for which they appear in the spectrum changes. This weakening and shifting in position decreases for increasing harmonic order and seems to behave differently for suppressions originally positioned at even and odd multiples of $\pi/2$ for linearly polarised fields. For $\theta_L = n\pi$, we observe more blurring and larger shifts, in comparison to the behaviour near $\theta_L = (2n+1)\pi/2$.

In the remaining rows of Fig. 7.2, we show the effect of using only the recombination or the ionisation prefactor in the calculation of $|M(\Omega)|^2$ (second and third row, respectively). These figures show us that, as the ellipticity of the field is increased, the structure of the shifted nodal-plane suppressions is determined by the recombination prefactor. All the structure in the ionisation prefactor is washed out for large enough ellipticity. This is in agreement with [62], which found that, although the effect of the nodal plane and ellipticity of the field by themselves are detrimental to HHG, the combination of both

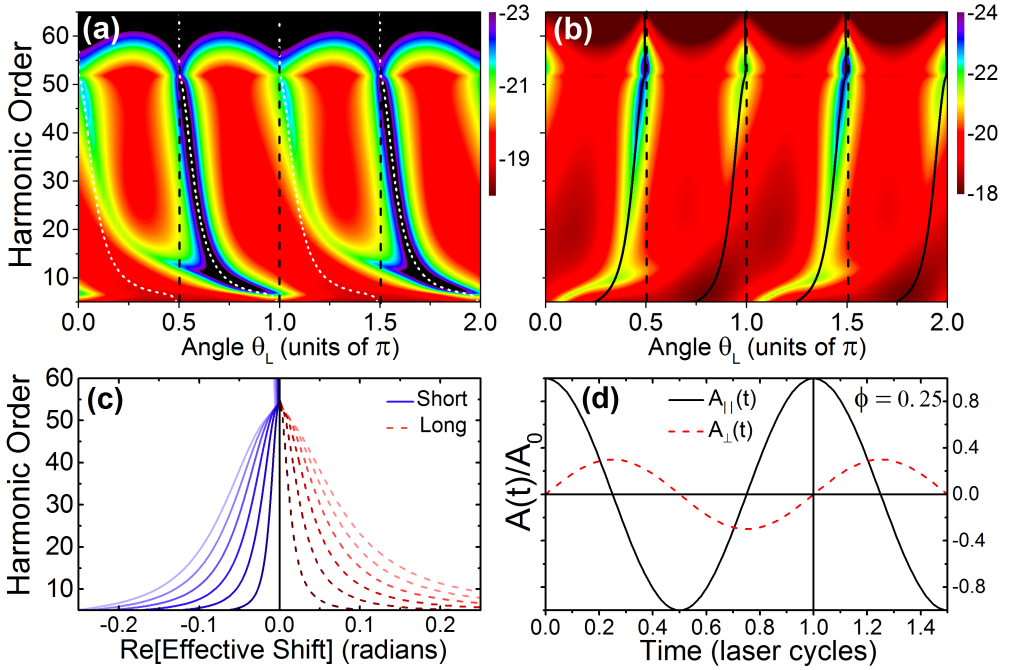

Figure 7.3: (Color online) Panels (a) and (b) show the transition probabilities $|M(\Omega)|^2$ for individual orbits along the major polarisation axis as functions of the alignment angle θ_L for O_2 in an elliptical field described by Eq. (3.58), using the same parameters as in Fig. 4.1 and using the length form of the dipole operator. Panel (a) [Panel (b)] shows the individual contributions from the long [short] orbit. In panel (a), the shifted positions of the nodal-plane suppression calculated using $\mathrm{Re}[\zeta(t,t')]$ given by Eq. (3.84) are indicated by the white short dashed curves, and in panel (b) they are given by the solid black lines. For comparison, we also indicate the position of the nodal-plane suppression for linearly polarised fields as the dashed black lines. The harmonic yield is given in a logarithmic scale. The increase in the harmonic yields after the cut-off observed in panel (b) is related to a breakdown of the standard saddle-point approximation for the short orbit (for details see Ref. [3]). In panel (c) we have plotted the real parts of the effective shifts $\zeta(t,t')$ as functions of the harmonic order computed for the long (red dashed curves) and short (blue solid curves) orbits in laser fields of increasing ellipticity and the same relative phase, intensity and frequency as in panels (a) and (b). The ellipticity has been increased from $\xi = 0$ to $\xi = 0.3$ in increments of $\delta\xi = 0.05$. A lighter colour indicates a higher ellipticity and a vanishing shift is indicated by a horizontal black line. Panel (d) shows a schematic representation of the major and minor components of the vector potential $\mathbf{A}(\mathrm{t})$ for ellipticity $\xi = 0.3$ and relative phase $\phi = 0.25$. The electron return time at $t = 2\pi/\omega$ is indicated by the thick vertical black line in the figure. For simplicity, all fields have been normalised to the vector potential amplitude $\mathrm{A}_0 = \mathrm{E}_0/\omega$.

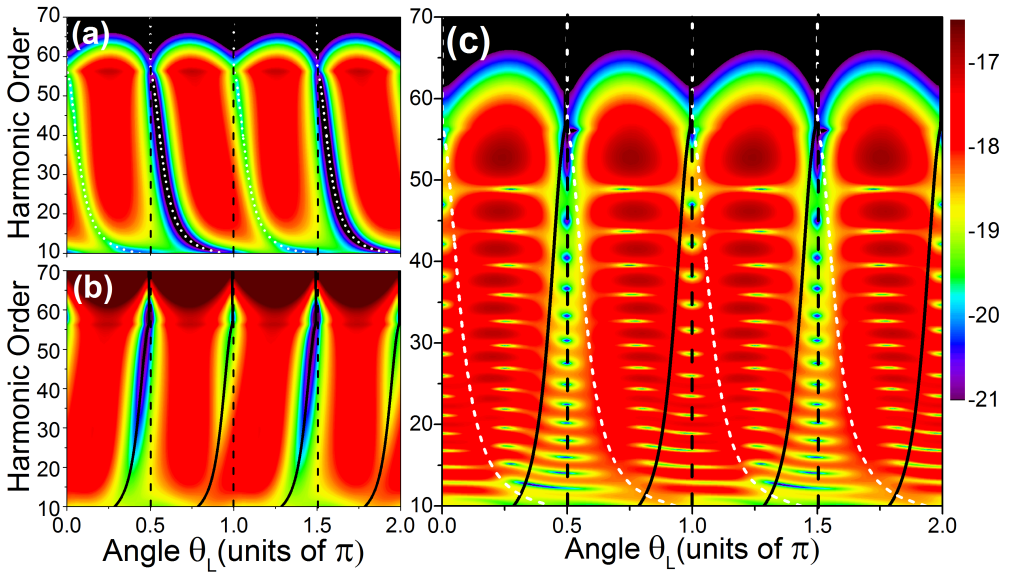

Figure 7.4: Panels (a) and (b) show the transition probabilities $|M(\Omega)|^2$ for the long and short individual orbits respectively as functions of the alignment angle θ_L for O_2 in an elliptical field described in Eq. (3.58) using the same parameters as in Fig. 7.2, but calculated using the velocity form of the dipole matrix elements. Panel (c) shows $|M(\Omega)|^2$ for a coherent superposition of the dominant long and short orbits considered in Panels (a) and (b). The shifted positions of the nodal-plane suppression calculated using $\mathrm{Re}[\zeta(t,t')]$ are indicated by the white short dashed curves for the long orbit, and by the solid black lines for the short orbit. For comparison, we also indicate the position of the nodal-plane suppression for linearly polarised fields as the dashed black lines.

can compensate for each other.

7.2 Individual orbits and different SFA forms

In the upper row of Fig. 7.3, we show the transition probabilities $|M(\Omega)|^2$ associated with individual orbits as functions of the alignment angle θ_L. The contributions from the long and short orbits are displayed in panels (a) and (b), respectively. Throughout, we observe an excellent agreement between Eq. (3.84) and the outcome of the SFA computations for the nodal plane-suppressions that are positioned at $\theta_L = (2n+1)\pi/2$ for linearly polarised fields. Furthermore, in agreement with what was found in Chapter 4, the positions of the suppressions are orbit dependent. The shift for the long orbit displaces the nodal-plane suppressions to the right, while for the short orbit this displacement is to the left. We also see that the displacement decreases for both orbits with increasingly higher harmonics. At the cut-off, the shifts vanish and the suppressions occur at $\theta_L = (2n+1)\pi/2$, as in the linearly polarised case.

The above-stated observation for these parameters can be explained with Fig. 7.3(c),

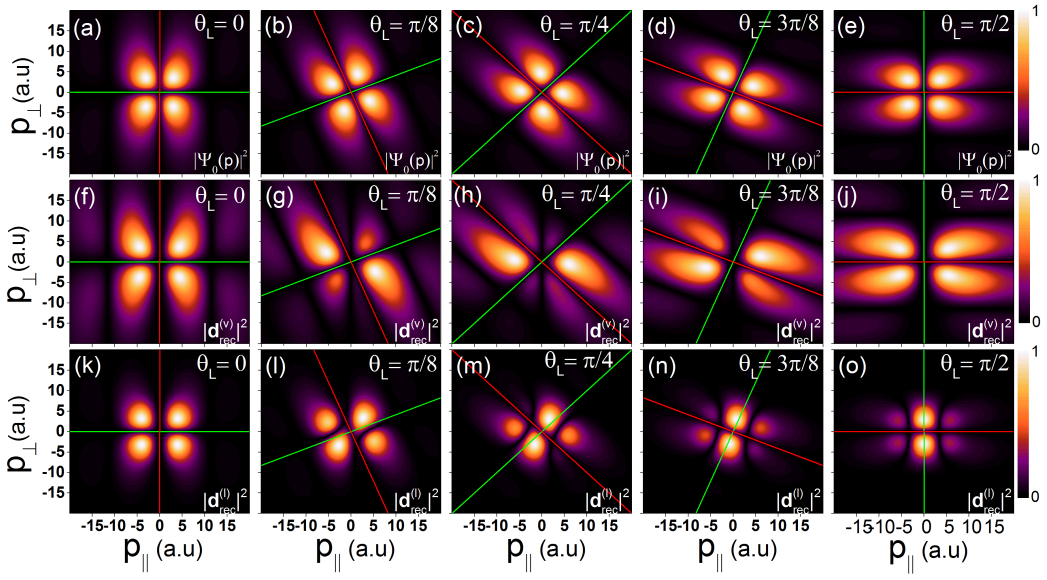

Figure 7.5: In the first, second and third row we compare the probability density $|\Psi_0(\mathbf{p})|^2$ in momentum space with the absolute squares of the dipole matrix elements $d^{(v)}_{\rm rec}(\mathbf{p}\cdot\hat{\epsilon}_{\|})$ and $d^{(l)}_{\rm rec}(\mathbf{p}\cdot\hat{\epsilon}_{\|})$ along the major polarisation axis, respectively, for the HOMO of O_2. The alignment angle θ_L is increased from the left column, $\theta_L = 0$, to the right column $\theta_L = \pi/2$ in increments of $\delta\theta_L = \pi/8$. The HOMO of O_2 is a $1\pi_g$ orbital with I_p =0.441 a.u. and the internuclear separation is $R = 2.28$ a.u. The green and red lines in all the panels indicate the orientation of nodal planes constructed using atomic basis functions at single and different atomic centres, respectively. The quantity in each panel has been normalised by its maximum value.

in which the real parts of the effective shifts $\zeta(t, t')$ are plotted for driving fields of increasing ellipticity. The case considered in the previous panels [Fig. 7.3(a) and (b)], i.e., $\xi = 0.3$, is given by the outer curves. For the long orbit, this shift is positive. Hence, it will displace the suppression caused by the nodal plane towards larger alignment angles [see Fig. 7.3(a)]. A similar argument can relate the negative shift observed for the short orbit to the displacement to the left observed in Fig. 7.3(b). At and beyond the cut-off, the real parts of the shifts vanish. Consequently, the nodal-plane suppression will approach the position obtained for a linearly polarised field. The reason for this is that around the cut-off the electron is expected to return at a crossing of the electric field, i.e., at a crest of the parallel vector potential [see Fig. 7.3(d)]. At such times, both orbits experience a vanishing perpendicular vector potential, which translates into a vanishing shift around the cut-off. Below the cut-off, the short and long orbits are subjected to equal but opposite perpendicular momenta, which increase for decreasing harmonic frequency. Hence, the nodal-plane suppressions are increasingly displaced in opposite directions for each orbit as the harmonic order decreases.

For the suppressions near even multiples of $\theta_L = \pi/2$, the calculated effective shift

does not fit the SFA outcome. The latter is strongly exaggerated for lower harmonics, and even meets the other shifted suppressions near the ionisation threshold (see dot-dashed lines in the picture). We also see that the suppressions are more blurred than those encountered for $\theta_L = (2n+1)\pi/2$.

If, instead, the matrix element $d^{(v)}_{\rm rec}(\mathbf{p}\cdot\hat{\epsilon}_\parallel)$ in the velocity form is used [Eq. (3.25)], the agreement between the SFA and the analytical condition (3.84) improves significantly near $\theta_L = 0, \pi$ and 2π. There is, however, some blurring, if compared with the suppressions observed near odd multiples of $\pi/2$ for the low harmonic ranges. These results can be seen in Fig. 7.4, for the individual contributions of the long and short orbit [panels (a) and (b), respectively], together with the results obtained using their coherent superposition [panel (c)].

These distortions are related to artefacts in the recombination dipole matrix elements, which leads to geometrical features that do not exist in the HOMO. In the present framework, the nodal structures are constructed in two ways. One may either employ nodes in the atomic orbitals at a *single* centre in the molecule, or the sum or subtraction of atomic orbitals at *different* centres within the LCAO approximation. The former type of construction causes the suppressions at $\theta_L = n\pi$, while the latter lead to the suppressions at $\theta_L = (2n+1)\pi/2$. The velocity form of the SFA along the major polarisation axis multiplies the momentum-space wavefunction by $p_\parallel$, while the length form of the SFA takes the partial derivative $\partial_{p_\parallel}\psi_a(\mathbf{p})$ of the atomic momentum wavefunctions used to construct the orbital [see Eq. (7.1)]. Both procedures modify the nodal structures constructed using a single centre. This spurious behaviour becomes evident as the molecule rotates.

This is exemplified in Fig. 7.5, where we display the HOMO probability density $|\Psi_0(\mathbf{p})|^2$ for O_2 in momentum space, together with the absolute squares of the dipole matrix elements $d^{(v)}_{\rm rec}(\mathbf{p}\cdot\hat{\epsilon}_\parallel)$ and $d^{(l)}_{\rm rec}(\mathbf{p}\cdot\hat{\epsilon}_\parallel)$ along the major polarisation axis, for several alignment angles θ_L. For $\theta_L = 0$, the three pictures are similar, with four lobes separated by two orthogonal nodal planes [see first column in the figure]. For $\theta_L \neq 0$, however, this scenario changes, as shown in the remaining columns of the figure. While $|\Psi_0(\mathbf{p})|^2$ does not alter its structure and merely rotates, for the velocity form there is an additional nodal plane at $p_\parallel = 0$. For the length form, the behaviour is more extreme and the node constructed with a single centre begins to warp, split and shift away from the original shape and orientation of $\Psi_0(\mathbf{p})$ indicated by the green lines.

Both structures can be understood by inspecting the two prefactors. In the velocity form, $p_\parallel\psi_a(\mathbf{p})$ implies that there will be a suppression at $p_\parallel = 0$. For $\theta_L = n\pi$, this condition coincides with the nodal plane given by $\tan\theta_L = p_\perp/p_\parallel$, which is obtained by imposing $\psi_a(\mathbf{p}) = 0$. For other angles, however, it leads to the spurious nodal structure. For the length form, the two terms in $\partial_{p_\parallel}\psi_a(\mathbf{p})$ lead, in general, to structures that are

quadratic in $p_{\parallel}$. Specifically, Eq. (7.2) moves the suppression away from the axis $p_{\parallel} = 0$ and the term given by Eq. (7.3) gives the above-mentioned warping. Once more, these spurious effects disappear for $\theta_L = n\pi$. These artefacts do not contribute when using a linearly polarised fields, as the electron's angle of return is always vanishing. This means that linearly polarised fields only probe the $p_{\parallel}$ axis in Fig. 7.5. If the nodal planes are not parallel to this axis, the returning electron will "see" a non-vanishing probability density and no suppression will occur. Hence, linearly polarised fields can only probe the nodal planes at multiples of $\pi/2$, for which the distortions cannot be seen along this axis.

Further, in Fig. 7.5(f) we can see that for $|p_{\parallel} = 0| > 10$ a.u. the velocity form exhibits additional lobes which rotate and warp with the nodal planes as the molecule is rotated from Fig. 7.5(f) to (j). In [151, 152], they explained that these lobes are artificial and are caused by the invalidity of the plane wave approximation for the kinetic energy range of the propagating electrons in HHG [153, 151, 152], an effect that has been observed in tomographical reconstructions of molecules such as N_2 [25, 154, 28].

The length or velocity form of the SFA dipole matrix elements has caused a lot of debate. In the single-active electron, single-active orbital approximation, it is known that the velocity form is superior in predicting structural interference minima, and provides the best agreement with the double-slit physical picture [112]. However, for linearly polarised driving fields the spurious terms introduced by the length form are well understood and easy to eliminate. They are caused by the lack of orthogonality between the bound and continuum states that exists in the SFA [116, 94], and are absent from the start in the expressions used in this paper [see Eq. (3.69)].

The results in Figs. 7.3 to 7.5 tell us that, although for a linearly polarised field the form of the dipole operator may not make much difference, to the nodal suppressions in the HHG spectrum for an elliptically polarised field it does. This is because in this type of field the returning electron can probe dynamics of the wavefunction that would previously be unreachable. This exposes other artefacts in both forms of the SFA dipole, which are more difficult to eliminate. Nonetheless, the velocity form provides better results, if compared to the length form.

7.3 Phase and Field Selection

In Figs. 7.3 and 7.4 the shift of the nodal-plane suppression is quite large, especially for lower harmonics. However, around the cut-off the shift vanishes. Since, however, the long and the short orbit merge at the cut-off, this would be the best region to observe the shift if a coherent superposition of orbits is taken into consideration [1]. Furthermore, if one wishes to observe these shifts experimentally, it would be more convenient if they occurred for the whole harmonic range in the spectrum. In this section we will discuss

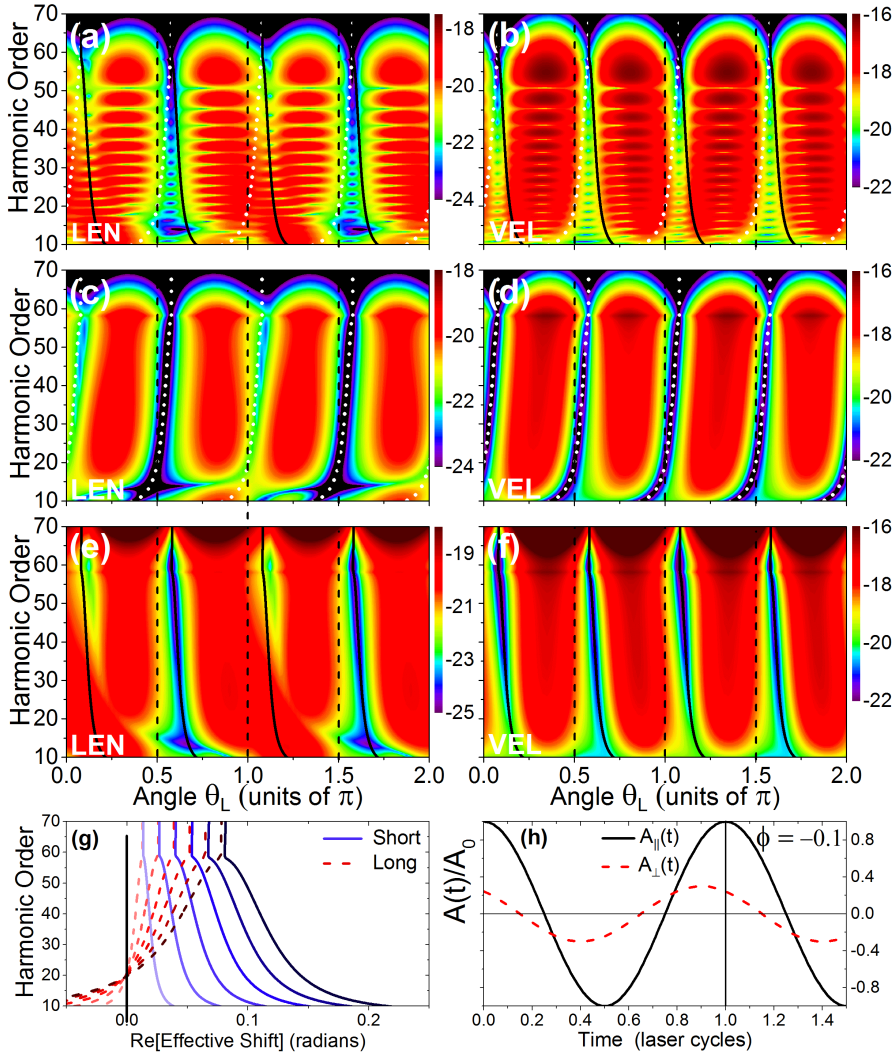

Figure 7.6: In panels (a) to (f), we show $|M(\Omega)|^2$ calculated using the length (first column) and the velocity (second column) forms of the SFA. The first, second and third row have been calculated using the coherent superposition of the dominant orbits [panels (a) and (b)], and the individual contributions of the long [panels (c) and (d)] and short orbits [panels (e) and (f)], respectively. The harmonic yield in these panels is given in a logarithmic scale. The parameters used are the same as in Fig. 7.2, but with a time delay $\phi = -0.1$ between the parallel and perpendicular waves. The black dashed lines indicate the position of the nodal-plane suppressions for a linearly polarised field, whilst the white short dashed and solid black curves give the calculated position of the suppression for the long and short orbit, respectively, for elliptically polarised fields. Panel (g) and (h) shows the same plot as panels (c) and (d) in Fig. 7.3, but using a relative phase of $\phi = -0.1$.

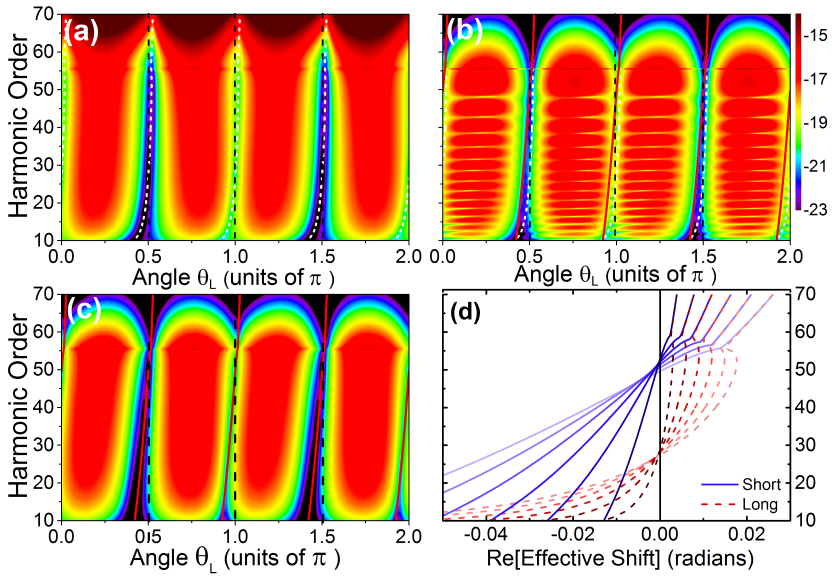

Figure 7.7: In panels (a) to (c), we show the transition probabilities $|M(\Omega)|^2$ along the major polarisation axis as functions of the alignment angle θ_L for O_2 (ionisation potential $I_p = 0.441$ a.u. and internuclear separation $R = 2.28$ a.u.). The parameters used are the same as in Fig. 7.2, but with $n = 2$ for the perpendicular wave, which is in phase ($\phi = 0$) with the parallel component of the laser field. Panels (a) and (c) give the individual contributions from the long and short orbit respectively, whilst (b) shows the result using their coherent superposition. The black dashed lines indicate the positions of the nodal-plane suppressions in the spectrum for a linearly polarised field, whilst the white short dashed and red curves give the calculated modified position of the suppression for the long and short orbit, respectively. The harmonic yield is given in a logarithmic scale. The increase in the harmonic yields after the cut-off observed in panel (a) is related to a breakdown of the standard saddle-point approximation which occurs to the long orbits for this particular phase difference (for details see Ref. [3]). In panel (d) we have the same plotted as Fig. 7.3c, but using the same relative phase, intensity and frequency as in panels (a), (b) and (c) in this figure.

field choices which are favourable to this behaviour.

Since the shifts are strongly dependent on the time delay between the parallel and perpendicular waves, choosing a different relative phase ϕ changes the behaviour of the shift. An example is provided in Fig. 7.6, for which the parallel and perpendicular driving waves have a phase difference of $\phi = -0.1$. In Fig. 7.6, we show the SFA transition probabilities computed for this phase, using the whole dominant pair, the long and the short orbit [first, second and third row, respectively]. For comparison, we include results in the length [panels (a), (c) and (e)] and velocity [panels (b), (d) and (f)] forms of the SFA. In contrast to what has been observed in the previous figures, the shifts are now present for the whole harmonic range, including the cut-off region. Our results indicate that the shift would be easier to observe for the short orbit, as it is much larger in this case. This is convenient for experiments as the short orbit is much easier to

isolate through phase matching [2]. Fig. 7.6(g), in which $\mathrm{Re}[\zeta(t,t')]$ is plotted, is also markedly different from Fig. 7.3(c). For instance, for the long and short orbit, the residual shift at the cut-off is positive. This is due to the fact that $A_\perp(t)$ is non-vanishing and positive at the cut-off return times [see Fig. 7.6(h)]. Once more, we see a better overall agreement between the analytical condition and the velocity form of the SFA. For the coherent superposition of the two orbits [Figs. 7.6(a) and (b)], despite some blurring in the plateau and threshold harmonics, the shift can be seen very clearly at the cut-off. For all nodes, only the velocity form gives the correct shifts [Fig. 7.6(b)].

Again, one should bear in mind, however, that for elliptically polarised fields the recollision probability of the electron decreases as ξ increases, which may lead to low HHG efficiency. For two-colour orthogonal fields, on the other hand, the electron has higher probability of returning to the parent molecule as the strength of the perpendicular field is increased. For this reason, it is useful to compare computations using these two types of field.

In Fig. 7.7, we present transition probabilities $|M(\Omega)|^2$ computed for two-colour fields. We consider a coherent superposition of the two dominant orbits [panel (b)], together with the individual contributions from the long and short orbits [panels (a) and (c), respectively]. We have taken the relative phase $\phi = 0$, which produces fairly large shifts for two-colour fields. The figure shows that the shifts in the nodal-plane suppressions are much smaller than those obtained in the elliptically polarised case. For instance, for $\xi = 0.3$, an elliptical field may lead to shifts up to $\mathrm{Re}[\zeta(t,t')] = 0.25$, while for a two-colour field the effective shift reaches up to $\mathrm{Re}[\zeta(t,t')] = 0.05$. This can be seen by comparing the effective shifts in Fig. 7.7(d) with the elliptical-field examples in Figs. 7.3(c) and 7.6(g). Hence, a two-colour field would be less suitable for finding the shift in experiments, despite the higher probability of return.

7.4 Conclusions

In this chapter, we investigated the effects of using orthogonally polarised fields on the nodal plane suppression in HHG spectra from aligned diatomic molecules. Our results show that, when using such fields, one may infer the angle with which an electron returns to its parent ion from HHG spectra, by relating it to distortions in the nodal-plane suppressions. While for linearly polarised fields these suppressions are well known and occur at fixed alignment angles throughout the spectra, if the fields are orthogonally polarised they are orbit- and harmonic-dependent. They can be controlled by changing the driving-field parameters, such as the relative phase, intensity and frequency ratios between the two orthogonal waves. As a testing ground, we have employed the HOMO of O_2, which exhibits two orthogonal nodal planes and no two-centre interference minimum

for the parameter range of interest, in our computations.

Within our model, the suppressions in the spectra are caused by the recombination dipole matrix element in the SFA. The analytic condition for the shift, given by Eq. (3.84), works well for individual orbits if the nodal planes are constructed using atomic basis functions at different centres, but discrepancies arise for nodal planes in which basis functions at single centres are used. These discrepancies expose limitations in the recombination dipole matrix elements, which are overlooked for linearly polarised fields.

In fact, we show that for specific alignment angles $\theta_L = n\pi/2$ the suppressions in these matrix elements coincide with the nodal planes. However, this is not the complete picture and spurious structures arise for other angles. These effects occur both for the length and the velocity form of the dipole operator. Nonetheless, while for the velocity form they lead to a light blurring around the analytical condition, in the length form they are very extreme and lead to exaggerated distortions. Hence, the length form of the SFA should be avoided when mapping nodal planes using orthogonal fields.

One should note, however, that, because the shifts are orbit dependent, they may be difficult to extract unless either the cut-off region or a particular return event can be singled out. For a coherent superposition of orbits these patterns are blurred as there are many possible return angles. This is a similar situation to that encountered in Chapter 4, in which the angle of return was incorporated in the structural, two-centre interference condition. Following the method set out in Chapter 5, this problem can however be solved using polarisation gating [107] and phase-matching conditions to remove the contributions to the HHG spectrum of one of the dominant trajectories. In particular the short orbit is very convenient for observing these effects, as it phase matches on axis and the HHG signal is strong. The same could be applied to the nodal-plane suppressions, for which there are two main advantages with regard to the shifted two-centre interference condition. First, the distortions caused by the angle of return near nodal planes are in principle easier to identify as the suppressions are stronger. Second, with the right choice of phase difference, this suppression can be shifted across the spectra.

We have also found that elliptically polarised fields provide better conditions for observing the shifts experimentally, in comparison with OTC fields. First, using an elliptically polarised field gives rise to a much larger shift. Second, in chapter 4 we found that using a two-colour orthogonal field caused the shift to flip sign every half cycle. This was because the parallel component $A_{\parallel}(t)$ of the vector potential would change sign every half cycle, but the perpendicular component $A_{\perp}(t)$ would not, causing $\zeta(t, t')$ to change sign. In chapter 5, we avoided this problem by using a few-cycle pulse in which a specific cycle was dominant in the region of interest. For elliptical fields, however, there

is no need to restrict ionisation events to a single half cycle. Hence, any pulse length can be employed. Thus, the present study proposes a way to extract an electron's angle of return using nodal planes as tools, which is valid as long as the single-active electron and orbital approximation holds. This seems to be the case for the plateau, as there is evidence that structural effects are dominant in this region [145, 146].

Part III

Strong field ionisation

Chapter 8

Theoretical background (ATI)

We can derive the transition amplitude for direct ATI within the framework of the SFA using Eq. (2.15) in Chapter 2. The mechanism behind this phenomenon is a transition of an electron from the ground state of an atom, $|\Psi_0(t')\rangle$ into a continuum state $|\Psi_{\mathbf{p}}(t)\rangle$, where p is the momentum of the continuum state. We project the continuum state onto Eq. (2.15) which gives us a transmission amplitude that reads [118, 3, 155, 156, 157]

$$\mathbf{M}_p = \lim_{\substack{t\to\infty \\ t'\to-\infty}} \left[\langle \Psi_{\mathbf{p}}(t)|U_0(t,t')|\Psi_0(t')\rangle - i\int_{t'}^{t} \mathrm{d}t'' \langle \Psi_{\mathbf{p}}(t)|U_V(t,t'')H_I(t'')U_0(t'',t')|\Psi_0(t')\rangle \right], \tag{8.1}$$

The first term vanishes as the ground and continuum states are orthogonal. This leaves us with

$$\mathbf{M}_p = \lim_{t\to\infty} -i\int_{-\infty}^{t} \mathrm{d}t' \langle \Psi_{\mathbf{p}}(t)|U_V(t,t')H_I(t')|\Psi_0(t')\rangle. \tag{8.2}$$

We can approximate the electron in the continuum by the Volkov states $|\Psi^V_{\mathbf{p}}(t)\rangle$, which in the length gauge are given by

$$|\Psi^V_{\mathbf{p}}(t)\rangle = e^{-iS(t)}|\mathbf{p}+\mathbf{A}(t)\rangle, \tag{8.3}$$

where

$$S(t) = \frac{1}{2}\int_{-\infty}^{t} \mathrm{d}t''[\mathbf{p}+\mathbf{A}(t'')]^2. \tag{8.4}$$

Utilizing $|\Psi_0(t)\rangle = e^{-iE_0t}|\Psi_0\rangle$, where E_0 is the bound energy of the state, Eq. (8.2) becomes

$$\mathbf{M}_p = -i\int_{-\infty}^{\infty} \mathrm{d}t' \mathbf{d}_{\mathrm{ion}}(\mathbf{p}+\mathbf{A}(t'))e^{iS(\mathbf{p},t')}, \tag{8.5}$$

where

$$\mathbf{d}_{\mathrm{ion}}(\mathbf{p}+\mathbf{A}(t')) = \langle \mathbf{p}+\mathbf{A}(t')|H_I(t')|\Psi_0\rangle, \tag{8.6}$$

is the ionisation prefactor and

$$S(\mathbf{p}, t') = \frac{1}{2}\int_{t'}^{\infty} \mathrm{d}\tau[\mathbf{p} + \mathbf{A}(\tau)]^2 + E_0 t'. \tag{8.7}$$

is the classical action. Eq. (8.5) is the SFA transition amplitude for direct ATI which describes the ionisation of an electron from the ground state to the continuum via tunnelling. Once in the continuum, its propagation is described by the action $S(t', \mathbf{p})$, where it has an asymptotic momentum $\mathbf{p}$ in the presence of a field with vector potential $\mathbf{A}(t)$.

8.1 Saddle point equations for direct ATI

Analogous to HHG in Chapter 3, in order to solve Eq. (8.5) one can take advantage of the fact that the action oscillates very quickly in comparison to the prefactor [117] and employ the saddle point approximation. This means the stationary points of the semi-classical action can be use to calculate the integral as they make the largest contributions to Eq. (8.5). To do this one must find the values of t' when $\partial S(\mathbf{p}, t')/\partial t' = 0$, which gives the following saddle point equation

$$\frac{[\mathbf{p} + \mathbf{A}(t')]^2}{2} + E_0 = 0. \tag{8.8}$$

Physically, Eq. (8.8) expresses the conservation of energy upon tunnelling ionisation at time t' for the electron. Because tunnelling has no classical counterpart, this equation only has complex solutions. The major contributions to the integral over t' in Eq. (8.5) come from the region around the value of t' for which the action is stationary. Using the saddle point method we can approximate the integral over t' by employing a Taylor expansion of the action around the saddle point, t'_{s},

$$S(\mathbf{p}, t') = S(\mathbf{p}, t'_{\mathrm{s}}) + \frac{\partial S(\mathbf{p}, t'_{\mathrm{s}})}{\partial t'}(t' - t'_{\mathrm{s}}) + \frac{1}{2}\frac{\partial^2 S(\mathbf{p}, t'_{\mathrm{s}})}{\partial t'^2}(t' - t'_{\mathrm{s}})^2 + ... \tag{8.9}$$

Here, orders higher than the second order are ignored and since t'_{s} is a stationary point the first order derivatives of the action vanish. Inserting Eq. (8.9) into Eq. (8.5), the transition amplitude now reads,

$$\mathbf{M}_p \approx \langle \mathbf{p} + \mathbf{A}(t'_{\mathrm{s}})|H_I(t')|\Psi_0\rangle e^{-iS(\mathbf{p},t'_{\mathrm{s}})}\int_{-\infty}^{\infty} \mathrm{d}t' e^{-i\frac{1}{2}(\partial^2 S(\mathbf{p},t'_{\mathrm{s}})/\partial t'^2)(t'-t'_{\mathrm{s}})^2}, \tag{8.10}$$

The last term in Eq. (8.10) has the form of a Gaussian integral and can therefore be

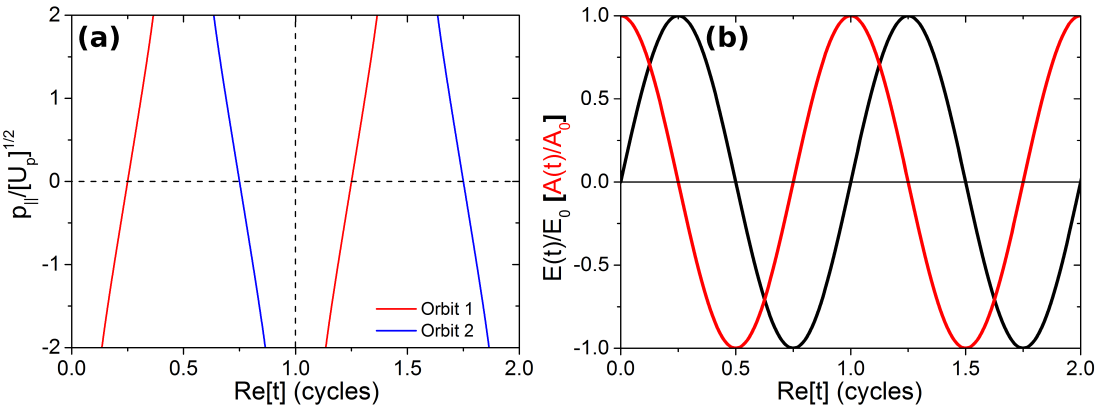

Figure 8.1: Panel (a) shows the real part of the ionisation times and the final momentum $\mathbf{p}$ that the electron acquires while in the continuum when following orbit 1_j (red line) and orbit 2_j (blue line). The end of the first cycle of the laser field is indicated by the horizontal dashed line. Panel (b) shows a schematic representation of two cycles electric field E(t)(black curve) and the vector potential A(t)(red curve) of a monochromatic linearly polarised field.

written in the following way

$$\int_{-\infty}^{\infty} \mathrm{d}t' e^{-i\frac{1}{2}(\partial^2 S(\mathbf{p},t'_\mathrm{s})/\partial t'^2)(t'-t'_\mathrm{s})^2} = \sqrt{\frac{2\pi}{\partial^2 S(\mathbf{p},t'_\mathrm{s})/\partial t'^2}}, \tag{8.11}$$

Inserting this into Eq. (8.10), we can now approximate the transition amplitude as a summation of saddle point solutions,

$$M(\mathbf{p}) \approxeq \sum_\mathrm{s} A_\mathrm{s} e^{S(\mathbf{p},t'_\mathrm{s})}, \tag{8.12}$$

where the classical action $S(\mathbf{p}, t'_\mathrm{s})$ is given by

$$S(\mathbf{p}, t'_\mathrm{s}) = \frac{1}{2}\int_{t'_\mathrm{s}}^{\infty} d\tau [\mathbf{p} + \mathbf{A}(\tau)]^2 + E_0 t'_\mathrm{s}, \tag{8.13}$$

and the prefactor A_s is given by,

$$A_s = \sqrt{\frac{2\pi i}{\partial^2 S(\mathbf{p}, t_\mathrm{s})/\partial t_s^2}} \langle \mathbf{p} + \mathbf{A}(t)|V|\Psi_0\rangle. \tag{8.14}$$

As mentioned in Chapter 3 in the context of HHG, the solutions of the saddle point equation Eq. (8.8) can be associated with classical trajectories of the electron in the laser field. For the ATI mechanism, the electron leaves the vicinity of the parent ion and reaches the detector with a final momentum $\mathbf{p}$. These trajectories ionise around the peak of the electric field and their final momentum is influenced by the amplitude of

the vector potential at the time of ionisation. Re$[t']$ can be interpreted as the trajectory start time when the electron ionises. The imaginary part reflects the quantum nature of these trajectories, for instance, Im$[t']$ can be associated to the width of the barrier the electron tunnels through at the time of ionisation [83, 118]. Importantly, there are two solutions/trajectories per cycle for a given final momentum $\mathbf{p}$. These two trajectories ionise around adjacent peaks of the electric field and are designated orbit 1_j and orbit 2_j, where 1 and 2 refer to the which trajectory ionises first in the cycle and the subscript is an integer referring to which cycle the trajectories ionised from. Fig. 8.1a shows the final momentum $\mathbf{p}$ of orbit $1_{1,2}$ and $2_{1,2}$ against Re$[t']$ while Fig. 8.1b shows the electric field [black] and the vector potential [red] at these times. By comparing panels (a) and (b), we can see that at adjacent peaks in the electric field, these orbits ionise with a vanishing final momentum $p_{||}$. This is because this time the vector potential is $|A_{||}(t)| \simeq 0$. Electrons ionising before or after the peak in the electric field are met with a large vector potential $A(t)$ at the time of ionisation which will give them a large absolute final momentum. The direction of the momentum (negative or positive) will be determined by the sign of the vector potential when the electron ionises.

For the direct ATI mechanism the saddle point solutions are well separated and therefore the SPA is suitable to calculate the transition amplitude given by Eq. (8.12). This is not always the case as saddle point solutions can begin to coalesce for other strong field phenomena such as rescattered ATI and HHG. This problem is addressed in Chapter 3 where we derived the transition amplitude for HHG.

Eq. 8.8 can be written in terms of the $p_{||}$ and $p_{\perp}$,

$$\left[p_{||} + A_{||}(t')\right]^2 + p_{\perp}^2 = -2E_0. \tag{8.15}$$

Eq.(8.15) denotes a circle centred at $(p_{||}, p_{\perp}) = (-A_{||}(t), -A_{\perp}(t))$. For a linearly polarised field this centre will be at $(p_{||}, p_{\perp}) = (0, 0)$ with a complex radius (yield exponentially decays around the centre). Physically, this centre corresponds to the most probable momentum with which the electron may tunnel. This makes sense as electrons with zero parallel and perpendicular momentum ionised at the peak of the electric field, where ionisation is most probable.

8.2 Orthogonally polarised driving fields

We will now assume that the external driving field is orthogonally polarised, i.e., made up of two orthogonal linearly polarised laser fields. This implies that the time dependent electric field $\mathbf{E}(t) = -\mathrm{d}\mathbf{A}(t)/\mathrm{d}t$ and the vector potential $\mathbf{A}(t)$ may be written as

$$\mathbf{E}(t) = E_{\parallel}(t)\hat{\epsilon}_{\parallel} + E_{\perp}(t)\hat{\epsilon}_{\perp}, \tag{8.16}$$

and

$$\mathbf{A}(t) = A_{\parallel}(t)\hat{\epsilon}_{\parallel} + A_{\perp}(t)\hat{\epsilon}_{\perp}, \tag{8.17}$$

where the unit vector along the major and the minor polarisation axes are denoted by $\hat{\epsilon}_{\parallel}$ and $\hat{\epsilon}_{\perp}$, respectively. For this specific case, it is convenient to re-write the action as

$$S(p_{||}, p_{\perp}, t) = -\frac{1}{2}\int_{t'}^{\infty} \mathrm{d}\tau [p_{||} + A_{||}(\tau)]^2 - \frac{1}{2}\int_{t'}^{\infty} \mathrm{d}\tau [p_{\perp} + A_{\perp}(\tau)]^2 + E_0 t', \tag{8.18}$$

and the saddle point equation as

$$\left[p_{||} + A_{||}(t')\right]^2 + \left[p_{\perp} + A_{\perp}(t')\right]^2 = -2E_0. \tag{8.19}$$

Analagous to the linear case above, Eqs.(8.19) also denotes a circle centred at $(p_{||}, p_{\perp}) = (-A_{||}(t), -A_{\perp}(t))$, the centre of which will be determined by the parameters of the orthogonally polarised field used.

Chapter 9

Quantum interference in above-threshold ionisation (ATI)

In recent years, features have been observed in the ATI photo-electron spectra that can not be reproduced using the SFA. The origin of these features, such as a fan like structure in the photo-electron momentum distributions [88, 89, 90, 91, 92], are due to the influence of the Coulomb potential, which is ignored within the frame work of the traditional SFA. In this chapter we perform a direct comparison of the temporal interference patterns arising from electron trajectories ionising at different times within a cycle and from consecutive cycles of the electric field. This comparison is performed using the Strong-Field Approximation, with the motive of using this information to investigate how Coulomb focusing modifies the electron trajectories responsible for the fan-shaped structure in above-threshold ionization in future studies. This study is performed for a helium atomic target using linearly and elliptically polarised driving fields of the form

$$\mathbf{E}(t) = \frac{E_0}{\sqrt{1+\xi^2}} \left[\sin(\omega t)\hat{\epsilon}_{\|} - \xi \cos(\omega t)\hat{\epsilon}_{\perp} \right], \tag{9.1}$$

where ξ is the ellipticity of the laser field which can be set to zero for a linearly polarised field.

9.1 Temporal interference, intra- and inter- cycle

The amplitude $M(\mathbf{p})$ given by Eq. (8.12) in Chapter 8 can be understood as a coherent superposition of the contributions from two trajectories per cycle of the driving field $\mathbf{E}(t)$. These two trajectories are designated orbits 1_j and 2_j, where j refers to the cycle in which the orbits ionised from. In this work we use a continuous monochromatic field described by Eq (9.1) so that all of the cycle are equivalent. These trajectories can ionise

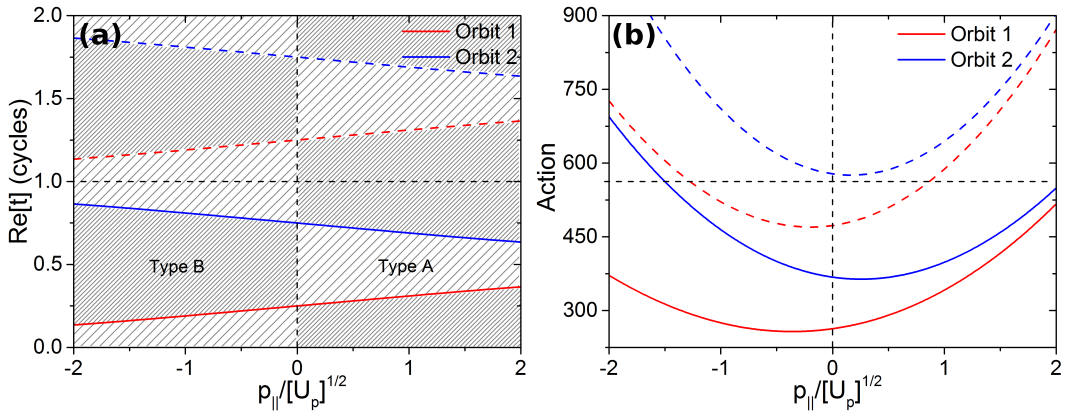

Figure 9.1: Panel (a) shows the real part of the ionisation times and the final momentum the electron acquires while in the continuum. Orbits 2_j and 2_j are indicated by the red and blue curves, respectively. The solid [dashed] curves indicate the orbits have ionised from the first [second] cycle of the field. The regions shaded by well separated linear hatching and labelled "type A" indicate the interfering parts of the orbits where the ionisation time difference between them is less then half a cycle, i.e., $\Delta t < T/2$. The regions shaded by closely spaced linear hatching indicate the interfering parts of the orbits where $\Delta t > T/2$, "type B". Panel (b) shows the value of the action for the orbits shown in panel (a), for a given final momentum that the electron acquires while in the continuum.

with a range of final momenta which depends of the size of the vector potential, $\mathbf{A}(t)$, at the time of ionisation. If orbits 1_j and 2_j ionise at the peak of the electric field, they will feel a vanishing vector potential and will therefore have a vanishing final momentum. Either side of the peak, the vector potential begins to increase in magnitude, but with opposing sign. This causes an increase in the momenta of the ionising electrons in different directions. The contributions to the transition amplitude from these two orbits can constructively or destructively interfere if they have the same final momentum. If we look at the ionisation times within the first cycle in Fig. 9.1a which shows the ionisation times of orbits $1_{1,2}$ (red lines) and $2_{1,2}$ (blue lines) against the corresponding final momentum, we can see for a positive $p_{||}$, orbits 1_1 and 2_2 ionise very close. This time difference, Δt increases as go to negative $p_{||}$. Δt creates a temporal double slit giving rise to interference fringes that get finer or thicker depending on its size. These interference effects were studied by Arbo *et al* in [45], where they factorised the momentum distributions into contributions from two types of interference using the following equation,

$$\frac{\mathrm{d}P^{SP}}{\mathrm{d}\mathbf{p}} = 4\Gamma(\mathbf{p}) \underbrace{\cos^2\left(\frac{\Delta S}{2}\right)}_{F(\mathbf{p})} \underbrace{\left[\frac{\sin(N\bar{S}/2)}{\sin(\bar{S}/2)}\right]}_{B(\mathbf{p})} \tag{9.2}$$

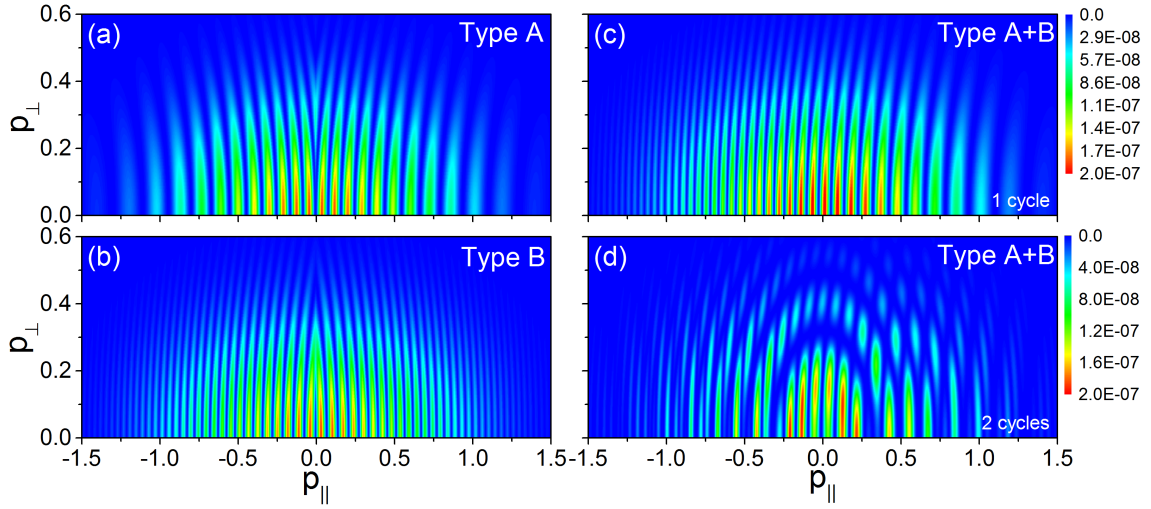

Figure 9.2: Momentum distribution maps for direct ATI from a helium atom in a linearly polarised laser field of intensity $I = 3.8$ W/cm^2 and frequency $\omega = 0.059$ a.u. The ionisation energy for helium is $I_p = 0.92$ a.u. Panel (a) shows type A intra-cycle interference, where the Δt is less than half a cycle and panel (b) shows type B intra-cycle interference where the Δt is greater than half a cycle. In panel (c) we show the complete contributions of orbits 1_1 and 2_1 from the first cycle of the field (see Fig. 9.1a). Panel (d) is the same as panel (c), but includes contributions over 2 cycle of the electric field, i.e., orbits $1_{1,2}$ and $2_{1,2}$.

where $\bar{S}_j = [S(t_j^{(1)}) + S(t_j^{(2)})]/2$ is the average action, where the action $S(t)$ is given by Eq. (8.13), and $\Delta S_j = [S(t_j^{(1)}) - S(t_j^{(2)})]$ is difference in action of the two trajectories released in cycle j where $t_j^{(1)}$ and $t_j^{(2)}$ are the ionisation times for orbits 1 and 2, respectively. $B(\mathbf{p})$ gives us the inter-cycle interference which arises when more then one cycle is considered and consecutive contributions from orbits $1_j^{(1)}$ or $2_j^{(2)}$ interfere leading to the well known ATI peaks [46, 47]. Arbo *et al* describe this "inter-cycle" interference as arising from a diffraction grating in time consisting of N slits [45], where N is the number of cycles of the monochromatic driving field. $F(\tilde{k})$ gives us the intra-cycle interference which arises from interference between orbits 1_j and 2_j within cycle j and leads to a modulation of the ATI spectrum. These modulations are controlled by the phase difference $\Delta S_j = [S(t_j^{(1)}) - S(t_j^{(2)})]$ and contain information about the sub-cycle ionisation dynamics [158].

In [158] they restrict their evaluation of the intra-cycle interference to a time slit $\Delta t_{\text{intra}} = t_j^{(2)} - t_j^{(1)}$ no greater then half a cycle [see Fig. 2a in [158]]. In this work we show that in fact, intra-cycle interference is present where $\Delta t > T/2$ (T = period of the laser) and leads to interference fringes that grow finer as Δt increases. In Fig. 9.1a, the regions where $\Delta t < T/2$ we have shaded the area between the two orbits with a well separated linear hatching. The difference in action ΔS of the orbits interfering across this region is small (see panel (b) of Fig. 9.1) and leads to thick interference fringes that

grow thicker as the ionisation times get closer together and ΔS decreases. For the regions where $\Delta t > T/2$ we have shaded the area between the two orbits with a very fine linear hatching. Interference between orbits across this region leads to finer fringes. This is because the difference in ionisation time and therefore ΔS is larger in this region. An inspections of Fig. 9.1b shows a increase in ΔS from positive $p_{\|}$ to negative $p_{\|}$. We label the intra-interference from across theses regions as "type A" and "type B" interference, respectively. In panel (a) of Fig. 9.2 we reproduce Fig. 2a of [158], which shows the calculated momentum distributions from one cycle of the field. To reproduce this figure we have defined the start our cycle at the peak of the electric field, $t = T/2$, which starts and ends in the middle of the range of ionisation times for orbits 1_1 and 1_2, respectively. Because of this we have had to neglect contributions from orbits $1_{1,2}$ (red line in Fig. 9.1) when the final momentum $p_{\|} < 0$ in the first cycle and $p_{\|} > 0$ in the second cycle. Defining the start of the cycle at the peak of the the electric field means the time slit Δt is always less than $T/2$, therefore only type A interference occurs. This is evident in the large fringe pattern that grows thicker for increasing absolute final momentum. In order to calculate the momentum distributions with only type B interference we must select only the contributions from orbits $1_{1,2}$ and $2_{1,2}$ whose ionisation times are separated by more than half a cycle, $\Delta t > T/2$. Again this means neglecting parts of an orbit 1's contribution to the spectrum. The result is shown in panel (b) of Fig. 9.2 where we can see that the larger Δt leads to finer interference fringes that grow finer as the absolute of the final momentum increases. Although panel (a) and (b) have highlighted the two types of intra-cycle interference, being selective about which part of orbit is allowed to contribute to the momentum distributions is fragmented and in the case of Fig. 2a of [158] meant that type B intra-cycle interference was completely overlooked. In panel (c) we try to avoid this and defined the beginning of our cycle at $t = 0$, which is a crossing in the electric field. In this way we include the full contribution from orbits 1_1 and 2_1, which produces an asymmetrical plot with a gradual transition from finer to thicker interference fringes, as the final momentum of the electron increased from negative $p_{||}$ to positive $p_{||}$. Because we are using a continuous monochromatic wave, plotting the momentum distributions from any subsequent cycle would produce exactly the same plot as panel (c). We can see why this is by inspecting Fig. 9.2, where it shows that for the second cycle, $(1T > \mathrm{Re}[t] > 2T)$, the time slit between the orbits 1_2 and 2_2 for $p_{||} < 0$ is $\Delta t > T/2$, i.e, type B intra interference occurs. For $p_{||} > 0$, type A intra interference occurs. This is exactly what we find for the first cycle. Of course if we define the start of the cycle at $t = T/2$ then the plot will be flipped around $p_{||} = 0$, with all subsequent cycles producing the identical plot.

A coherent superposition of contributions from orbits ionising from the first and second cycle means that in Fig. 9.2d the well known inter-cycle interference rings appear in

the momentum distribution maps (see comparison plot in [158]). This is due interference between orbits 1_1 and 1_2 and orbits 2_1 and 2_2, where the ionisation times are separated by one cycle of the field ($\Delta t = T$). Like panel (c), the momentum distribution map of panel (d) is asymmetrical around $p_{||} = 0$, but unlike panel (c), type A and type B interference is present across the whole momentum distribution. This is because we have taken a coherent superposition of contributions from orbits $1_{1,2}$ and $2_{1,2}$ and thereore cannot avoid introducing some type B interference where $p_{||} > 0$ and type A for $p_{||} < 0$. This is because temporal interference between orbits 2_1 and 1_2 from difference cycles has been introduced. This creates a time slit Δt that get smaller as we go from $+p_{||}$ to $-p_{||}$. This is the opposite of what we find when we consider the two cycles separately. In fact if we calculate the momentum distributions taking an incoherent superposition of the contributions from the two cycle we retrieve the same plot as panel (c) of Fig. 9.2. Despite the mixing, the dominant type of interference will be decided by the amount of interference that occurs when $\Delta t < T/2$ (type A), versus when $\Delta t > T/2$ (type B). For example, in Fig. 9.2 between $p_{||} > 0$ the dominate interference pattern over two cycles is the large fringes arising from type A interference. Within these fringes we see the finer fringe of type B interference. Looking at Fig. 9.1a we can see that within this momentum range there are two region of type A interference and one type B. Therefore type A dominates the pattern. Over many cycles one would expect this dominance to become less significant.

To calculate a symmetrical momentum distribution with an *even* amount of type A and B interference, one needs an *uneven* number of contributions from orbits 1_j or 2_j, or in other words take the coherent superposition of $N + 1/2$ cycles.

9.2 Temporal interference with an elliptically polarised field

Fig. 9.3 shows how the ellipticity of the fundamental driving laser field affects the interference between orbits 1_1 and 2_1. In panel (a) the field is linear ($\xi = 0$), and we can clearly see intra-cycle interference between orbits 1_1 and 2_1 with a transition from type B to type A intra-cycle interference as $p_{||}$ goes from negative to positive. As the ellipticity is increased, we see the momentum distribution widen along the $p_\perp$ axis until there are two completely distinct momentum distributions with vanishing intra-cycle interference fringes in panel (d) where $\xi = 0.29$. The lack of interference fringes is a clue as to what is happening here, which is that the momentum distributions of each orbit have been shifted in opposing directions along the $p_\perp$ axis, until there is no overlap at $\xi = 0.29$. Without the overlap, there is no interference. An explanation for this shift along $p_\perp$ can be found by inspecting Eq. (8.19), which denotes a circle centred at $(p_{||}, p_\perp) = (-A_{||}(t), -A_\perp(t))$. As the ellipticity of the field increases, orbits 1 and 2 are

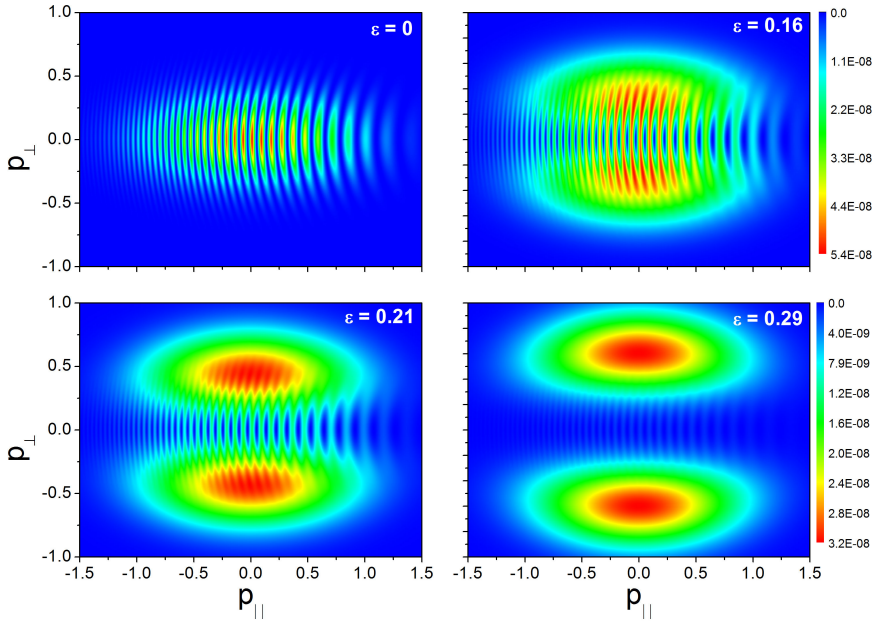

Figure 9.3: Momentum distribution maps for direct ATI from a helium atom in a elliptically polarised laser field described by Eq. (9.1) of intensity $I = 3.8$ W/cm^2 and frequency $\omega = 0.059$ a.u. computed for orbits 1_1 and 2_1. The ionisation energy for helium is $I_p = 0.92$ a.u. The ellipticity of the field is increasing from $\xi = 0$, 0.16, 0.21 to 0.29 from panel (a) to (d).

affected by an equal but opposite perpendicular vector potential $|A_\perp(t)|$. This moves the centre of the circle for each trajectory in opposite directions along the $p_\perp$ axis. This puts the centre for orbit 1 at $(p^1_{||}, p^1_\perp) = (0, -A_\perp(t))$, shifting the momentum distribution down and for orbit 2 at $(p^2_{||}, p^2_\perp) = (0, A_\perp(t))$, shifting it up. This causes the strength of the intra-cycle interference to decrease as the overlap between the two distributions gets smaller and at the $p_\perp$ extremes the two orbits cease to interfere. The pattern and shape of the intra-cycle interference within the overlap remains unaffected by the change in ellipticity, other than a decrease in intensity as the momentum distributions move away from each other. At $\xi = 0.29$ we find that the intra-cycle interference is barely visible between the two distinct momentum distributions of orbits 1_1 and 2_1.

Analogous to Fig. 9.2d, in Fig. 9.4, we consider two cycles of the driving field with contributions from consecutive ionisations from orbits $1_{1,2}$ and $2_{1,2}$. This creates the asymmetrical intra-cycle interference pattern seen most clearly in panel (a) of Fig. 9.4. As the ellipticity is increased, the individual distributions for orbits $1_{1,2}$ and $2_{1,2}$ separate, weakening the intra-cycle interference as we saw in Fig. 9.3. The rings arising from inter-cycle interference dominate. This is due to the fact that the cycles considered are equivalent, hence the centre of the circle denoted by Eq. (8.19) will shift in the same way for orbit 1_1 and orbit 1_2, for example. This means the overlap of the momentum

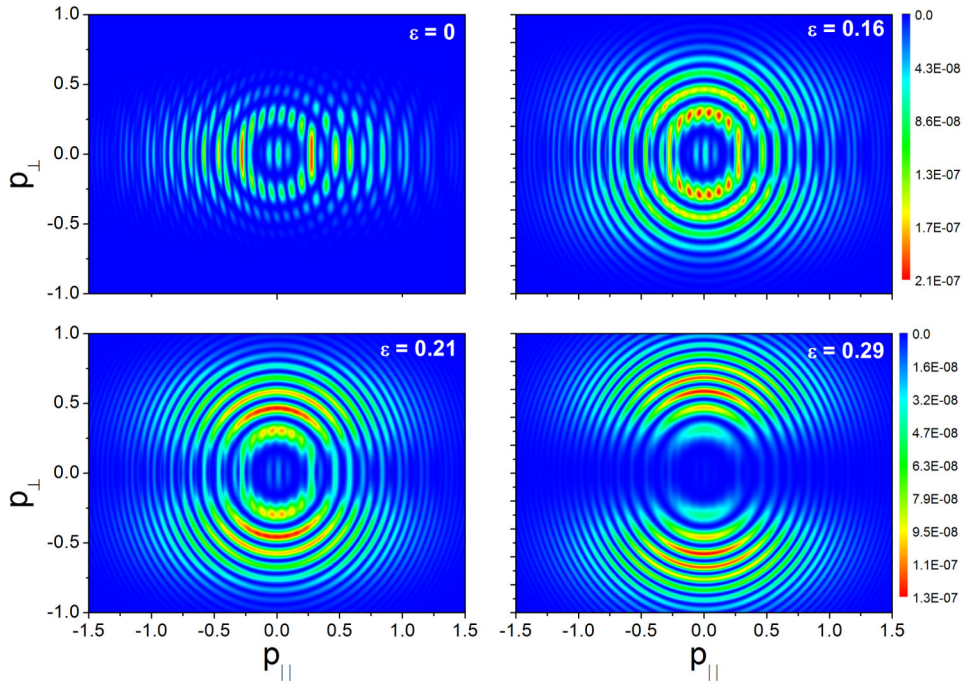

Figure 9.4: Same as Fig. 9.3 except two cycles of the fundamental driving field are considered, i.e., orbits $1_{1,2}$ and $2_{1,2}$ contribute to the momentum maps.

distributions for these orbits remains and therefore so does the inter-cycle interference. For $\xi = 0.29$ intra-cycle interference has almost completely disappeared and only inter-cycle interference is observed.

Experimental results for direct ATI from He conducted by [159], show this splitting in the individual momentum distributions along the $p_\perp$ axis as the ellipticity is increased. It also shows the fan structure disappearing. It is fair to assume then, that the fan like structure is due to modification to the intra-cycle interference as this also disappears as the ellipticity is increased.

Including a third cycle we see that the circle of amplitude around $(p_{||}, p_\perp) = (0, 0)$ has disappeared, and a sub-set of rings begins to appear between the brighter rings. These rings arise from inter-cycle interference of consecutive ionisations from orbits $1_{1,3}$ or orbits $2_{1,3}$, which are separated by two cycles. This creates a larger temporal slit , Δt, which leads to finer interference rings. Panel (a) of Fig. 9.6 is a plot of the momentum distribution of electrons ionising along orbits $1_{1,2,3}$ only. We can see from this figure that these rings indeed arise from inter-cycle interference. In panel (b) we display the coherent superposition of momentum distributions for orbit 1_1 and orbit 1_2. When compared to panel (c), where only orbit 1_1 and orbit 1_3 are considered, we can see that the difference in ionisation time affects the thickness of the rings. These ionisation times are separated

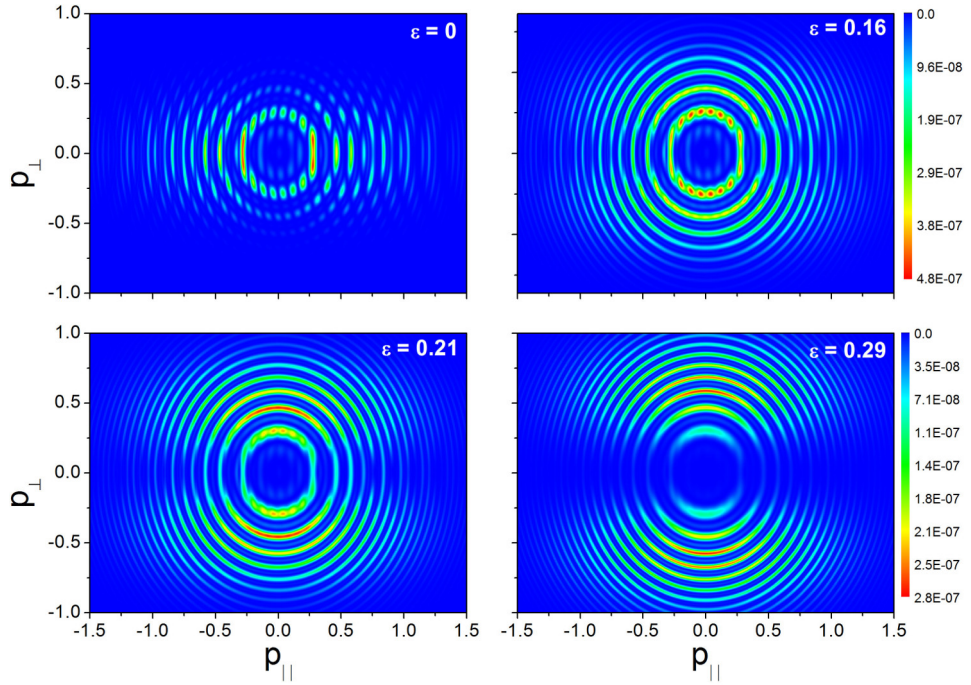

Figure 9.5: Same as Fig. 9.3 except computed for orbits $1_{1,2,3}$ and $2_{1,2,3}$.

by two cycles and we can clearly see that the rings are thinner then those in panel (b). The combination of these two temporal double slit diffraction patterns give rise to the two sets of rings in panel (a).

9.3 RESI and elliptically polarised fields

The investigation of direct ATI in this chapter can give some insight into the momentum distributions of the second electron of recollision-excitation sequential ionisation mechanism (RESI) of non-sequential double ionisation (NSDI). In this mechanism an electron is ionised and rescatters inelastically with it parent ion, imparting some of the energy it has gained whilst propagating in the continuum. This excites a second electron, which after some time tunnel ionises and propagates in the continuum gaining kinetic energy until it reaches the detector. The mechanism describing the ionisation of the second electron is almost exactly like that of direct ATI, except that it ionises from an excited state rather than from the ground state. In fact, studies of the RESI mechanism have used partial momentum maps as a way of understanding the different processes that occur for each of the electrons [160]. When an elliptically polarised field is used this second electron gains a negative or positive perpendicular momentum depending on which orbit it propagates along in the continuum. However, this information is lost once a full momentum map

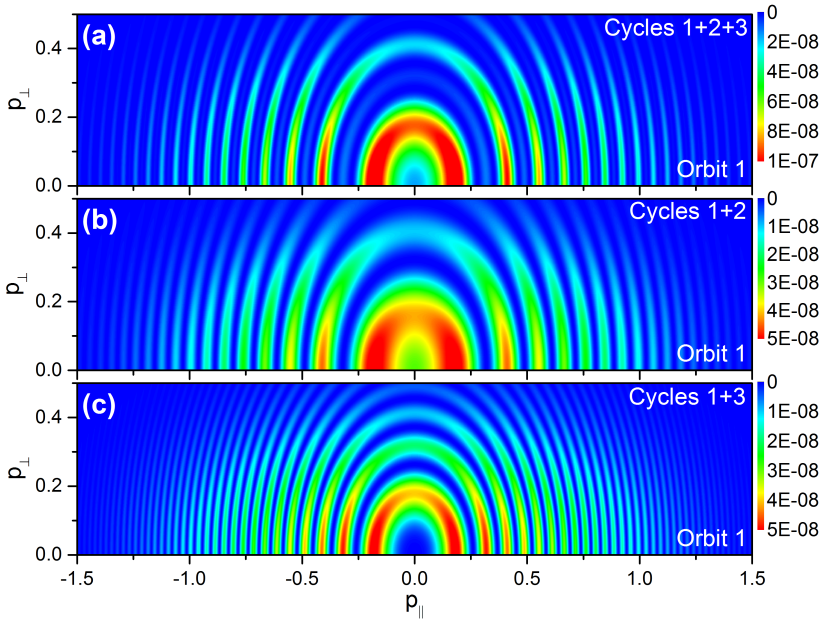

Figure 9.6: Momentum distribution maps for direct ATI from a helium atom, $I_p = 0.92$ a.u., computed for orbits 1_j only. Panel (a) considers ionisations over three cycles of the fundamental driving field, i.e orbits 1_1, 1_2 and 1_3. Panel (b) considers contributions from orbits 1_1 and 1_2 and (c) considers contributions from orbits 1_1 and 1_3. In all three panels the driving laser field is linear, $\xi = 0$, of intensity $I = 3.8$ W/cm^2 and frequency $\omega = 0.059$ a.u.

showing only the parallel final momenta of the first and second electron is calculated.

9.4 Conclusions

In this chapter we analyse the different types of quantum interference in direct ATI. This is done first using linearly polarised fields, where we identify intra-cycle interference type B that is often overlooked or not included in models used to calculate the direct ATI momentum distributions. This intra-cycle interference occurs between electrons ionising at times separated by more than half a cycle of the field and leads to finer fringes in the momentum maps. We also show that the subset of rings in the momentum distribution when more than two cycles are considered in the calculation, arise due to the summation of different combinations of inter-cycle interference patterns from different sized temporal time slits, i.e, interference between orbits whose ionisation times are separated by one cycle and two cycles. By employing an elliptically polarised field we find that the individual momentum distributions of orbit 1 and orbit 2 separate, shifting them in different directions along the perpendicular momentum axis. The reason behind this shift is that the two orbits are exposed to equal but opposite amplitudes of the perpendicularly polarised vector potential field at the time of ionisation. This shift increases as

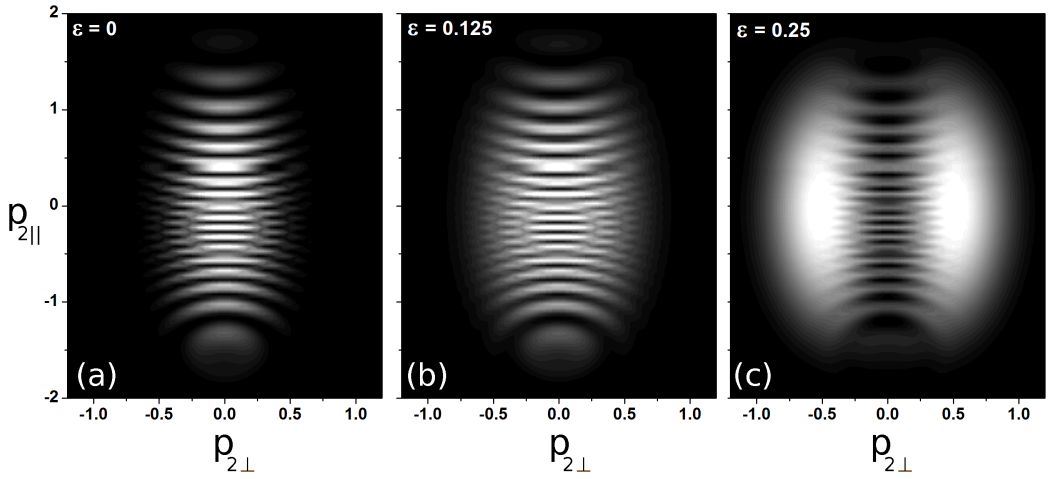

Figure 9.7: Partial momentum distribution maps for the second electron of the RESI mechanism of NSDI ionising from the excited state of the He atom. Only one cycle of the fundamental driving field is considered and the ellipticity is increasing from $\xi = 0$, 0.125 to 0.2 from panel (a) to (c)

the ellipticity is increased. The separating momentum distributions causes a decrease in intra-cycle interference. This is because the overlap between the momentum distributions of orbits 1_j and 2_j decreases, leaving only the "ring" shaped inter-cycle interference. This could explain the loss of the fan-shaped structure in the recent experimental result performed by [159]. Of course, although we can assume with the result so far, that this fan-shaped structure arises from intra-cycle interference, we cannot reproduce the feature using the current model. This is because the SFA neglects the Coulomb potential when the electron is propagating in the continuum. Studies have indicated that the influence of the Coulomb potential may be modifying the trajectories of electrons [79], producing this fan-shaped structure in the continuum. It is therefore important to begin to work towards modifying our model to a Coulomb corrected SFA. This would allow us to more accurately analyse strong field phenomena, giving us the resource to disentangle the effect of the Coulomb potential from those of the driving laser field, in the calculate spectra. This would first be applied to direct ATI as it is the simple mechanism, which once done could be easy applied to the second ionising electron of the RESI mechanism of NSDI. A more long term goal would be to apply Coulomb corrections to HHG and other strong field rescattering phenomena.

Chapter 10

Summary

In this thesis we address temporal and structural interference in high harmonic generation (HHG) from diatomic molecules H_2, Ar_2 and O_2 and direct above threshold ionisation (ATI) from atomic He targets in linearly and orthogonally polarised fields. We have used the strong field approximation to model the phenomena at the single atom and molecule response level and extended this to the macroscopic response level for high harmonic generation, using Maxwell's wave equations, in order to model the propagated high harmonics measured experimentally.

In Part II, we focus on the HHG phenomena and study in detail the added dynamics introduced to the electrons propagation in the continuum when a driving field composed of two orthogonal linearly polarised waves is employed. We show how this added dynamic cause the electron to return at an angle with respects to the major polarisation of the field, modifying the structural two-centre interference patterns in the HHG spectra of diatomic molecules. We then investigate the macroscopic high harmonics response in order to aid the experimental observation of this modification from which one may infer electron angle of return. Additionally in Chapter 7, we investigate how these dynamics can also influence nodal planes suppressions in HHG.

Understanding these effects could prove useful in fields such as molecular imaging and orbital reconstruction [25, 24, 26, 27, 28]. The second orthogonal field introduces an extra degree of freedom, which could also open up these techniques to molecules that are difficult to align [72]. But in order to do so we must disentangle the influence of the field on the HHG spectrum from the structural influence of the target molecule and other influences like the Coulomb potential, which like the driving laser field, can modify the trajectories of the propagating electrons [79]. Therefore a detailed understanding of the electron trajectories in orthogonally polarised fields is required. Moreover, manipulation of the two centre interference minimum can providing a window that can reveal the HHG contributions from lower lying orbitals [78]. Employing orthogonally polarised fields could

be used to tweak the window provided by the interference minimum.

In Chapter 3 we derive a two-centre interference condition, Eq. (3.85), that can be used to predict the position of shifted two centre interference minima in HHG spectra for any orthogonally polarised field. The significance of this condition is that it incorporates an electron's angle of return to its parent molecule. Using this condition it is possible to extract this angle from the shifted minima in HHG spectra.

We test this condition in Chapter 4, at the single-molecule response level using H_2 and Ar_2 as diatomic targets and employing an orthogonally polarised two colour field. We find that the shift in the two centre interference minima and therefore the electron's angle of return are orbit dependent, causing blurring and splitting of the minima within the HHG spectra. This dependence is linked to the difference in the ionisation and recombination times of the "long" or "short" trajectories, which means that the electron "feels" a range of amplitudes and directions of the vector field potential, upon its return. We also find that, when using a $\omega + 2\omega$ orthogonally polarised field, the shift flips sign every half cycle, adding to the blurring caused by the orbit dependence of the shift.

In Chapter 5, we investigate whether it is possible to observe the shifted minimum in macroscopic high-harmonic spectra and ultimately extract the angle with which the electron returns. To date, this shifted two centre interference has not been observed, but experiments have measured that the minimum is lost as the strength of the second orthogonal field is increased [54]. With the work done in Chapter 4, the loss of the minimum can be explained as blurring caused by the sub-cycle variation in the return angle for the electron trajectories. In order to measure a shifted interference minimum experimentally, conditions at the single atom response level and the macroscopic response level, that have been outlined in Chapters 4, 5 and later in Chapter 6, must be considered. In this Chapter we find that through polarisation gating and carefully chosen phase matching conditions, we could suppress the contributions to the HHG spectra from one of the dominant orbits and observe a clear shifted minimum. On top of this we used a few-cycle pulse to show that blurring caused by the change in sign of the shift every half cycle of a could be avoided. This leads us to conclude that the above-mentioned shift could be measured experimentally.

In Chapter 6, we analysed the benefits of using elliptically polarised fields over the OTC fields when trying to observe the shifted minimum. elliptically polarised fields have been found reduce the probability of an electron returning to the parent ion as the ellipticity of the field is increased, leading to drop in HHG yield. We tackled the problem first at the single-molecule response level using H_2 and Ar_2 as targets and found that, unlike the OTC, the shift did not change sign every half cycle. This removes the need to suppressing contribution from other cycles at the macroscopic HHG response level. Furthermore, the shift to the two centre minimum was much larger in general,

which means a lower ellipticity could be employed reducing the detrimental effect to HHG ionisation yield. Using only Ar_2 as a target we modelled the macroscopic HHG response in elliptically polarised fields. We found examples of parameters required to observe the shifted minimum, that indeed agreed with our analysis at a single-molecule response level. More importantly, were able to observe the shifted minimum without the need to suppress one of the dominant orbits, taking advantage of the fact that for certain parameters of the elliptically polarised field there is a point within the plateau of the HHG spectrum where the shifted minima of the "long" and "short" orbit coincide, and therefore the electron has the same, non-vanishing, angle of return. This was not possible for the OTC fields as the shifted minima of the "long" and "short" orbit only meet within the plateau when their angles of return were very close to zero.

In Chapter 7 we show that employing orthogonally polarised fields causes the nodal plane suppressions in HHG spectra to distort. This effect stems from the same electron returning at non-vanishing angles with respect to the major polarisation axis. We investigate this at a single-molecule response level using O_2 as a diatomic target and propose that these distorted suppressions can be employed to infer this angle, with the added benefit of larger shifts and the ability to use the whole harmonic range to do so. Our investigation also led us to understand some important limitations of the different forms of SFA when using orthogonally polarised fields. We found that both the length and velocity forms of the dipole operator give rise to discrepancies for nodal planes constructed using atomic basis functions at single centres. These discrepancies are unnoticeable if linearly polarised fields are used and only come to light using orthogonally polarised fields, because the electron returns at angles to the major polarisation of the fields and is therefore able to probe the spurious structures. Our analysis shows that these discrepancies much more extreme in the length form and suggests avoiding this form in favour of the velocity form of the dipole matrix element, although care is advised.

In Chapter 9, we address quantum interference in direct ATI. This is done first using linearly polarised fields, where we identify different types of intra-cycle interference which are often overlooked or not included in models used to calculate the direct ATI momentum distributions. This intra-cycle interference is between electrons ionising at times separated by more than half a cycle of the field, leading to finer fringes in the momentum maps. We also show how the sub-set of rings in the momentum distribution arises due to combinations of inter-cycle interference patterns from different sized temporal slits. By employing an elliptically polarised field we find that the individual momentum distributions related to ionisation events occurring at subsequent half cycles are shifted in different directions along the perpendicular momentum axis. This shift is due to the different orbits being exposed to equal but opposite amplitudes of the perpendicularly polarised vector potential as ellipticity is increased, at the time of ionisation. This causes

a decrease in intra-cycle interference as the overlap between the momentum distributions decreases, leaving only the "ring" shaped inter-cycle interference. The loss of intra-cycle interference could explain why the fan-shaped structure in experimental ATI momentum distribution maps disappearances as the ellipticity of the field is increased [159]. This fan-shaped structure cannot be reproduced using the SFA. This is because the Coulomb potential is neglected in this model, the effects of which have been shown to modifying electrons trajectories in the continuum [79]. Models that include Coulomb corrections can reproducing this fan-shaped structure [79], therefore it is important to begin to work towards modifying our model to include these corrections. This would allow us to more accurately analyse and calculate the spectra of strong field phenomena, enabling us to disentangle the effect of the Coulomb potential from those of the driving laser field and model experimental results more successfully.

Appendices

Appendix A

List of Abbreviations

AO - Atomic Orbital
AU - Atomic Units
ATI - Above Threshold Ionization
GTO - Gaussian Type Orbital
HHG - High Harmonic Generation
HOMO - Highest Occupied Molecular Orbital
LCAO - Linear Combination of Atomic Orbitals
NSDI - Non Sequential Double Ionisation
OTC - Orthogonally polarised two colour
RESI - Recollision Excitation followed by Subsequent Ionisation
SAE - Single Active Electron
SFA - Strong-Field Approximation
SPA - Saddle-Point Approximation
STO - Slater Type Orbital
TSM - Three Step Model
UA - Uniform Approximation
XUV - Extreme Ultra Violet

Bibliography

[1] T. Das, B. B. Augstein, and C. Figueira de Morisson Faria, "High-order-harmonic generation from diatomic molecules in driving fields with nonvanishing ellipticity: A generalized interference condition," *Phys. Rev. A*, vol. 88, p. 023404, 2013.

[2] T. Das, B. B. Augstein, C. Figueira de Morisson Faria, L. E. Chipperfield, D. J. Hoffmann, and J. P. Marangos, "Extracting an electron's angle of return from shifted interference patterns in macroscopic high-order-harmonic spectra of diatomic molecules," *Phys. Rev. A*, vol. 92, p. 023406, 2015.

[3] C. Figueira de Morisson Faria, H. Schomerus, and W. Becker, "High-order above-threshold ionization: The uniform approximation and the effect of the binding potential," *Phys. Rev. A*, vol. 66, p. 043413, 2002.

[4] J. J. Larsen, K. Hald, N. Bjerre, H. Stapelfeldt, and T. Seideman, "Three dimensional alignment of molecules using elliptically polarized laser fields," *Phys. Rev. Lett.*, vol. 85, pp. 2470–2473, 2000.

[5] S. Rehn, A. Planat-Chrétien, M. Berger, J.-M. Dinten, C. Deumié, and A. da Silva, "Depth probing of diffuse tissues controlled with elliptically polarized light," *Journal of Biomedical Optics*, vol. 18, no. 1, pp. 016007–016007, 2013.

[6] A. da Silva, A. Planat-Chrétien, M. Berger, S. Rehn, J.-M. Dinten, and C. Deumié, "Probing biological tissues in depth with elliptically polarized light," *Proc. SPIE*, vol. 8799, pp. 879904–879904–5, 2013.

[7] B. Kunnen, C. Macdonald, A. Doronin, S. Jacques, M. Eccles, and I. Meglinski, "Application of circularly polarized light for non-invasive diagnosis of cancerous tissues and turbid tissue-like scattering media," *Journal of Biophotonics*, vol. 8, no. 4, pp. 317–323, 2015.

[8] S. Sridhar and A. Da Silva, "Enhanced contrast and depth resolution in polarization imaging using elliptically polarized light," *Journal of Biomedical Optics*, vol. 21, no. 7, p. 071107, 2016.

[9] A. McPherson, G. Gibson, H. Jara, U. Johann, T. S. Luk, I. A. McIntyre, K. Boyer, and C. K. Rhodes, "Studies of multiphoton production of vacuum-ultraviolet radiation in the rare gases," *J. Opt. Soc. Am. B*, vol. 4, no. 4, pp. 595–601, 1987.

[10] M. Ferray, A. L'Huillier, F. Li, L. Lompré, G. Mainfray, and C. Manus, "Multiple-harmonic conversion of 1064nm radiation in rare gases," *J. Phys. B*, vol. 21, p. L31, 1988.

[11] B. Walker, B. Sheehy, L. F. DiMauro, P. Agostini, K. J. Schafer, and K. C. Kulander, "Precision measurement of strong field double ionization of helium," *Phys. Rev. Lett.*, vol. 73, pp. 1227–1230, 1994.

[12] D. N. Fittinghoff, P. R. Bolton, B. Chang, and K. C. Kulander, "Observation of nonsequential double ionization of helium with optical tunneling," *Phys. Rev. Lett.*, vol. 69, pp. 2642–2645, 1992.

[13] P. B. Corkum, "Plasma perspective on strong field multiphoton ionization," *Phys. Rev. Lett.*, vol. 71, pp. 1994–1997, 1993.

[14] P. B. Corkum, N. H. Burnett, and M. Y. Ivanov, "Subfemtosecond pulses," *Opt. Lett.*, vol. 19, no. 22, pp. 1870–1872, 1994.

[15] M. Ivanov, P. B. Corkum, T. Zuo, and A. Bandrauk, "Routes to control of intense-field atomic polarizability," *Phys. Rev. Lett.*, vol. 74, pp. 2933–2936, 1995.

[16] P. Antoine, B. Piraux, D. B. Milošević, and M. Gajda, "Generation of ultrashort pulses of harmonics," *Phys. Rev. A*, vol. 54, pp. R1761–R1764, 1996.

[17] Z. Chang, "Single attosecond pulse and XUV supercontinuum in the high-order harmonic plateau," *Phys. Rev. A*, vol. 70, p. 043802, 2004.

[18] I. J. Sola, E. Mével, L. Elouga, E. Constant, V. Strelkov, L. Poletto, P. Villoresi, E. Benedetti, J.-P. Caumes, S. Stagira, C. Vozzi, G. Sansone and M. Nisoli, "Controlling attosecond electron dynamics by phase-stabilized polarization gating," *Nature Phys.*, vol. 2, p. 319, 2006.

[19] G. Sansone, E. Benedetti, F. Calegari, C. Vozzi, L. Avaldi, R. Flammini, L. Poletto, P. Villoresi, C. Altucci, R. Velotta, S. Stagira, S. De Silvestri and M. Nisoli, "Isolated single-cycle attosecond pulses," *Science*, vol. 314, p. 443, 2006.

[20] M. Hentschel, R. Kienberger, Ch. Spielmann, G. A. Reider, N. Milosevic, T. Brabec, P. Corkum, U. Heinzmann, M. Drescher and F. Krausz, "Attosecond metrology," *Nature*, vol. 414, pp. 509–513, 2001.

[21] R. Kienberger, E. Goulielmakis, M. Uiberacker, A. Baltuska, V. Yakovlev, F. Bammer, A. Scrinzi, Th. Westerwalbesloh, U. Kleineberg, U. Heinzmann, M. Drescher and F. Krausz, "Atomic transient recorder," *Nature*, vol. 427, pp. 817–821, 2004.

[22] I. P. Christov, M. M. Murnane, and H. C. Kapteyn, "High-harmonic generation of attosecond pulses in the "single-cycle" regime," *Phys. Rev. Lett.*, vol. 78, pp. 1251–1254, 1997.

[23] M. Kitzler, X. Xie, A. Scrinzi, and A. Baltuska, "Optical attosecond mapping by polarization selective detection," *Phys. Rev. A*, vol. 76, p. 011801, 2007.

[24] D. Shafir, Y. Mairesse, D. M. Villeneuve, P. B. Corkum and N. Dudovich, "Atomic wavefunctions probed through strong-field light-matter interaction," *Nature Phys.*, vol. 5, p. 412, 2009.

[25] J. Itatani, J. Levesque, D. Zeidler, H. Niikura, H. Pépin, J. C. Kieffer, P. B. Corkum and D. M. Villeneuve, "Tomographic imaging of molecular orbitals," *Nature*, vol. 432, p. 867, 2004.

[26] C. Vozzi, M. Negro, F. Calegari, G. Sansone, M. Nisoli, S. D. Silvestri, and S. Stagira, "Generalized molecular orbital tomography," *Nature*, vol. 7, pp. 822–826, 2011.

[27] Y. J. Chen, L. B. Fu, and J. Liu, "Asymmetric molecular imaging through decoding odd-even high-order harmonics," *Phys. Rev. Lett.*, vol. 111, p. 073902, 2013.

[28] M. Qin, X. Zhu, Q. Zhang, and P. Lu, "Tomographic imaging of asymmetric molecular orbitals with a two-color multicycle laser field," *Optics Letters*, vol. 37, p. 5208, 2012.

[29] M. Kitzler and M. Lezius, "Spatial control of recollision wave packets with attosecond precision," *Phys. Rev. Lett.*, vol. 95, p. 253001, 2005.

[30] I. J. Kim, C. M. Kim, H. T. Kim, G. H. Lee, Y. S. Lee, J. Y. Park, D. J. Cho, and C. H. Nam, "Highly efficient high-harmonic generation in an orthogonally polarized two-color laser field," *Phys. Rev. Lett.*, vol. 94, p. 243901, 2005.

[31] L. Brugnera, F. Frank, D. J. Hoffmann, R. Torres, T. Siegel, J. G. Underwood, E. Springate, C. Froud, E. I. C. Turcu, J. W. G. Tisch, and J. P. Marangos, "Enhancement of high harmonics generated by field steering of electrons in a two-color orthogonally polarized laser field," *Opt. Lett.*, vol. 35, no. 23, pp. 3994–3996, 2010.

[32] L. Brugnera, D. J. Hoffmann, T. Siegel, F. Frank, A. Zaïr, J. W. G. Tisch, and J. P. Marangos, "Trajectory selection in high harmonic generation by controlling the

phase between orthogonal two-color fields," *Phys. Rev. Lett.*, vol. 107, p. 153902, 2011.

[33] Y. Zhou, C. Huang, A. Tong, Q. Liao, and P. Lu, "Correlated electron dynamics in nonsequential double ionization by orthogonal two-color laser pulses," *Opt. Express*, vol. 19, no. 3, pp. 2301–2308, 2011.

[34] P. Eckle, M. Smolarski, P. Schlup, J. Biegert, A. Staudte, M. Schoffler, H. G. Muller, R. Dorner, and U. Keller, "Attosecond angular streaking," *Nat. Phys*, vol. 4, p. 565, 2008.

[35] S. P. Goreslavski, G. G. Paulus, S. V. Popruzhenko, and N. I. Shvetsov-Shilovski, "Coulomb asymmetry in above-threshold ionization," *Phys. Rev. Lett.*, vol. 93, p. 233002, 2004.

[36] M. Busuladžić, A. Gazibegović-Busuladžić, and D. B. Milošević, "Strong-field approximation for ionization of a diatomic molecule by a strong laser field. iii. high-order above-threshold ionization by an elliptically polarized field," *Phys. Rev. A*, vol. 80, p. 013420, 2009.

[37] A. Staudte, S. Patchkovskii, D. Pavičić, H. Akagi, O. Smirnova, D. Zeidler, M. Meckel, D. M. Villeneuve, R. Dörner, M. Y. Ivanov, and P. B. Corkum, "Angular tunneling ionization probability of fixed-in-space H_2 molecules in intense laser pulses," *Phys. Rev. Lett.*, vol. 102, p. 033004, 2009.

[38] G. G. Paulus, F. Zacher, H. Walther, A. Lohr, W. Becker, and M. Kleber, "Above-threshold ionization by an elliptically polarized field: Quantum tunneling interferences and classical dodging," *Phys. Rev. Lett.*, vol. 80, pp. 484–487, 1998.

[39] X. Lai, C. Wang, Y. Chen, Z. Hu, W. Quan, X. Liu, J. Chen, Y. Cheng, Z. Xu, and W. Becker, "Elliptical polarization favors long quantum orbits in high-order above-threshold ionization of noble gases," *Phys. Rev. Lett.*, vol. 110, p. 043002, 2013.

[40] M. Lewenstein, P. Salières, and A. L'Huillier, "Phase of the atomic polarization in high-order harmonic generation," *Phys. Rev. A*, vol. 52, pp. 4747–4754, 1995.

[41] P. Salières, B. Carré, L. Le Déroff, F. Grasbon, G. G. Paulus, H. Walther, R. Kopold, W. Becker, D. B. Milošević, A. Sanpera, and M. Lewenstein, "Feynman's path-integral approach for intense-laser-atom interactions," *Science*, vol. 292, no. 5518, pp. 902–905, 2001.

[42] R. Kopold, D. B. Milošević, and W. Becker, "Rescattering processes for elliptical polarization: A quantum trajectory analysis," *Phys. Rev. Lett.*, vol. 84, pp. 3831–3834, 2000.

[43] G. G. Paulus, F. Grasbon, A. Dreischuh, H. Walther, R. Kopold, and W. Becker, "Above-threshold ionization by an elliptically polarized field: Interplay between electronic quantum trajectories," *Phys. Rev. Lett.*, vol. 84, pp. 3791–3794, 2000.

[44] A. Zaïr, M. Holler, A. Guandalini, F. Schapper, J. Biegert, L. Gallmann, U. Keller, A. S. Wyatt, A. Monmayrant, I. A. Walmsley, E. Cormier, T. Auguste, J. P. Caumes, and P. Salières, "Quantum path interferences in high-order harmonic generation," *Phys. Rev. Lett.*, vol. 100, p. 143902, 2008.

[45] D. G. Arbó, K. L. Ishikawa, K. Schiessl, E. Persson, and J. Burgdörfer, "Diffraction at a time grating in above-threshold ionization: The influence of the Coulomb potential," *Phys. Rev. A*, vol. 82, p. 043426, 2010.

[46] P. Agostini, F. Fabre, G. Mainfray, G. Petite, and N. K. Rahman, "Free-free transitions following six-photon ionization of xenon atoms," *Phys. Rev. Lett.*, vol. 42, pp. 1127–1130, 1979.

[47] M. Protopapas, D. G. Lappas, and P. L. Knight, "Strong field ionization in arbitrary laser polarizations," *Phys. Rev. Lett.*, vol. 79, pp. 4550–4553, 1997.

[48] B. K. McFarland, J. P. Farrell, P. H. Bucksbaum and M. Gühr *Science*, vol. 322, p. 1232, 2008.

[49] N. Hay, R. Velotta, M. Lein, R. de Nalda, E. Heesel, M. Castillejo, and J. P. Marangos, "High-order harmonic generation in laser-aligned molecules," *Phys. Rev. A*, vol. 65, p. 053805, 2002.

[50] S. Baker, J. Robinson, M. Lein, C. Chirilă, R. Torres, H. Bandulet, D. Comtois, J. Kieffer, D. Villeneuve, J. Tisch, and J. Marangos, "Dynamic two-center interference in high-order harmonic generation from molecules with attosecond nuclear motion," *Phys. Rev. Lett*, vol. 101, p. 053901, 2008.

[51] T. Kanai, S. Minemoto, and S. Sakai, "Quantum interferenece during high-order harmonic generation from aligned molecules," *Nature*, vol. 435, p. 470, 2005.

[52] M. Okunishi, R. Itaya, K. Shimada, G. Prümper, K. Ueda, M. Busuladžić, A. Gazibegović-Busuladžić, D. B. Milošević, and W. Beckers, "Two-source double-slit interference in angle-resolved high-energy above-threshold ionization spectra of diatoms," *Journal of Physics: Conference Series*, vol. 194, no. 3, p. 032048, 2009.

[53] M. Lein, R. Velotta, J. P. Marangos, and P. L. Knight, "Interference effects in high-order harmonic generation with molecules," *Phys. Rev. A*, vol. 66, p. 023805, 2002.

[54] C. Vozzi, F. Calegari, E. Benedetti, J. Caumes, G. Sansone, S. Stagira, M. Nisoli, R. Torres, E. Heesel, N. Kajumba, J. Marangos, C.Altucci, and R. Velotta, "Controlling two-center interference in molecular high harmonic generation," *Phys. Rev. Lett.*, vol. 95, p. 153902, 2005.

[55] B. Zimmermann, M. Lein, and J. M. Rost, "Analysis of recombination in high-order harmonic generation in molecules," *Phys. Rev. A*, vol. 71, p. 033401, 2005.

[56] O. Smirnova, Y. Mairesse, S. Patchkovskii, N. Dudovich, D. Villeneuve, P. Corkum and M.Y. Ivanov, "High harmonic interferometry of multi-electron dynamics in molecules," *Nature*, vol. 460, p. 972, 2009.

[57] S. Odžak and D. B. Milošević, "Interference effects in high-order harmonic generation by homonuclear diatomic molecules," *Phys. Rev. A*, vol. 79, p. 023414, 2009.

[58] B. B. Augstein and C. Figueira de Morisson Faria, "Influence of asymetry and nodal structures on high-order harmonic generation in heteronuclear molecules," *J. Phys. B*, vol. 44, p. 055601, 2011.

[59] C. B. Madsen and L. B. Madsen, "High-order harmonic generation from arbitrarily oriented diatomic molecules including nuclear motion and field-free alignment," *Phys. Rev. A*, vol. 74, p. 023403, 2006.

[60] A. D. Bandrauk, S. Chelkowski, S. Kawai, and H. Lu, "Effect of nuclear motion on molecular high-order harmonics and on generation of attosecond pulses in intense laser pulses," *Phys. Rev. Lett.*, vol. 101, p. 153901, 2008.

[61] A. D. Bandrauk, S. Chelkowski, and H. Lu, "Signatures of nuclear motion in molecular high-order harmonics and in the generation of attosecond pulse trains by ultrashort intense laser pulses," *Journal of Physics B: Atomic, Molecular and Optical Physics*, vol. 42, no. 7, p. 075602, 2009.

[62] M. Lein, "Antibonding molecular orbitals under the influence of elliptically polarized intense light," *J. Phys. B*, vol. 36, p. L155, 2003.

[63] O. Smirnova, S. Patchkovskii, Y. Mairesse, N. Dudovich, D. Villeneuve, P. Corkum and M. Yu. Ivanov, "Attosecond circular dichroism spectroscopy of polyatomic molecules," *Phys. Rev. Lett.*, vol. 102, p. 063601, 2009.

[64] A. Etches, C. Madsen, and L. B. Madsen, "Inducing elliptically polarized high-order harmonics from aligned molecules with linearly polarized femtosecond pulses," *Phys. Rev. A*, vol. 81, p. 013409, 2010.

[65] S. Odžak and D. Milošević, "Ellipticity and the offset angle of high harmonics generated by homonuclear diatomic molecules," *J. Phys. B*, vol. 44, p. 125602, 2011.

[66] S. Odžak and D. B. Milošević, "Role of ellipticity in high-order harmonic generation by homonuclear diatomic molecules," *Phys. Rev. A*, vol. 82, p. 023412, 2010.

[67] M. Busuladžić, A. Gazibegović, D. Milošević, and W. Becker, "Strong-field approximation for ionization of a diatomic molecule by a strong laser field. ii. the role of electron rescattering off the molecular centers," *Phys. Rev. A*, vol. 78, p. 033412, 2008.

[68] X. Lai and C. Figueira de Morisson Faria, "Temporal and spatial interference in molecular above-threshold ionization with elliptically polarized fields," *Phys. Rev. A*, vol. 88, p. 013406, 2013.

[69] C. Figueira de Morisson Faria and B. B. Augstein, "Molecular high-order harmonic generation with more than one active electron: Quantum-interference effects," *Phys. Rev. A.*, vol. 81, p. 043409, 2010.

[70] O. Smirnova, S. Patchkovskii, Y. Mairesse, N. Dudovich, and M. Y. Ivanov, "Strong-field control and spectroscopy of attosecond electron-hole dynamics in molecules," *Proceedings of the National Academy of Sciences*, vol. 106, no. 39, pp. 16556–16561, 2009.

[71] Y. Mairesse, J. Higuet, N. Dudovich, D. Shafir, B. Fabre, E. Mével, E. Constant, S. Patchkovskii, Z. Walters, M. Y. Ivanov, and O. Smirnova, "High harmonic spectroscopy of multichannel dynamics in strong-field ionization," *Phys. Rev. Lett.*, vol. 104, p. 213601, 2010.

[72] M. V. Frolov, N. L. Manakiov, T. S. Sarantseva, and A. F. Starace, "High-order-harmonic-generation spectroscopy with elliptically polariszed laser fields," *Phys. Rev. A.*, vol. 86, p. 063406, 2012.

[73] T. Zuo, A. Bandrauk, and P. Corkum, "Laser-induced electron diffraction: a new tool for probing ultrafast molecular dynamics," *Chemical Physics Letters*, vol. 259, no. 3âĂŞ4, pp. 313 – 320, 1996.

[74] H. Ihee, V. A. Lobastov, U. M. Gomez, B. M. Goodson, R. Srinivasan, C.-Y. Ruan, and A. H. Zewail, "Direct imaging of transient molecular structures with ultrafast diffraction," *Science*, vol. 291, no. 5503, pp. 458–462, 2001.

[75] B. J. Siwick, J. R. Dwyer, R. E. Jordan, and R. J. D. Miller, "An atomic-level view of melting using femtosecond electron diffraction," *Science*, vol. 302, no. 5649, pp. 1382–1385, 2003.

[76] H. Niikura, F. Legare, R. Hasbani, A. D. Bandrauk, M. Y. Ivanov, D. M. Villeneuve, and P. B. Corkum, "Sub-laser-cycle electron pulses for probing molecular dynamics," *Nature*, vol. 417, p. 917, 2002.

[77] C. Yu, H.Wei, X. Wang, A. Le, R. Lu, and C. D. Lin, "Reconstruction of two-dimensional molecular structure with laser-induced electron diffraction from laser-aligned polyatomic molecules," *Nature*, vol. 5, p. 15753, 2015.

[78] R. Torres, T. Siegel, L. Brugnera, I. Procino, J. G. Underwood, C. Altucci, R. Velotta, E. Springate, C. Froud, I. C. E. Turcu, S. Patchkovskii, M. Y. Ivanov, O. Smirnova, and J. P. Marangos, "Revealing molecular structure and dynamics through high-order harmonic generation driven by mid-ir fields," *Phys. Rev. A*, vol. 81, p. 051802, 2010.

[79] Lai, X.-Y. and Poli, C. and Schomerus, H. and Figueira de Morisson Faria, C., "Influence of the Coulomb potential on above-threshold ionization: A quantum-orbit analysis beyond the strong-field approximation," *Phys. Rev. A*, vol. 92, p. 043407, 2015.

[80] J. S. Parker, B. J. S. Doherty, K. T. Taylor, K. D. Schultz, C. I. Blaga, and L. F. DiMauro, "High-energy cutoff in the spectrum of strong-field nonsequential double ionization," *Phys. Rev. Lett.*, vol. 96, p. 133001, 2006.

[81] J. S. Parker, B. J. S. Doherty, K. J. Meharg, and K. T. Taylor, "Time delay between singly and doubly ionizing wavepackets in laser-driven helium," *Journal of Physics B: Atomic, Molecular and Optical Physics*, vol. 36, no. 21, p. L393, 2003.

[82] G. S. J. Armstrong, J. S. Parker, and K. T. Taylor, "Double-electron above-threshold ionization resonances as interference phenomena," *Journal of Physics: Conference Series*, vol. 388, no. 3, p. 032057, 2012.

[83] M. Lewenstein, Ph. Balcou, M. Yu. Ivanov, A. L'Huillier and P. B. Corkum, "Theory of high-harmonic generation by low-frequency laser fields," *Phys. Rev. A.*, vol. 49, p. 2117, 1994.

[84] D. M. Volkov, "On a class of solutions of the dirac equation," *Z. Phys.*, p. 250, 1935.

[85] J. B. Bertrand, H. J. Wörner, P. Hockett, D. M. Villeneuve, and P. B. Corkum, "Revealing the cooper minimum of N_2 by molecular frame high-harmonic spectroscopy," *Phys. Rev. Lett.*, vol. 109, p. 143001, 2012.

[86] Y. Mairesse, J. Levesque, N. Dudovich, P. Corkum, and D. Villeneuve, "High harmonic generation from aligned molecules - amplitude and polarization," *Journal of Modern Optics*, vol. 55, no. 16, pp. 2591–2602, 2008.

[87] M. D. Śpiewanowski, A. Etches, and L. B. Madsen, "High-order-harmonic generation from field-distorted orbitals," *Phys. Rev. A*, vol. 87, p. 043424, 2013.

[88] A. Rudenko, K. Zrost, C. D. Schröter, V. L. B. de Jesus, B. Feuerstein, R. Moshammer, and J. Ullrich, "Resonant structures in the low-energy electron continuum for single ionization of atoms in the tunnelling regime," *Journal of Physics B: Atomic, Molecular and Optical Physics*, vol. 37, no. 24, p. L407, 2004.

[89] Z. Chen, T. Morishita, A.-T. Le, M. Wickenhauser, X. M. Tong, and C. D. Lin, "Analysis of two-dimensional photoelectron momentum spectra and the effect of the long-range Coulomb potential in single ionization of atoms by intense lasers," *Phys. Rev. A*, vol. 74, p. 053405, 2006.

[90] D. G. Arbó, S. Yoshida, E. Persson, K. I. Dimitriou, and J. Burgdörfer, "Interference oscillations in the angular distribution of laser-ionized electrons near ionization threshold," *Phys. Rev. Lett.*, vol. 96, p. 143003, 2006.

[91] D. G. Arbó, K. I. Dimitriou, E. Persson, and J. Burgdörfer, "Sub-Poissonian angular momentum distribution near threshold in atomic ionization by short laser pulses," *Phys. Rev. A*, vol. 78, p. 013406, 2008.

[92] T.-M. Yan and D. Bauer, "Sub-barrier Coulomb effects on the interference pattern in tunneling-ionization photoelectron spectra," *Phys. Rev. A*, vol. 86, p. 053403, 2012.

[93] C. Chirilă and M. Lein, "Strong-field approximation for harmonic generation in diatomic molecules," *Phys. Rev. A*, vol. 73, p. 023410, 2006.

[94] C. Figueira de Morisson Faria, "High-order harmonic generation in diatomic molecules: A quantum-orbit analysis of the interference patterns," *Phys. Rev. A*, vol. 76, p. 043407, 2007.

[95] Y. J. Chen and B. Hu, "Strong-field approximation for diatomic molecules: Comparison between the length gauge and the velocity gauge," *Phys. Rev. A*, vol. 80, p. 033408, 2009.

[96] R. Torres, N. Kajumba, J. G. Underwood, J. S. Robinson, S. Baker, J. W. G. Tisch, R. de Nalda, W. A. Bryan, R. Velotta, C. Altucci, I. C. E. Turcu, and J. P. Marangos, "Probing orbital structure of polyatomic molecules by high-order harmonic generation," *Phys. Rev. Lett.*, vol. 98, p. 203007, 2007.

[97] R. Kopold, W. Becker, and M. Kleber, "Model calculations of high-harmonic generation in molecular ions," *Phys. Rev. A*, vol. 58, p. 4022, 1998.

[98] C. B. Madsen and L. B. Madsen, "Theoretical studies of high-order harmonic generation: Effects of symmetry, degeneracy, and orientation," *Phys. Rev. A*, vol. 76, p. 043419, 2007.

[99] B. B. Augstein and C. Figueira de Morisson Faria, "Multi-electron corrections in molecular high harmonic generation for different formulations of the strong-field approximation," *J. Mod. Opt.*, vol. 58, p. 1173, 2011.

[100] A. Etches and L. B. Madsen, "Extending the strong-field approximation of high-order harmonic generation to polar molecules: gating mechanisms and extension of the harmonic cutoff," *J. Phys. B*, vol. 43, p. 155602, 2010.

[101] M. B. Gaarde, J. L. Tate, and K. J. Schafer, "Macroscopic aspects of attosecond pulse generation," *Journal of Physics B: Atomic, Molecular and Optical Physics*, vol. 41, no. 13, p. 132001, 2008.

[102] P. Salières, A. L'Huillier, P. Antoine, and M. Lewenstein, "Study of the spatial and temporal coherence of high-order harmonics," *Academic Press*, vol. 41, pp. 83 – 142, 1999.

[103] T. Brabec and F. Krausz, "Intense few-cycle laser fields: Frontiers of nonlinear optics," *Rev. Mod. Phys.*, vol. 72, pp. 545–591, 2000.

[104] P. Antoine, A. L'Huillier, and M. Lewenstein, "Attosecond pulse trains using high–order harmonics," *Phys. Rev. Lett.*, vol. 77, pp. 1234–1237, 1996.

[105] M. Bellini, C. Lyngå, A. Tozzi, M. B. Gaarde, T. W. Hänsch, A. L'Huillier, and C.-G. Wahlström, "Temporal coherence of ultrashort high-order harmonic pulses," *Phys. Rev. Lett.*, vol. 81, pp. 297–300, 1998.

[106] T. Auguste, P. Salières, A. S. Wyatt, A. Monmayrant, I. A. Walmsley, E. Cormier, A. Zaïr, M. Holler, A. Guandalini, F. Schapper, J. Biegert, L. Gallmann, and

U. Keller, "Theoretical and experimental analysis of quantum path interferences in high-order harmonic generation," *Phys. Rev. A*, vol. 80, p. 033817, 2009.

[107] D. J. Hoffmann, C. Hutchison, A. Zaïr, and J. P. Marangos, "Control of temporal mapping and harmonic intensity modulation using two-color orthogonally polarized fields," *Phys. Rev. A*, vol. 89, p. 023423, 2014.

[108] M. B. Gaarde and K. J. Schafer, "Quantum path distributions for high-order harmonics in rare gas atoms," *Phys. Rev. A*, vol. 65, p. 031406, 2002.

[109] W. Becker, A. Lohr, M. Kleber, and M. Lewenstein, "A unified theory of high-harmonic generation: Application to polarization properties of the harmonics," *Phys. Rev. A*, vol. 56, pp. 645–656, 1997.

[110] K. Burnett, V. C. Reed, J. Cooper, and P. L. Knight, "Calculation of the background emitted during high-harmonic generation," *Phys. Rev. A*, vol. 45, p. 3347, 1992.

[111] C. Granados and L. Plaja, "Invalidity of the Ehrenfest theorem in the computation of high-order-harmonic generation within the strong-field approximation," *Phys. Rev. A*, vol. 85, p. 053403, 2012.

[112] C. Chirila and M. Lein, "Assessing different forms of the strong-field approximation for harmonic generation in molecules," *J. Mod. Opt.*, vol. 54, p. 1039, 2006.

[113] E. V. van der Zwan, C. C. Chirilă, and M. Lein, "Molecular orbital tomography using short laser pulses," *Phys. Rev. A*, vol. 78, p. 033410, 2008.

[114] E. Hijano, C. Serrat, G. N. Gibson, and J. Biegert, "Orbital geometry determined by orthogonal high-order harmonic polarization components," *Phys. Rev. A*, vol. 81, p. 041401, 2010.

[115] X. Zhu, M. Qin, Y. Li, Q. Zhang, Z. Xu, and P. Lu, "Tomographic reconstruction of molecular orbitals with twofold mirror antisymmetry: Overcoming the nodal plane problem," *Phys. Rev. A*, vol. 87, p. 045402, 2013.

[116] O. Smirnova, M. Spanner, and M. Ivanov, "Anatomy of strong field ionization ii to dress or not to dress.," *J. Mod. Opt.*, vol. 54, p. 1019, 2007.

[117] A. C. Wahl, "Analytic self consistent field wavefunctions and computed properties for homonuclear diatomic molecules," *The Journal of Chemical Physics*, vol. 41, no. 9, 1964.

[118] W. Becker, F. Grasbon, R. Kopold, D. Milošević, G. Paulus, and H. Walther, "Above-threshold ionization: From classical features to quantum effects," *Academic Press*, vol. 48, pp. 35 – 98, 2002.

[119] R. Kopold, W. Becker, and M. Kleber, "Quantum path analysis of high-order above-threshold ionization," *Optics Communications*, vol. 179, no. 1-6, pp. 39 – 50, 2000.

[120] J. C. Slater, "Atomic shielding constants," *Phys. Rev.*, vol. 36, pp. 57–64, 1930.

[121] S. F. Boys, "Electronic wave functions. i. a general method of calculation for the stationary states of any molecular system," *Proceedings of the Royal Society of London A: Mathematical, Physical and Engineering Sciences*, vol. 200, no. 1063, pp. 542–554, 1950.

[122] P. Atkins and R. Friedman, "Molecular quantum mechanics, fourth edition," *University Oxford Press*, 2005.

[123] M. F. Guest, I. J. Bush, H. J. J. Van Dam, P. Sherwood, J. M. H. Thomas, J. H. Van Lenthe, R. W. A. Havenith and J. Kendrick, "The GAMESS-UK electronic structure package: algorithms, developments and applications," *Mol. Phys.*, vol. 103, p. 719, 2005.

[124] J. S. Binkley, J. A. Pople, and W. J. Hehre, "Self-consistent molecular orbital methods. 21. small split-valence basis sets for first-row elements," *Journal of the American Chemical Society*, vol. 102, no. 3, pp. 939–947, 1980.

[125] M. S. Gordon, J. S. Binkley, J. A. Pople, W. J. Pietro, and W. J. Hehre, "Self-consistent molecular-orbital methods. 22. small split-valence basis sets for second-row elements," *Journal of the American Chemical Society*, vol. 104, no. 10, pp. 2797–2803, 1982.

[126] M. J. Frisch, J. A. Pople, and J. S. Binkley, "SelfâĂŘconsistent molecular orbital methods 25. supplementary functions for gaussian basis sets," *The Journal of Chemical Physics*, vol. 80, no. 7, pp. 3265–3269, 1984.

[127] A. Szabo and N. Ostlund in *Modern Quantum Chemitry:Introduction to Advanced Electronic Structure Theory*, New York: McMillan, 1982.

[128] M. Lein, "Molecular imaging using recolliding electrons," *J. Phys. B*, vol. 40, p. R135, 2007.

[129] B. B. Augstein and C. Figueira de Morisson Faria, "High-order harmonic generation in diatomic molecules: quantum interference, nodal structures and multiple orbitals," *Modern Physics Letters B*, vol. 26, p. 1130002, 2012.

[130] N. H. Shon, A. Suda, Y. Tamaki, and K. Midorikawa, "High-order harmonic and attosecond pulse generations: Bulk media versus hollow waveguides," *Phys. Rev. A*, vol. 63, p. 063806, 2001.

[131] W. H. Press, S. A. Teukolsky, W. T. Vetterling and B. P. Flannery, "Numerical recipes in c++: the art of scientific computing," *Cambridge University Press*, 2002.

[132] M. V. Ammosov, N. B. Delone, and V. P. Krainov, "Tunnel ionization of complex atoms and of atomic ions in an alternating electromagnetic field," *Soviet Physics - JETP*, vol. 64, no. 6, pp. 1191–1194, 1986.

[133] E. Priori, G. Cerullo, M. Nisoli, S. Stagira, S. De Silvestri, P. Villoresi, L. Poletto, P. Ceccherini, C. Altucci, R. Bruzzese, and C. de Lisio, "Nonadiabatic three-dimensional model of high-order harmonic generation in the few-optical-cycle regime," *Phys. Rev. A*, vol. 61, p. 063801, 2000.

[134] B. Henke, E. Gullikson, and J. Davis, "X-ray interactions: Photoabsorption, scattering, transmission, and reflection at e = 50-30,000 eV, Z = 1-92," *Atomic Data and Nuclear Data Tables*, vol. 54, no. 2, pp. 181 – 342, 1993.

[135] P. Balcou, P. Salières, A. L'Huillier, and M. Lewenstein, "Generalized phase-matching conditions for high harmonics: The role of field-gradient forces," *Phys. Rev. A*, vol. 55, pp. 3204–3210, 1997.

[136] L. Chipperfield, J. Robinson, P. Knight, J. Marangos, and J. Tisch, "The generation and utilisation of half-cycle cut-offs in high harmonic spectra," *Laser & Photonics Reviews*, vol. 4, no. 6, pp. 697–719, 2010.

[137] M. Lein, N. Hay, R. Velotta, J. P. Marangos and P. L. Knight, "Role of the intramolecular phase in high-harmonic generation," *Phys. Rev. Lett.*, vol. 88, p. 183903, 2002.

[138] N. B. Delone and V. P. Krainov, "Energy and angular electron spectra for the tunnel ionization of atoms by strong low-frequency radiationd," *J. Opt. Soc. Am. B*, vol. 8, p. 1207, 1991.

[139] P. Dietrich, N. H. Burnett, M. Ivanov, and P. B. Corkum, "High-harmonic generation and correlated two-electron multiphoton ionization with elliptically polarized light," *Phys. Rev. A*, vol. 50, p. R3585, 1994.

[140] W. Becker, S. Long and J. K. McIver, "Modeling harmonic generation by a zero-range potential," *Phys. Rev. A*, vol. 50, p. 1540, 1994.

[141] B. Wang, X. Li, and P. Fu, "Polarization effects in high-harmonic generation in the presence of static-electric field," *Phys. Rev. A*, vol. 59, p. 2894, 1999.

[142] D. Milošević, "Cutoff law for high-harmonic generation by a ellitpically polarized field," *J. Phys. B*, vol. 33, p. 2479, 2000.

[143] A. de Bohan, P. Antoine, D. B. Milošević, and B. Piraux, "Phase-dependent harmonic emission with ultrashort laser pulses," *Phys. Rev. Lett.*, vol. 81, pp. 1837–1840, 1998.

[144] C. A. Haworth, L. E. Chipperfield, J. S. Robinson, P. L. Knight, J. P. Marangos and J. W. G. Tisch, "Half-cycle cutoffs in harmonic spectra and robust carrier-envelope phase retrieval," *Nature*, vol. 3, p. 52, 2007.

[145] K. Kato, S. Minemoto, and H. Sakai, "Suppression of high-order-harmonic intensities observed in aligned CO_2 molecules with 1300-nm and 800-nm pulses," *Phys. Rev. A*, vol. 84, p. 021403, 2011.

[146] A. Rupenyan, P. M. Kraus, J. Schneider, and H. J. Wörner, "High-harmonic spectroscopy of isoelectronic molecules: Wavelength scaling of electronic-structure and multielectron effects," *Phys. Rev. A*, vol. 87, p. 033409, 2013.

[147] D. Pavičić, K. Lee, D. Rayner, P. Corkum, and D. Villeneuve, "Direct measurement of angular dependence of ionization for N_2, O_2 and CO_2 in intense laser fileds," *Phys. Rev. Lett.*, vol. 98, p. 243001, 2007.

[148] M. Abu-samha and L. B. Madsen, "Theory of strong-field ionization of aligned co_2," *Phys. Rev. A*, vol. 80, p. 023401, 2009.

[149] S. Petretti, Y. V. Vanne, A. Saenz, A. Castro, and P. Decleva, "Alignment-dependent ionization of n_2, o_2, and co_2 in intense laser fields," *Phys. Rev. Lett.*, vol. 104, p. 223001, 2010.

[150] V. R. Bhardwaj, D. M. Rayner, D. M. Villeneuve, and P. B. Corkum, "Quantum interference in double ionization and fragmentation of C_6H_6 in intense laser fields," *Phys. Rev. Lett.*, vol. 87, p. 253003, 2001.

[151] V. H. Le, A. T. Le, R. H. Xie, and C. D. Lin, "Theoretical analysis of dynamic chemical imaging with lasers using high-order harmonic generation," *Phys. Rev. A*, vol. 76, p. 013414, 2007.

[152] A. T. Le, R. Lucchese, S. Tonzani, T. Morishita, and C. Lin, "Quantitative rescattering theory for high-order harmonic generation from molecules," *Phs. Rev. A*, vol. 80, p. 013401, 2009.

[153] C. Greenei, "Discussion on molecular tomography," *Presentation: see http://online.kitp.ucsb.edu/online/atto06/moletomo/.*

[154] C. Zhai, L. He, P. Lan, X. Zhu, Y. Li, F. Wang, W. Shi, Q. Zhang, and P. Lu, "Coulomb-corrected molecular orbital tomography of nitrogen," *Scientific Reports*, vol. 6, p. 23236, 2016.

[155] L. V. Keldysh, "Ionization in the field of a strong electromagnetic wave," *Sov. Phys. JETP*, vol. 20, p. 1307, 1964.

[156] F. H. M. Faisal, "Collision of electrons with laser photons in a background potential," *J. Phys. B*, vol. 6, p. L89, 1973.

[157] H. R. Reiss, "Effect of an intense electromagnetic field on a weakly bound system," *Phys. Rev. A*, vol. 22, pp. 1786–1813, 1980.

[158] D. G. Arbó, K. L. Ishikawa, K. Schiessl, E. Persson, and J. Burgdörfer, "Intracycle and intercycle interferences in above-threshold ionization: The time grating," *Phys. Rev. A*, vol. 81, p. 021403, 2010.

[159] X. Lai, W. Quan, "Private communication,"

[160] T. Shaaran and C. Figueira de Morisson Faria and H. Schomerus, "Causality and quantum interference in time-delayed laser-induced nonsequential double ionization," *Phys. Rev. A*, vol. 85, p. 023423, 2012.